SEARCH FOR A RIGHT-HANDED W BOSON AND HEAVY NEUTRINO IN PROTON-PROTON COLLISIONS AT 13 TEV WITH THE CMS DETECTOR

A Dissertation

Presented to the Faculty of the Graduate School

of Cornell University

in Partial Fulfillment of the Requirements for the Degree of

Doctor of Philosophy

by

Jorge Enrique Chaves

August 2017

SEARCH FOR A RIGHT-HANDED W BOSON AND HEAVY NEUTRINO IN PROTON-PROTON COLLISIONS AT 13 TEV WITH THE CMS DETECTOR

Jorge Enrique Chaves, Ph.D.

Cornell University 2017

A search for a right-handed heavy gauge boson W in the context of the Left-Right symmetry model is presented. The search has been conducted using the Compact Muon Solenoid detector at the Large Hadron Collider with proton-proton collision data corresponding to an integrated luminosity of 35.9 fb^{-1} at a center-of-mass energy of 13 TeV. The events selected are required to have two same flavor charged leptons (e or μ) and two jets. No excess above standard model expectation is seen in the invariant mass distribution of the two lepton, two jet system. Assuming identical couplings and decay branching fractions as the left-handed gauge boson, a W_R boson with a mass less than 4.4 TeV is excluded at 95% confidence level.

BIOGRAPHICAL SKETCH

Jorge Chaves began his undergraduate studies at the Universidad Nacional de Colombia, but transferred to Rutgers University where he received his B.S in physics in 2011. At Rutgers, Jorge worked with Professor Eva Halkiadakis as an undergraduate researcher on the Compact Muon Solenoid experiment. In the summer of 2010, Jorge participated in a Research Experience for Undergraduates at the University of Chicago with Professor Florencia Canelli, working on energy calibration of jets with data from the CDF experiment at Fermilab.

Jorge has been working with Professor Peter Wittich at Cornell University since the summer of 2011 on several projects related to the Compact Muon Solenoid experiment. Some of this work is described in this dissertation. Jorge was a National Science Foundation Graduate Research Fellow from 2012 until 2016.

Jorge will continue as a postdoctoral researcher at the University of Pennsylvania working on neutrino physics.

To Andrea, for always being there with love and support.

ACKNOWLEDGEMENTS

First, I would like to thank my advisor, Peter Wittich, for his support and guidance over the years. I am grateful for the many conversations we had about physics and many other subjects. I had a great experience during my graduate studies and this is certainly due to the interesting projects I was able to work on thanks to Peter. His enthusiasm for neutrino physics was one of the main reasons why I have decided to pursue this kind of science as a postdoctoral researcher.

I also want to thank postdoc Jordan Tucker for his help throughout the years. We worked together on several projects and he was always willing to provide his valuable input. In particular, we studied the behavior of cosmic muons and the alignment of the CMS detector, from which I learned a great deal.

The results of the tracklet project were possible because of all the work from a small group of institutions, including Cornell University, Rutgers University, Ohio State University, and Notre Dame University. I would like to thank in particular Professor Anders Ryd for all his help in making the tracklet implementation possible and also to Cornell engineer Charlie Strohman for his help getting started on Verilog and firmware development. Professors Peter Wittich, Eva Halkiadakis, Yuri Gerstein, and Brian Winer provided valuable suggestions and input from their combined experience. Postdoc Louise Skinnari was responsible for a large fraction of the simulation of the project. Last but not least, thanks to my fellow graduate students Zhengcheng Tao, Margaret Zientek, Savvas Kyriacou, and Anthony Lefeld.

The search for right-handed W was initially performed by physicists at the University of Minnesota. We joined their effort for the current iterations of the search, the most recent of which is described in this dissertation. I would like to

thank Professors Jeremy Mans and Roger Rusack, postdoc Nicole Ruckstuhl and graduate students Sean Kalafut and Andrew Evans. Graduate student Giulia Negro has also joined the effort helping with signal production and limit setting.

I would like to thank the Cornell CMS group and the physics department for providing the right environment for research and study. The flexibility in the program allowed me to take courses that I found interesting, even those not directly related to my research.

Finally, I would like to thank my wife Andrea for her love and support. Together with Lupe we made a home in Ithaca and I am looking forward to what awaits us in the future.

TABLE OF CONTENTS

LIST OF TABLES

LIST OF FIGURES

CHAPTER 1

INTRODUCTION

In the field of particle physics, we aim at finding the most fundamental building blocks of matter. Over many decades, we have been able to probe deeper and deeper into the structure of matter by colliding particles at higher and higher energies. This approach has been extremely fruitful to this day, when we currently collide particles at a center of mass energy of 13 TeV in the Large Hadron Collider (LHC). The LHC has now been running since 2010 and will continue for many more years, providing the experiments with huge amounts of data to probe the fundamental structure of matter.

In our understanding of elementary particles, we initially believed that atoms were the indivisible unit of matter. In fact, atoms are divisible and are made of nucleons, which in turn are made from quarks. A theory to explain this structure was conceived in the 1970s, known as the standard model of particle physics [1–3], and so far has been extremely successful at explaining the experimental data collected over the years. The standard model defines a set of fundamental particles and the forces that govern their interactions. The theory made many prediction for yet unseen particles that were later discovered at collider experiments. One of the fundamental predictions of the standard model was the existence of a new scalar field and an associated particle known as the Higgs boson.

In July 2012, the discovery of the Higgs boson was announced by the CMS and ATLAS experiments at the Large Hadron Collider [4, 5]. By smashing two beams of protons at record energies, this predicted particle was seen at a mass approximately 125 times that of the proton. The two experiments were able to

see the decay products of the Higgs boson and reconstruct the initial particle and study its properties. This discovery has been the crowning achievement of the Large Hadron Collider as it completes the last major prediction of the standard model.

Although the theory has been so successful, there are remaining questions in particle physics that lie beyond the scope of the standard model. For instance in the last 20 years, we have confirmed that neutrinos have a very small mass, albeit not zero as in the standard model. The weak force that explains radioactive decays is inherently asymmetric, as it only couples particles of a specific chirality. This is evident in the lepton sector, where only left-handed neutrinos are present in the standard model. These are some of questions still unresolved in the standard model and we discuss more on this in Chapter 2.

Some other theory beyond the standard model should come into play at a higher energy scale that can solve the puzzles still left in particle physics. One proposed theory introduces an additional symmetry in the standard model that mirrors that of the weak force, known as the Left-Right symmetry model [6–10]. This theory predicts the existence of additional heavy particles similar to the W and Z bosons, as well as a new kind of neutrinos.

A search for these new heavy particles was done in CMS using the data collected in 2011 and 2012 [11]. The authors of this search reported an excess of events in the data compared to the prediction from only standard model processes. In particle physics, evidence for a new particle can be claimed when the number of events seen deviates by more than three standard deviations from the null-hypothesis prediction. In this case, the authors reported an excess with a 2.8σ local significance, just shy of being able to claim this as evidence for a

new particle.

The events in excess were very carefully studied by the authors of the search, as well as by other groups as a cross check of the methodology. After intense scrutiny, it was determined that the excess was real and not an artifact of experimental error. This in turn lead to the need for more data to be collected as the main limitation became the statistics. This, however, would have to wait until the second run of the LHC.

In this dissertation, we present the continuation of the search for a right-handed W using the data collected by CMS in 2016. We also discuss in detail a prototype system to perform fast tracking for the CMS upgrade.

This dissertation is organized as follows. An overview of the standard model and the Left-Right symmetry model is presented in Chapter 2. In Chapter 3, we describe the LHC and the CMS detector. Chapter 4 contains a brief description of object reconstruction relevant to the search for right-handed W bosons. The details of the search are presented in Chapter 5. We conclude in Chapter 6.

Appendix A describes our work for the proposed track-trigger system of CMS using Field Programmable Gate Arrays. Appendix B presents a measurement of the momentum resolution of muons using cosmic rays in the CMS detector, relevant to the analysis presented.

CHAPTER 2

STANDARD MODEL AND THE LEFT-RIGHT SYMMETRY

In this Chapter, we present an overview of the standard model (SM) and the questions still left unanswered by it. We discuss some of the proposed models for theories beyond the standard model with a focus on the Left-Right symmetry model. A search for a right-handed W boson in the context of this model is described in this dissertation.

2.1 Standard model

The standard model [1, 12, 13] describes elementary particles and the fundamental forces that govern their interactions (excluding gravity). To construct the Lagrangian of the SM, we need only to input the gauge symmetries associated to the forces in nature, strong and electroweak, and the irreducible representation of particles in these gauge groups. The symmetry group of the SM is

$$SU(3)_C \times SU(2)_L \times U(1)_Y, \tag{2.1}$$

where $SU(3)_C$ represents the strong nuclear force and $SU(2)_L \times U(1)_Y$ corresponds to the unified electromagnetic and weak forces. The generators of these symmetry groups correspond to the eight gluons fields G_a^μ for SU(3), three boson fields W_a^μ for SU(2), and one boson field B^μ for U(1).

The other input needed to construct the SM are the irreducible representations of the three generations of quarks and leptons and the scalar field ϕ identified as the Higgs field. Due to the chiral structure of the electroweak force, we

Field	Representation
Q_{Li}	$(3,2)_{+1/6}$
U_{Ri}	$(3,1)_{+2/3}$
D_{Ri}	$(3,1)_{-1/3}$
L_{Li}	$(1,2)_{-1/2}$
E_{Ri}	$(1,1)_{-1}$
ϕ	$(1,2)_{+1/2}$
G_a^μ	$(8,1)_0$
W_a^μ	$(1,3)_0$
B^μ	$(1,1)_0$

Table 2.1: Representation of SM fields, i=1,2,3. Convention $(A,B)_Y$, where A is for SU(3), B is for SU(2) and Y is hypercharge

have left-handed quark and lepton isospin doublets, quark and charged lepton right-handed singlets, but no right-handed neutral singlets. This means that there are no right-handed neutrinos in the SM. Table 2.1 shows these representations for the SM fields.

It is worth noting that we have introduced the weak interaction as chiral in our gauge description. The experimental data suggests that the interaction is of the form $V-A$ [14]. However, there is no underlying theoretical motivation why this should be the case, or why there is not also a $V+A$ interaction. The case for adding the $V+A$ interaction is mainly aesthetic, but as we will notice in our description of the Left-Right symmetry model it also provides a natural explanation for neutrino masses.

If the SM was a fully symmetric theory, all the gauge bosons would be massless. This is certainly the case for photons and gluons, but we know that this is not true for the W and Z bosons. Thus, the electroweak symmetry must be broken. The Higgs mechanism describes the pattern of *spontaneous symmetry*

breaking in the electroweak sector,

$$SU(3)_C \times SU(2)_L \times U(1)_Y \rightarrow SU(3)_C \times U(1)_{EM}, \tag{2.2}$$

which gives rise to the masses of the W and Z, as well as the fermions' masses through additional Yukawa interaction terms in the Lagrangian.

Another output of the theory are the accidental symmetries. These symmetries often come from the renormalizable terms in the Lagrangian and are broken by higher order non-renormalizable terms. Some examples of accidental symmetries include the lepton and baryon number in any SM process. Experiments are looking for decays that could violate lepton number conservation, such as $\mu \rightarrow e^+e^-e^+$ [15], as well as experiments looking for Majorana masses [16] for neutrinos that could lead to some new physics.

With the symmetries and irreducible representations as our inputs, we can construct the most general Lagrangian up to dimension 4.

$$\mathcal{L} = \mathcal{L}_{kinetic} + \mathcal{L}_{Yukawa} + \mathcal{L}_{Higgs}. \tag{2.3}$$

This Lagrangian represents a generic standard model. In order to make it "the" standard model, we have to measure the parameters of the theory that we see in nature. The SM has 18 free parameters that, once measured, completely determine the model and allow us to make predictions. These parameters correspond to the 6 quark masses, the 3 charged lepton masses, 2 parameters of the Higgs potential (usually the vacuum expectation value and the Higgs boson mass), 3 gauge couplings, 3 mixing angles and the CP-violating phase of the Cabibbo-Kobayashi-Maskawa (CKM) matrix.

The CKM matrix is a unitary matrix that determines the strength of quark mixing in weak decays. The mass eigenstates of the quarks are not the same as the weak eigenstates, thus leading to the only flavor changing interactions in the SM. Initially conceived as a 2×2 matrix to explain mixing with the strange, and later with the charm quarks, with a single Cabibbo angle θ_C. It was further generalized to 3×3 to include the third generation when evidence for CP violation made necessary an additional phase. A similar matrix to describe the neutrino mixing between flavor and mass eigenstates was proposed by Pontecorvo, Maki, Nakagawa, and Sakata (PMNS matrix).

It is not necessary to measure the parameters directly, as it is sometimes experimentally challenging, but rather we need 18 independent measurements that can specify our model. With the discovery of the Higgs boson [4, 5], the final free parameter of the SM corresponding to the Higgs mass has been measured. Its couplings to the fermion fields are fixed by the masses and we can measure these couplings as a further test of the SM. Table 2.2 shows the current best measurements of the parameters of the SM.

2.2 Beyond the Standard Model

Although the SM has been extremely successful at explaining experimental results, there is undeniable evidence that it is not the complete description of the universe. Instead, the SM is a low-energy effective theory valid up some energy scale Λ deriving from a Grand Unified Theory (GUT) from a single gauge group.

Perhaps the most notable shortcoming of SM is that it does not include grav-

Parameter	Value
Electron mass m_e	511 keV
Muon mass m_μ	105.7 MeV
Tau mass m_τ	1776.86 ± 0.12 MeV
Up quark mass m_u	2.2 ± 0.6 MeV
Down quark mass m_d	4.7 ± 0.5 MeV
Strange quark mass m_s	96 ± 8 MeV
Charm quark mass m_c	1.27 ± 0.03 GeV
Bottom quark mass m_b	4.18 ± 0.04 GeV
Top quark mass m_t	173.21 ± 1.22 GeV
CKM matrix λ	0.22506 ± 0.00050
CKM matrix A	0.811 ± 0.026
CKM matrix $\bar{\rho}$	0.124 ± 0.019
CKM matrix $\bar{\eta}$	0.356 ± 0.011
U(1) gauge coupling α	137.035999074
SU(2) gauge coupling G_F	1.1663787×10^{-5} GeV^{-2}
SU(3) gauge coupling $\alpha_s(s = M_Z^2)$	0.120
Higgs vacuum expectation value v	246 GeV
Higgs mass m_H	125.09 ± 0.32 GeV

Table 2.2: SM parameters from PDG [17]. CKM matrix is expressed in terms of the Wolfenstein parametrization.

ity. In fact, the effect of gravity at small scales is extremely weak. The strength of the gravitational attraction at the quantum level is expected to be comparable to the other forces at the Planck scale ($M_{Planck} \approx 10^{19}$ GeV[1]). This scale is well beyond what we can probe in our current experiments and therefore, theories that incorporate gravity are not easily tested.

Our description of the standard model assumed that neutrinos are massless. Experiments such as SNO [18] and Super-Kamiokande [19] proved that neutrinos have mass. The experiments measured an oscillation between electron neutrinos and muon neutrinos coming from the sun and the earth's atmosphere. This oscillation is only possible if there is a difference in mass between

[1]Masses are expressed in units of eV/c^2, but it is convention to take $\hbar = c = 1$.

the neutrino mass eigenstates. From cosmological observations [20], an upper limit was also placed on the absolute mass scale of neutrinos. These masses are uncomfortably small compared with any other mass scale in the SM.

As mentioned before, the mass of the Higgs boson is a free parameter of the SM, but the fact that it is 125 GeV has some implications for model-building. Even before the Higgs was discovered, the troubling realization that its mass would be subject to very large loop corrections had led theorists to suggest ways to solve this without relying on a fine tuned cancellation between the bare mass and the quantum corrections. One particular model was supersymmetry (SUSY) [21], where a new fermion-boson symmetry is introduced. The biggest contribution to the Higgs loop corrections comes from the top quark because of its large coupling to the Higgs. The superpartner to the top, a boson, will contribute to these corrections with an opposite sign, effectively cancelling the large Higgs mass corrections. SUSY is not an exact symmetry, as the superpartners are expected to be much heavier than SM particles, but also light enough to still provide a natural solution to the fine-tuning problem. Supersymmetric particles have not yet been observed at the LHC, placing more stringent constraints on the possible masses of the superpartners and making SUSY less appealing theoretically.

The matter that is described by the SM only makes up roughly 5% of the total energy content of the entire universe [22]. Of the remaining 95%, approximately 20% consists of dark matter and the rest is dark energy. Dark matter is not only dark to electromagnetic interactions, but it also does not interact strongly with any of the forces described by the SM. Its presence is inferred from its gravitational interaction with baryonic matter. From a particle physics perspective, this

new type of matter should come from a new particle. Many models, including SUSY, propose a weakly interactive massive particle (WIMP) as a candidate for dark matter. This is a very active area of research at collider experiments as well as direct detection experiments [23] and even satellite based detectors [24].

As mentioned above, the weak force is chiral and only left-handed particles couple with right-handed antiparticles. From the table of fields in the SM, an obvious missing element are the right-handed neutrinos. Completing this table and restoring the chiral symmetry to the standard model are the motivations for Left-Right (LR) symmetry models [6–10].

2.2.1 Left-Right symmetry model

By introducing an additional $SU(2)_R$ symmetry to the SM, we regain this missing element in Table 2.1 at the cost of introducing new gauge heavy bosons and additional Higgs multiplets. The gauge symmetries would then include

$$SU(2)_L \times SU(2)_R \times U(1)_{L-B}, \tag{2.4}$$

(omitting the color) and the irreducible representations mirror the left-handed sector. There is an accidental symmetry of $B - L$ rather than individual baryon and lepton number conservation as in the SM.

Quarks and leptons are now completely left-right symmetric,

$$Q_{L,R} = \begin{pmatrix} u \\ d \end{pmatrix}_{L,R}, L_{L,R} = \begin{pmatrix} l \\ \nu \end{pmatrix}_{L,R} \tag{2.5}$$

and the electromagnetic charge is now defined as

$$Q_{EM} = I_{3L} + I_{3R} + \frac{B - L}{2}. \tag{2.6}$$

The Higgs sector is more complicated, as the SM representation is replaced by a bi-doublet $\phi = (2_L, 2_R, 0_{B-L})$ and there are now two additional triplets $\Delta_L = (3_L, 1_R, 2)$ and $\Delta_R = (1_L, 3_R, 2)$. The ground states of these fields are chosen to be

$$\langle\phi\rangle = \begin{pmatrix} v_1 & 0 \\ 0 & v_2 e^{i\alpha} \end{pmatrix}, \langle\Delta_L\rangle = 0, \langle\Delta_R\rangle = \begin{pmatrix} 0 & 0 \\ v_R & 0 \end{pmatrix}, \tag{2.7}$$

where $v_{1,2}$ are real positive numbers and $v_R \gg v_{1,2}$. This choice ensures that the new right-handed bosons are much heavier than the SM bosons and the LR symmetry is broken down to the SM $SU(2)_L \times U(1)$. The electroweak spontaneous symmetry breaking proceeds as before and we recover the SM at low energies.

The masses of the right-handed bosons are given by

$$M_{W_R}^2 = g^2 v_R^2 \tag{2.8}$$

$$M_{Z_R}^2 = (g^2 + g_{B-L}^2) v_R^2 \tag{2.9}$$

where $g = g_L = g_R$. Additional mixing angles analogous to the Weinberg angle can be constructed from these gauge couplings. These angles determine the amount of mixing between the left-handed W and the much heavier right-handed W. Precision measurements place tight constraints on the mixing between left and right handed bosons. We can identify the light mass eigenstates as the SM bosons and the heavy mass eigenstates as our predicted new right-handed partners.

The Yukawa interaction of the quarks with the Higgs bi-doublet after spontaneous symmetry breaking (SSB) generates mass matrices

$$M_u = Y v_1 + \tilde{Y} v_2 e^{-i\alpha} \tag{2.10}$$

$$M_d = Y v_2 e^{-i\alpha} + \tilde{Y} v_1. \tag{2.11}$$

These matrices can be diagonalized such that

$$M_u = U_{uL} m_u U_{uR}^{\dagger}, \quad M_d = U_{dL} m_u U_{dR}^{\dagger}. \tag{2.12}$$

We have then recovered the CKM matrix $V_{CKM} = U_{uL}^{\dagger} U_{dL}$ and constructed the right-handed analogue $V_R = U_{uR}^{\dagger} U_{dR}$. This matrix effectively controls the branching ratios of the right-handed W into SM quarks and leptons. Since the theory does not put any constraints on the values of the matrix, it is convenient to assume that they are equal to those of the CKM matrix. We use this assumption for the experimental search described in this dissertation.

Another consequence of the LR symmetry is that by introducing the right-handed neutrinos, there are then new terms in the Lagrangian

$$\mathcal{L}_N = \frac{1}{2} M_{ij}^N N_{R_i} N_{R_j} + Y_{ij}^N \bar{L_{L_i}} \tilde{\phi} N_{R_j} + h.c, \tag{2.13}$$

which correspond to a Majorana mass term and a Yukawa coupling term. The right-handed neutrino then generates a mass term for the SM neutrinos. The see-saw mechanism [25, 26] explains how three generations of heavy N_R mix with the SM light neutrinos, and how they acquire masses that are inversely proportional to the mass of the N_R.

2.3 Summary

We have presented a Left-Right symmetry extension of the standard model, where heavy right-handed bosons decay can decay to SM particles. In the search presented in this dissertation, we have made as few assumptions about the details of the model in a way that the final result can be reinterpreted as a search

for a heavy resonance search. These possible reinterpretations have been discussed in the literature [27–31].

CHAPTER 3

EXPERIMENTAL APPARATUS

In this Chapter, we describe the Large Hadron Collider (LHC) and the Compact Muon Solenoid detector (CMS) used to record the collision events studied in this dissertation.

3.1 The Large Hadron Collider

The LHC [32] is the most powerful particle accelerator and hadron collider built to date. Located under the Franco-Swiss border, near the city of Geneva, the LHC was built inside CERN's 27 km LEP ring with a design center-of-mass energy of 14 TeV and a design instantaneous luminosity of $\mathcal{L} = 10^{34}\text{cm}^{-2}\text{s}^{-1}$.

The process of particle acceleration begins from a simple tank of hydrogen as the source of protons, which are progressively accelerated to higher energies in sequential machines ending at the LHC. A diagram of the CERN accelerator complex is shown in Figure 3.1. The hydrogen atoms are stripped of their electrons and are accelerated by a linear accelerator, Linac2, using alternatingly charged cylindrical conductors. The conductors generate electric fields that accelerate the beam, while superconducting quadrupole magnets generate magnetic fields that keep the beam focused. The protons are accelerated by Linac2 to 50 MeV before moving to the next stage, the Proton Synchrotron Booster (PSB). Linac2 is expected to be replaced in 2020 by Linac4, which will deliver protons at 160 MeV and will increase the beam brightness by a factor of 2 in preparation for a higher luminosity phase of running.

Protons are accelerated to 1.4 GeV by the PSB before going to the Proton

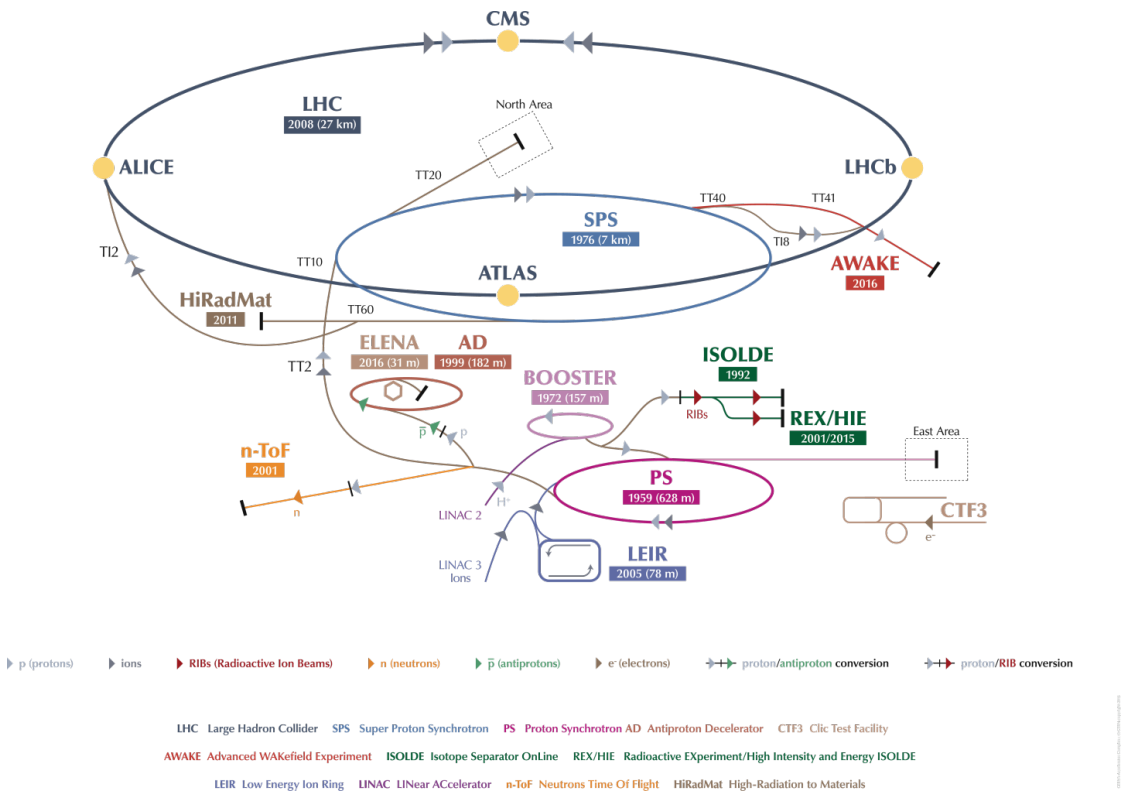

Figure 3.1: Illustration of the CERN accelerator complex including the four main experiments and the injection chain [33].

Synchrotron (PS). In heavy ion running, the PS is instead supplied by the Low Energy Ion Ring (LEIR). Originally built in 1959, the PS was at the time the most powerful synchrotron but now it serves mainly as a pre-stage for the more powerful machines. Protons leave the PS in bunch trains at an energy of 25 GeV before moving to the Super Proton Synchrotron (SPS). In the final stage before particles are injected into the LHC, the SPS accelerates protons to 450 GeV. The W and Z gauge bosons were discovered at the SPS in 1983 in proton-antiproton collisions.

Finally, 2808 bunches per beam with 1.15×10^{15} protons reach the LHC for the final acceleration. These bunches are accelerated around the LHC ring for

approximately 20 minutes before reaching the maximum energy, gaining 0.5 MeV per turn, at a beam-crossing frequency of 40 MHz. These bunches are spaced out throughout the ring in trains of 72 bunches, followed by a beam dump gap of 8 empty bunches. LHC fills last several hours while the beams circulate around the ring and collide at the interaction points.

The circular orbit of the protons along the ring is guided by strong superconducting electromagnets. RF cavities in the straight sectors of the LHC accelerate the beams to their final energy. There are approximately 9600 magnets in the LHC, including the 1232 main dipole magnets, plus quadrupoles, sextupoles, octupoles, and decapoles. The main bending of the beam is done by the dipoles, while the higher order magnets correct the particles' trajectories. A cross-sectional view of a LHC dipole magnet is shown in Figure 3.2.

The dipoles are made from niobium-titanium (NbTi) cables that are cooled using superfluid helium below their superconducting critical temperature of 10 K. This allows for a higher current to flow and generate the strong field needed to bend the beams to their 7 TeV design energy. At a temperature of 1.9 K, a current of 11,850 A flows through the dipole to create an 8.33 T magnetic field. The cold mass and cryostat encasing the dipoles also includes the higher order correcting magnets as well as the two beam pipes for the counter-rotating beams. These two beams are brought together to collide at the four detector sites along the ring.

The number of collisions generated at the LHC is directly proportional to the cross section for proton-proton interactions and the instantaneous luminosity, integrated over time,

$$N_{events} = \int \mathcal{L}\sigma dt. \tag{3.1}$$

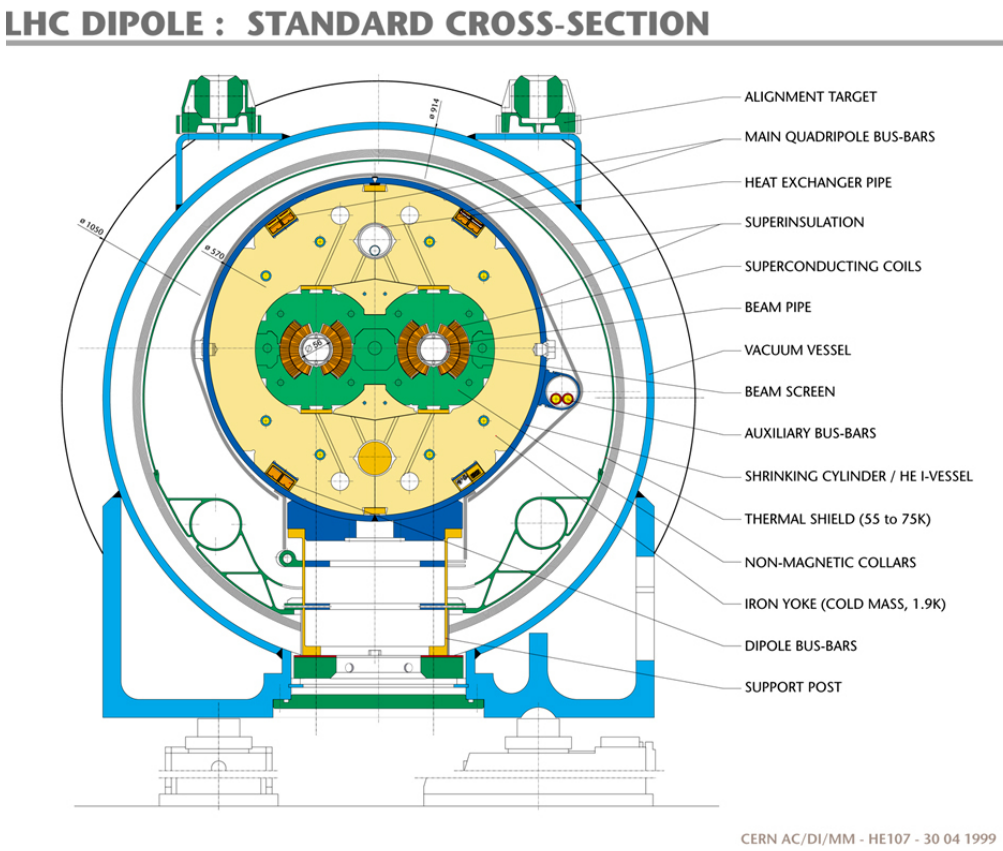

Figure 3.2: Illustration of an LHC dipole magnet with the two beam pipes for protons or heavy ions [34].

The instantaneous luminosity is defined as a function of the beam parameters and can be written as

$$\mathcal{L} = \frac{N_1 N_2 n_b f_{rev}}{AF}, \tag{3.2}$$

where N_1 and N_2 are the number of protons per bunch, n_b is the number of bunches per beam, f_{rev} the beam revolution frequency (11.2455 kHz), A is the cross sectional area of the beams at the interaction point, and F is a reduction factor to account for the non-zero crossing angle at the interaction point [35].

The number of events can only be increased by increasing the instantaneous luminosity. The frequency of the beams is effectively fixed since the particles are traveling so close to the speed of light and by the design of the accelerator RF cavities. Therefore, the luminosity can be increased by either increasing the number of protons per bunch, including more tightly spaced bunches, or by decreasing the area of interaction A. The cross sectional area can be expressed as

$$A = \frac{4\pi\epsilon_n\beta^*}{\gamma_r}, \tag{3.3}$$

where ϵ_n is the normalized transverse beam emittance[1], β^* is the beta function at the interaction point[2], and γ_r is the relativistic gamma factor.

The LHC's design instantaneous luminosity was 10^{34} cm^{-2}s^{-1}, which was surpassed during the 2016 run of the LHC. For the high-luminosity upgrade, the planned instantaneous luminosity is 7.5×10^{34} cm^{-2}s^{-1}. The integrated luminosity corresponds to the time integral of the instantaneous luminosity over the running period and it is measured in inverse barns (1 barn = 10^{-24} cm^2).

The LHC can be configured to collide two beams of protons, lead ions on protons, or lead ions on other ions. During the proton-proton configuration, the two beams are currently accelerated to energies up to 6.5 TeV (center of mass energy $\sqrt{s}$=13 TeV) and collided at four intersection points along the ring. These collisions are recorded by the four main experiments: ALICE [36], ATLAS [37], CMS [38], and LHCb [39]. While ATLAS and CMS are considered

[1]Emittance describes the spread of the beam in position and momentum phase space.
[2]The beta function describes the transverse size of the beam along the beam trajectory at the interaction point.

general purpose detectors, ALICE and LHCb are more specialized and receive less integrated luminosity. LHCb records and studies events with b quarks with a specialized forward detector layout to take advantage of the fact that $b - \bar{b}$ events are mostly produced in the same forward direction. Recent results from LHCb have provided evidence for the rare decay of $B_S \rightarrow \mu\mu$[40], a flavor changing neutral current interaction, as well as pentaquarks[41]. ALICE studies collisions of heavy ions that can produce a quark-gluon plasma.

The total integrated luminosity collected in 2016 by the CMS detector is shown in Figure 3.3. This dataset corresponding to 35.9 fb^{-1} of good data is used for the search described in this dissertation.

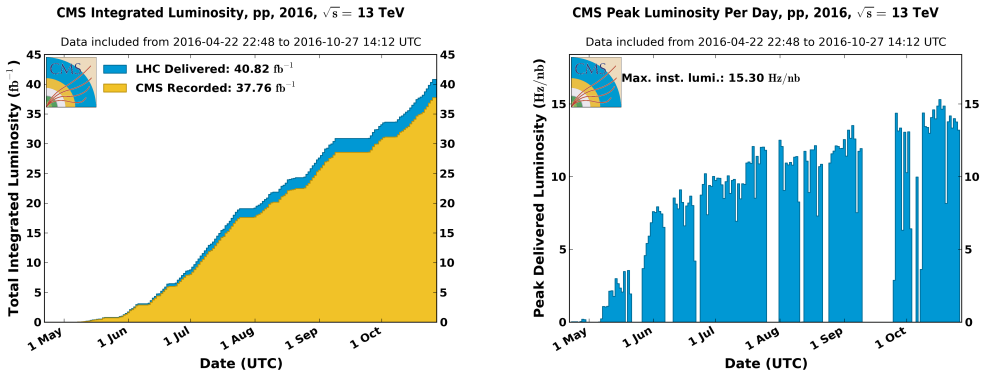

Figure 3.3: Operating conditions of the CMS detector in 2016 [42]. (Left) Total integrated luminosity in 2016. (Right) Peak luminosity per day in 2016.

3.2 Compact Muon Solenoid detector

One of the two general purpose detectors at the LHC, CMS measures 15 meters tall, 22 meters long, and weighs 14000 tons. It sits 100 meters below the surface at the LHC interaction point opposite the CERN site. At half the size of

ATLAS and twice the weight, CMS is dense and compact. The distinguishing characteristic of CMS is its strong axial magnetic field of 3.8 T, generated by a superconducting solenoid magnet that surrounds the inner detector subsystems. A diagram of the CMS detector is shown in Figure 3.4. CMS is built from multiple subsystems arranged in concentric layers around the beam pipe. The pixel detector is the closest to the interaction point, farther out is the silicon tracker, surrounded by the electromagnetic and hadronic calorimeters, and finally the muon system outside the solenoid magnet.

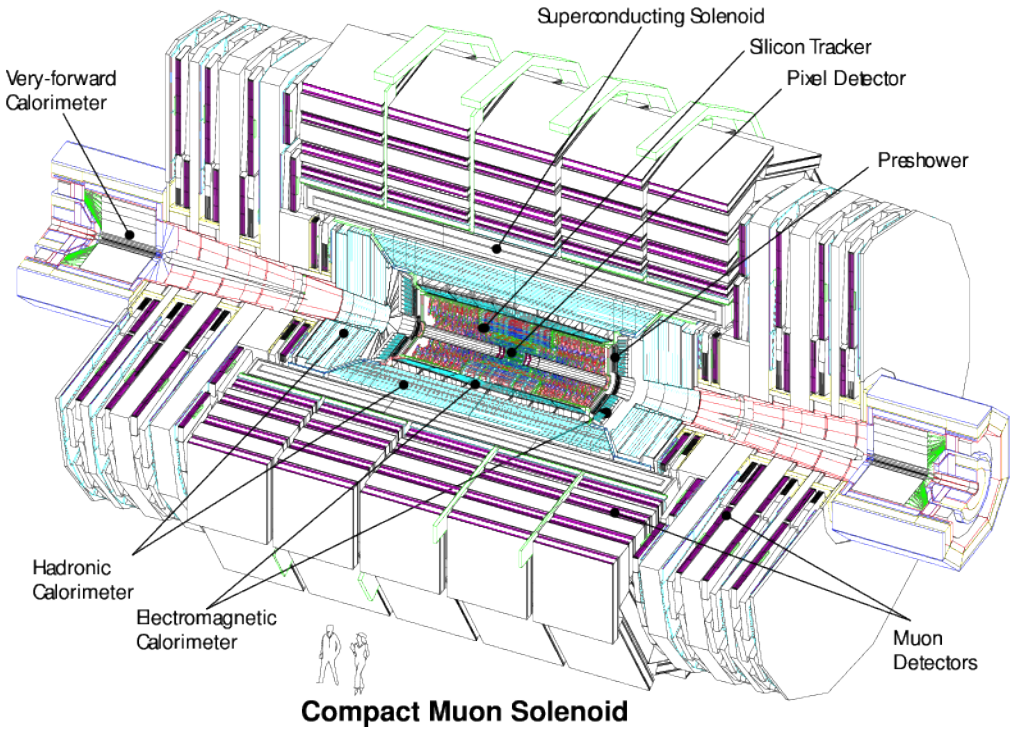

Figure 3.4: Cross sectional view of the CMS detector [38]. CMS consists of multiple subsystems arranged in concentric layers around the beam pipe. Silicon trackers are the innermost subdetectors, followed by the calorimeters, and then the muon system as the outermost subdetector.

3.2.1 Coordinate System

The coordinate system of CMS is defined by the plane of the LHC ring. The x-axis points toward the center of the ring, the y-axis points upward perpendicular to the plane, and the positive z-axis is determined by a right-handed coordinate system along the beam. The nominal interaction point of the beams defines the origin of the coordinate system.

A more convenient system used in colliders defines the azimuthal angle ϕ in the $x - y$ plane, also referred to as the transverse plane, measured with respect to the x-axis. A radial coordinate r is also defined in the transverse plane. The magnetic field of CMS bends the trajectories of charged particles in the transverse plane, which makes the description of these trajectories more convenient in $r - \phi$ coordinates. Finally, we define the pseudorapidity as $\eta = -\ln\tan(\theta/2)$, where θ is the polar angle measured from the positive z-axis. In the case of particles where the mass is much smaller than their mometum, η approaches rapidity $y = 1/2\ln(\frac{E+p_L}{E-p_L})$, where p_L is the longitudinal component of the momentum. Rapidity is a useful coordinate in colliders since the number of particles produced is constant as a function of rapidity.

3.2.2 Solenoid Magnet

The CMS superconducting solenoid magnet provides a uniform 3.8 T magnetic field. The magnetic field map measured using cosmic rays is shown in Figure 3.5. With the pixel detector and silicon tracker inside this magnetic field, it is possible to measure precisely the curvature of tracks left by charged particles and therefore their momenta.

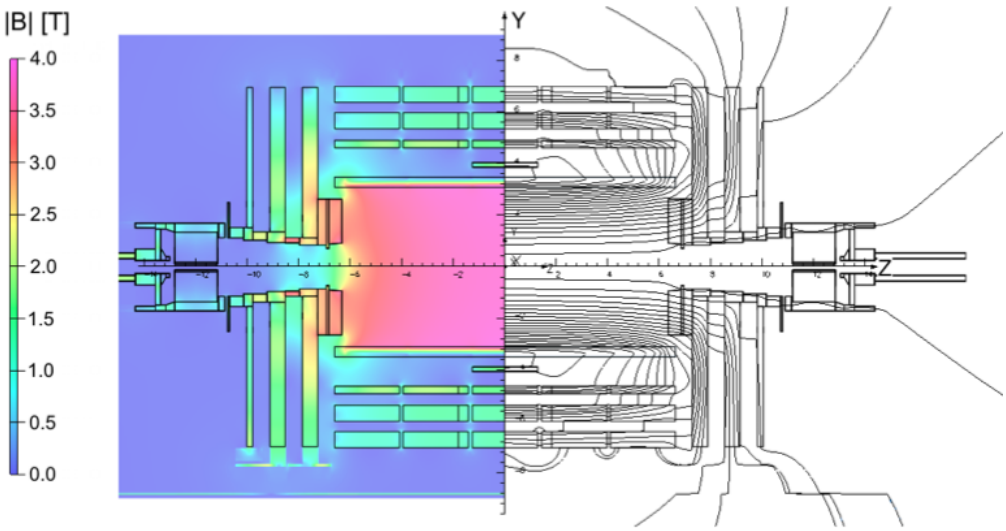

Figure 3.5: Value of the CMS magnetic field shown on the left side and the field lines are shown on the right side. The central region of the detector shows a very stable field, which makes the track reconstruction easier [43].

The magnetic field is confined by steel yoke around the solenoid. After this point, most particles have been detected or stopped by the yoke so that mostly muons make it this far.

At the beginning of Run 2 in 2015, the CMS magnet had to be turned off while collisions were happening due to a leak in the helium cooling system. The magnet could not be operated safely under these conditions. A lot of work was done to fix the leakage so the magnet could be operational during collisions and CMS could collect as much good data as possible. This problem was solved during the technical stop in the winter of 2015-2016, which allowed for the CMS magnet to operate during the full 2016 data taking period.

3.2.3 Inner Tracking System

The all-silicon tracker system is composed of an inner pixel detector and an outer strip tracker. A schematic of the tracker system is shown in Figure 3.6.

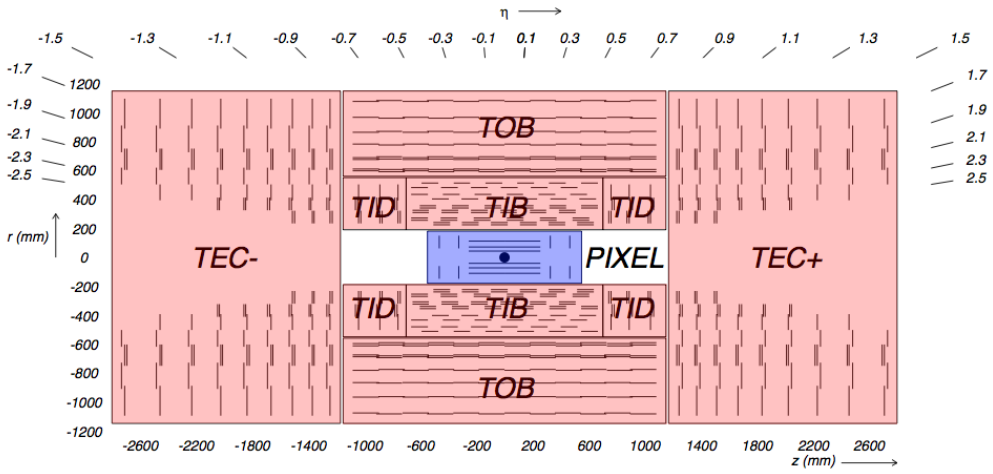

Figure 3.6: Schematic cross sectional view of the CMS tracker [38]. The inner tracker is divided into inner barrel (TIB) and disks (TID) and outer barrel (TOB) and endcaps (TEC).

Pixel detector

The pixel detector consists of three cylindrical layers at radii of 4.4, 7.3, and 10.2 cm around the beam pipe [38, 44]. In addition, there are two disks on each side at $z = 34.6$ and 46.5 cm. The layout of the pixel modules provides coverage to $|\eta| < 2.5$ and delivers on average three precise measurements of a charged particle's position along its helical path. There are approximately 66 million pixels totaling an area of about 1 m^2 of silicon.

The pixel detector sits closest to the interaction point and receives the highest doses of radiation from fast hadrons and charged particles. At the end of the

2016 run of the LHC, the pixel detector reached the end of its useful life and was upgraded in preparation for the 2017 run. The performance of the pixels for the past four years of CMS has been outstanding and has allowed for precise tracking as well as vertexing in searches with bottom quarks and tau leptons or new physics models with other displaced vertices.

The pixel detector design was driven by the goal of getting the best track position resolution possible for CMS while also having a detector that could withstand harsh radiation conditions. The pixel sensors were built using high dose n-implants on a high resistance n-substrate, which ensured high signal collection efficiency with only moderate bias voltages even after high doses of radiation.

In the barrel, the pixel detector is built from approximately 800 detector modules. A detector module is composed of a support basestrip that holds 8 to 16 read-out chips (ROC). Each ROC is bump bonded to arrays of 52×80 pixels of size 100×150 μm^2. Finally, the High Density Interconnect, a flexible low mass 3 layer PCB, is equipped with a Token Bit Manager chip in charge of controlling the read-out of the ROCs.

For the disks, the basic unit is called a plaquette. A plaquette consists of a single pixel sensor, a variable number of read-out chips, and a very-high-density-interconnect that provides power, control, and data links. The plaquettes are built in different sizes to cover the trapezoidal geometry of the disks without leaving any gaps in coverage. Figure 3.7 shows schematic designs of a barrel module and two of the disk plaquette configurations.

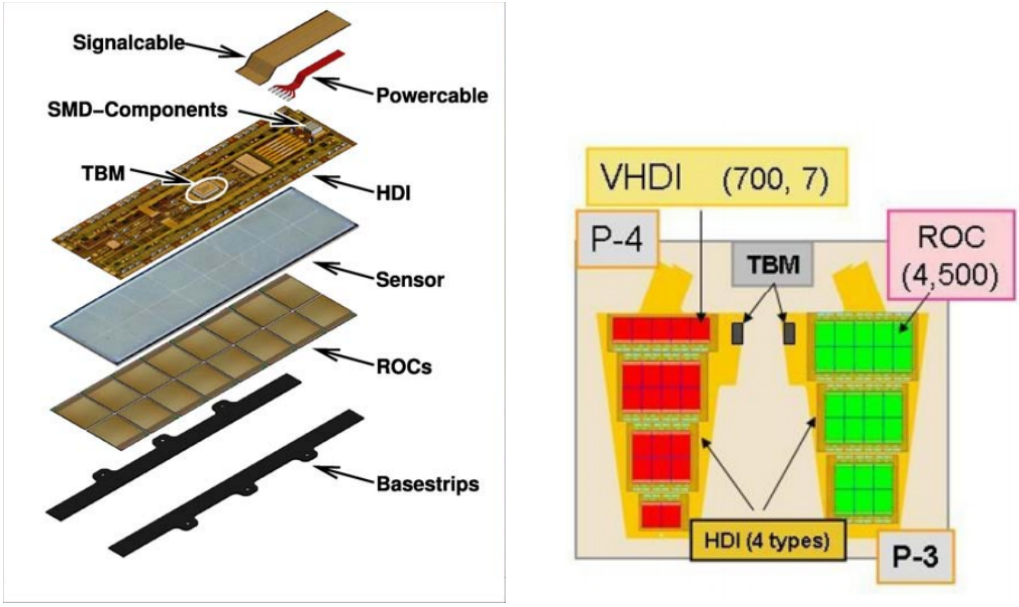

Figure 3.7: Pixel module schematics. (Left) Barrel module. (Right) Disk plaquette [38].

Silicon strip tracker

The strip tracker is divided into the Tracker Inner Barrel (TIB), Tracker Inner Disks (TID), Tracker Outer Barrel (TOB), and the Tracker End Caps (TEC) as shown in Figure 3.6 [38, 44, 45]. The sensors are made from p-on-n silicon microstrips arranged in 15 different sensor geometries to cover the entire volume. In total, the CMS tracker consists of 24,244 silicon sensors covering an effective active area of 198 m^2, making it the largest silicon tracker ever built.

The four layers of the TIB are located at r = 255.0 mm, 339.0 mm, 418.5 mm, and 498.0 mm between z = ±700 mm. The inner two layers are made of double sided sensors with a strip pitch of 80 μm, while the outer layers are single-sided sensors with a strip pitch of 120 μm. The strip side of the sensor is parallel to the beam axis, providing a position measurement in ϕ. The second sensor in the inner layers is placed with a stereo angle of 100 mrad to provide a measurement

in z. The TID consists of two sets of disks in z between ±800 mm and ±900 mm, with radii between 200 mm and 500 mm. The pitch of the modules in the TID varies from 100 μm to 141 μm. The inner two rings of each disk are also equipped with double sided sensors. The inner tracker covers up to η = 2.5 and the single point resolution in the TIB is less than 35 μm.

Surrounding the inner tracker is the TOB, which extends to a radius of 1160 mm and has a total length along the z axis of 2180 mm. The TOB consists of 6 layers, with a pitch of 183 μm for the inner four layers and 122 μm for the outer two. Capping the barrel tracker elements are the TEC with 9 disks (with up to 7 rings of sensor modules) on each side between 124 cm < $|z|$ < 282 cm and 22.5 cm < r < 113.5 cm. The inner two layers of the TOB as well as rings 1, 2, 5 of the TEC carry double sensor modules with stereo tilt as in the TIB.

The read-out system for the tracker consists of the front-end ASICs, optical links, front-end driver, control and monitoring, and power supply. The signal from the detector is amplified, shaped, and stored by the custom front-end ASIC called APV25. If the event is selected by the trigger, the signal moves through the optical links at 40 Mb/s to the front-end driver (FED) board in the service cavern above CMS. A FED board converts the analogue inputs from 96 optical fibers to digital signals using a 40 MHz, 10 bit ADC. The output of the FED are clusters with address information and signal height that can be then used for track reconstruction and physics analysis. Clocking, trigger, and control data signals are sent using optical links from a front-end controller (FEC) card also located in the service cavern.

Alignment of the inner tracker is crucial for an accurate measurement of a track's momentum. The tracker modules are aligned based on three compo-

nents: assembly data during installation, the laser alignment system, and alignment using tracks. The double sided sensors are treated as single modules for alignment purposes, and thus it is necessary to determine the three translational and three rotational parameters of 15,148 tracker modules. The position of the modules from the assembly process is known to within a few tens of μm. The module positions change over time due to changes in pressure and magnetic field, so the positions must be constantly updated. The laser alignment system uses an infrared laser to constantly monitor selected modules in the detector with a precision on tracker substructures of 100 μm. Finally, the most precise alignment can be achieved using tracks [46]. In addition to collision data, cosmic muons, either with magnetic field on or off, and beam halo tracks are also used to constrain correlations in the position parameters.

3.2.4 Electromagnetic Calorimeter

The electromagnetic calorimeter (ECAL) is used in CMS to measure the energy of electrons, photons, and π^0 mesons. The barrel ECAL (EB) covers the central region $|\eta| < 1.479$, while the endcap ECAL (EE) closes the calorimeter, covering the range $1.479 < |\eta| < 3.0$. A preshower detector (ES) is placed in front of the endcaps, covering the region between $1.653 < |\eta| < 2.6$. A cross sectional view of a quarter of the ECAL is shown in Figure 3.8.

Barrel and Endcap detector

The ECAL consists of 61,200 lead tungstate ($PbWO_4$) crystal in the central barrel and 7,324 crystals in each of the two endcaps [38, 47, 48].

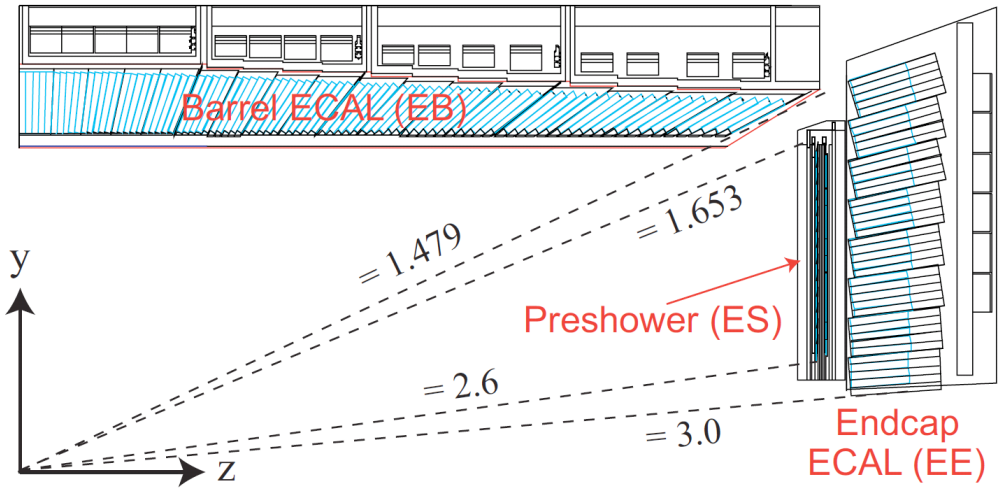

Figure 3.8: Cross sectional view of the CMS electromagnetic calorimeter [38].

$PbWO_4$ crystals were the preferred choice for a fully absorbing material because of its scintillator characteristics. Its short radiation length (0.89 cm) and small Molière radius (2.2 cm) keep electromagnetic showers relatively small, therefore providing a better position measurement. These crystals are radiation hard, a fast response time, and were able to be consistently mass produced. About 80% of the scintillation light produced in a shower is emitted in 25 ns, in time for an LHC bunch crossing. One downside of lead tungstate is its low light output and that this output varies with temperature. In order to maintain the desired energy measurement resolution, the temperature must be kept constant with very little variation. The nominal operating temperature of the ECAL is 18 ± 0.05 °C.

The crystals in the EB are mounted in a quasi-projective geometry at a radius of 1.29 m, with a 3° angle in both η and ϕ between the crystal axis and a particle's trajectory coming from the interaction point. The front face of the crystal is approximately 22×22 mm^2, the rear face is 26×26 mm^2, and each crystal extends

230 mm in length. A pair of avalanche photodiodes (APD) attached to the rear face of the crystal collect the scintillation light. The active area of each diode is 5×5 mm^2 and they are operated at a gain of 50. The amplification of the APDs is also negatively affected by temperature, which is another reason to maintain a stable temperature in the ECAL.

The endcaps are divided into two halves, each containing 3,662 crystals grouped in 5×5 mechanical units called supercrystals (SCs). The SCs are arranged to form angles ranging from 3 to 8 degrees between the crystal axis and particles coming from the interaction point. The distance from the interaction point to the endcap disks is 315.4 cm with the magnetic field turned on. The EE crystals are slightly larger with a front face area of 28.6×28.6 mm^2, a rear face area of 30×30 mm^2, and a length of 220 mm. A single vacuum phototriode (VPT) is glued to the back of each crystal for light collection. These VPTs were specially designed to operate in the 3.8 T magnetic field of CMS with an active area around 280 mm^2, and similar performance to the APDs in the barrel.

Similar to the SC in the EE, 25 crystals in the barrel are grouped in 5×5 arrays in $\eta \times \phi$. These groupings are known as trigger towers and will contribute to the Level 1 decision of the trigger. The signals from the photodetectors must be amplified, shaped, digitized, and read-out in approximately the 3 μs of trigger latency. This process all happens in the on-detector electronics.

The off-detector electronics are in charge of creating trigger primitives, collecting and buffering data, and distributing data to the trigger and the data acquisition (DAQ) systems. A trigger primitive refers to the summed transverse energy deposited in a trigger tower plus a bit describing the shape of the EM shower. The full information from the detector is collected and verified in ded-

icated boards that, if a trigger is received, send the data to the DAQ for further offline processing.

Given the large amount of data that would come from reading the full ECAL, a system of selective read-out is implemented to give priority to larger energy deposits and keep the data throughput within the allocated budget (100 kB per event). A trigger tower is deemed high interest if the measured E_T is above 5 GeV. Then the tower and its neighbors are read-out. For towers with energy above 2.5 GeV, known as medium interest, only the tower is read-out. Other towers, that are not neighbors of a high interest, are read-out with zero suppression at about three standard deviations of the base noise level ($3\sigma_{noise}$).

Preshower detector

The preshower detector (ES), located in front of the endcaps, consists of two orthogonal layers of lead radiators, each followed by a layer of silicon strip sensors. The total thickness of the ES is 20 cm, which is enough so that 95% of incident photons start showering before they reach the second sensor layer. The fine-granularity of the ES improves the position determination of electrons in the endcaps. The silicon sensors cover an active area of 61×61 mm^2 with 32 strips of 1.9 μm pitch.

3.2.5 Hadronic Calorimeter

The hadronic calorimeter (HCAL) measures the energy deposits left by outgoing hadrons, such as pions and kaons [38, 47, 49]. The HCAL is particularly

important in searches using jets and missing transverse energy. The four main components of the HCAL are: the barrel (HB), the endcaps (HE), the outer calorimeter (HO), and the forward calorimeter (HF). A cross sectional view of the HCAL is shown in Figure 3.9.

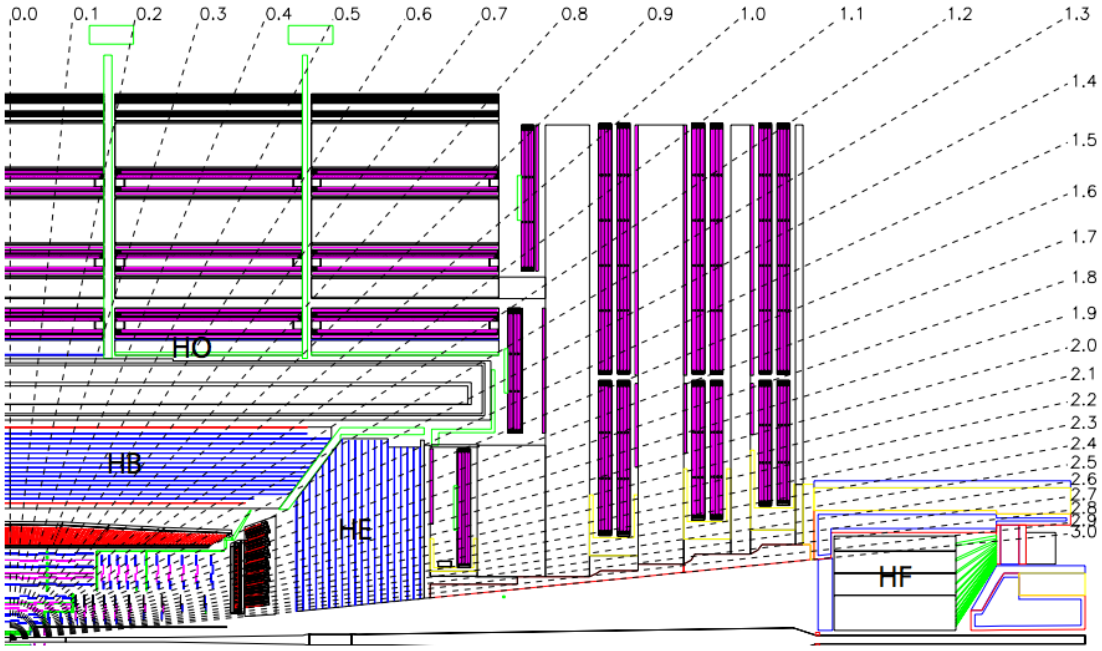

Figure 3.9: Cross sectional view of the CMS hadronic calorimeter [38]. The calorimeter is divided into barrel (HB), endcaps (HE), outer calorimeter (HO), and forward calorimeter (HF). Muon chambers are also shown in the figure.

The HB is a sampling calorimeter of plastic scintillator layers sandwiched between brass absorber plates. The innermost and outermost absorber layers are made of stainless steel for structural integrity. The HB surrounds the barrel ECAL and sits fully inside the CMS solenoid, extending to a pseudorapidity of $|\eta| < 1.3$. The HB is divided into 18 ϕ sectors called wedges. Each of these wedges is further subdivided in 4 ϕ sectors and 16 η sectors, resulting in a granularity of $(\Delta\eta, \Delta\phi) = (0.087, 0.087)$. The active material uses Kuraray SCSN81

plastic scintillator coupled to wavelength shifting fibers to bring the light to the photodetectors. An additional layer of scintillator is placed between the ECAL and the stainless steel layer to capture showers developing in this region of inert material. This initial layer and the last scintillator layer are 9 mm thick, while the other 15 layers are only 3.7 mm thick. Wavelength shifting fibers are spliced to clear fibers and brought together into read-out towers in a hybrid photodiode (HPD).

The design of the endcap calorimeter (HE) was driven by the space constraints set by the ECAL endcaps and the magnet iron yoke. Another design requirement was to minimize the cracks between the HB and the HE while still covering the pseudorapidity range $1.3 < |\eta| < 3.0$. The geometry of the HE is similar to the HB, with 18 brass absorber layers and 17 SCSN81 scintillator layers 3.7 mm thick. The layer of scintillator before the absorber is made of Bicron BC408 and it is 9 mm thick. The calorimeter is divided in 36 ϕ sectors and 13 η towers, resulting in a segmentation of $(\Delta\eta, \Delta\phi) = (0.087, 0.087)$ for $|\eta| < 1.6$ and $(\Delta\eta, \Delta\phi) \approx (0.17, 0.17)$ for $|\eta| > 1.6$. Similarly to the HB, wavelength shifting fibers collect the light and transfer the signals to hybrid photodiodes in the back of the sensors.

The two remaining components of the HCAL are the forward calorimeters (HF) and the outer barrel (HO). These additional detectors complement the HB and HE by extending the pseudorapidity coverage to $|\eta| < 5.0$ with the HF and the radial sampling depth with the HO. The HO sits after the first layer of the return iron yoke and covers the region of $|\eta| < 1.3$. It consists of a single 10 mm Bicron BC408 scintillator layer at a radial distance of 4.07 m. An additional scintillator layer in the very central region ($|z| < 2.686$ m) is added before the

magnet iron to compensate for less absorber depth in this region. In the same way as in the HB and HE, light is collected in wavelength shifting fibers that are spliced to clear fibers and brought out to HPDs.

The HF uses radiation-hard quartz fibers as the active material incased in a cylinder of steel as the absorber. The inner radius of the cylinder is 12.5 cm from the beam line, the outer radius is 130.0 cm, and the front face is located 11.2 m from the interaction point extending 165 cm along z. Each quartz fiber is 800 μm in diameter and is placed in grooves in the steel 5.0 mm apart. Half the fibers start 22 cm from the front face of the absorber. This feature helps differentiate electrons and photons from other hadrons, since e/γ objects deposit most of their energy in the first 22 cm.

The HCAL also contributes to the Level 1 decision of the trigger. The analog signals from the HPDs are digitized and sent to the HCAL Trigger/Read-out (HTR) board at 40 MHz. Level 1 trigger primitives are constructed in the HTR boards and are sent downstream to the regional calorimeter trigger to be combined with Level 1 decisions from other subdetectors. Upon a Level 1 Accept, the full data from all the sensors is transmitted to the DAQ for physics analysis.

3.2.6 Muon System

Detecting muons is a vital part of the CMS physics program since they are a signature of many searches for new physics, including the search presented in this dissertation, as well as many standard model processes. The muon system consists of approximately 25,000 m^2 of detector area covering the pseudorapidity region $|\eta| < 2.4$ [38, 47, 50–52]. In the central region, drift tubes are used for

muon detection. Cathode strip chambers are used for the endcaps and additionally a resistive plate detector covers the region $|\eta| < 1.6$. A cross sectional view of the muon system is shown in Figure 3.10.

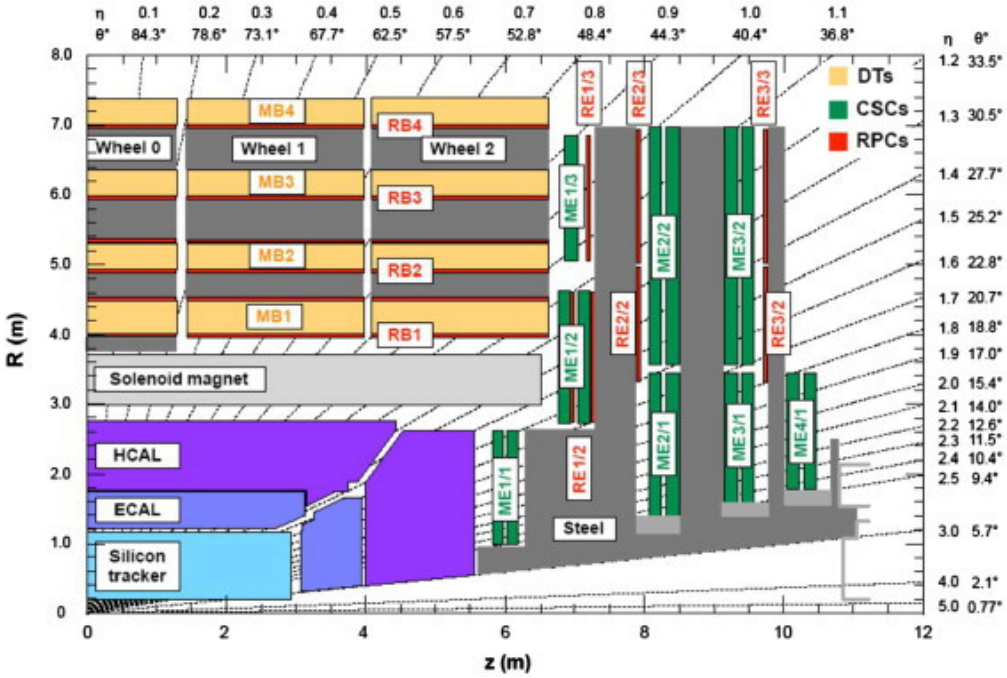

Figure 3.10: Cross sectional view of the CMS muon system [52].

Drift tubes

Four layers of drift tube (DT) stations cover the region $|\eta| < 1.2$, providing a precise measurement of a muons position as it traverses the weaker magnetic field outside the solenoid. A drift tube station is shown in Figure 3.11, along with an individual cell with a sketch of the drift lines. Each station consists of three super layers (SL) with four chambers of DTs. The DT cells inside the chambers are staggered by half a cell to avoid dead regions. The outer two of these SLs are oriented parallel to the beam direction, to provide position measurements in $r - \phi$, while the middle SL runs perpendicular to the beam to measure the z

position. The outermost stations do not have this third SL.

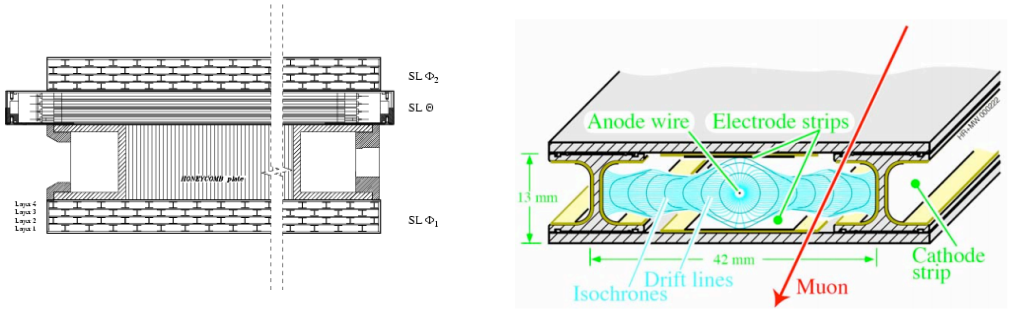

Figure 3.11: (Left) Drift tube station view in $r-\phi$ plane. Station 4 does not have an $SL\Theta$ SL to measure the z position. (Right) Sketch showing the drift lines inside the drift cell [38].

The DTs have dimensions of 13×42 mm^2 of cross sectional area and 2.4 m in length and are filled with a gas mixture of 85-15% Ar+CO_2. The resolution goal for the DTs is to measure a muon's position in $r-\phi$ to within 100 μm. This was achieved by spacing the two outer SLs with an aluminum honeycomb plate that is attached to the iron yoke. The size of the drift cell allows for a maximum drift path of 21 mm, or 380 ns in the Ar+CO_2 mixture, providing an excellent time measurement. This is particularly important for bunch crossing tagging to be used in the Level 1 muon trigger.

Front-end electronics installed directly on the aluminum honeycomb are tasked with amplifying and shaping the signal to be further processed by the read out and trigger boards. The first level of track formation is done at the front-end by correlating ϕ segments from the same bunch crossing within a chamber. The best two track candidates are sent downstream for a trigger decision. If a Level 1 Accept is received, the rest of the data is sent to the central DAQ.

Cathode strip chambers

The endcap region of the CMS muon system is instrumented with Cathode Strip Chambers (CSC). The CSCs are arranged in disks covering the pseudorapidity range $0.9 < |\eta| < 2.4$, where each trapezoidal CSC covers 10-20° in ϕ. A chamber is composed of 7 cathode strip panels alternating with 6 layers of anode wire planes. The wires are wound along the ϕ direction and provide a radial position measurement, while the strips run in the radial direction and measure the ϕ position by means of shape interpolation between multiple strips. The muon position in z comes directly from the plane position in the chamber. A diagram of a CSC is shown in Figure 3.12 as well as schematic of the interpolation principle used to precisely measure the ϕ position in the cathode strips.

In addition to the resolution requirements imposed by physics analyses and timing needs of the trigger, the CSCs has to maintain the same initial performance after 10 years of LHC running at the designed luminosity in the much harsher forward region. This led to a design that is radiation hard, it is not much affected by non-uniform magnetic fields, and does not need precise pressure and temperature control. The CSCs operate with a gas combination of 40-50-10% Ar+CO_2+CF_4 at atmospheric pressure with the anode wires set at a voltage of 3.6 kV.

The fast and precise measurements in the CSCs are used in the Level 1 trigger decision by performing a coarse track reconstruction in each chamber. A dedicated Field Programmable Gate Array (FPGA) board tries to find patterns of hits in the 6 cathode planes that would be consistent with a muon coming from the interaction point. These valid patterns are found within 225 ns and are sent as trigger primitives to form muon candidates. A second set of trigger

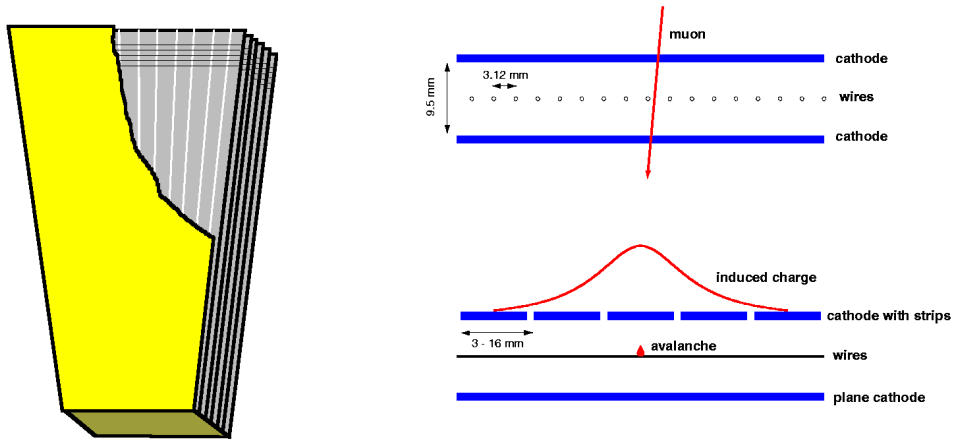

Figure 3.12: (Left) Schematic of a muon cathode strip chamber. (Right) Cross sectional view of a single gap in the CSC illustrating the charge induction principle [38].

primitives is formed in a comparator board that also looks for valid patterns, but uses a comparator circuit to determine the hit positions within a half-strip resolution. The combination of the two sets of trigger primitives is sent on to the Level 1 muon trigger and is used in the Level 1 Accept decision. If a Level 1 Accept is received before 3.2 μs, the full data from the CSCs is sent to the central DAQ.

Resistive plate chambers

The Resistive Plate Chambers (RPCs) provide a very precise timing measurement of a muon (much smaller than 25 ns) at the cost of coarse position deter-

mination. The RPCs are embedded in the iron yoke as seen in Figure 3.10 and cover the pseudorapidity region $|\eta| < 1.6$.

Each RPC consists of a double-gap module with common pick-up read-out strips and is filled with 95.2% Freon + 4.5% isobutane + 0.3% hexafluoride gas and water vapor. The RPC trigger system receives unsynchronized signals from the front-end boards; these signals are synchronized to the LHC clock and sent over optical fibers for reconstruction. Muon candidates are formed from the combination of RPC signals that are consistent with a track coming from the interaction point.

3.2.7 Trigger and Data Acquisition System

The LHC reached its designed instantaneous luminosity of 10^{34} $cm^{-2}s^{-1}$ in 2016, with an average of 20 proton-proton interactions per bunch crossing. At a crossing frequency of 40 MHz, the detectors see on average an input data rate of 1 GHz. It is impossible to store that much information; the computer farm where the events are recorded can handle up to 400 Hz. This rate reduction of over 6 orders of magnitude is at the limit of the trigger design and will need to be reworked for the time of the high luminosity upgrade of the LHC, but has performed well through Run 2.

The events that are recorded must be carefully selected so they are likely to be coming from interesting physics. Most of the collisions in a bunch crossing are very soft and produce interactions that are not interesting. These are not the type of events that we want to study in CMS, but rather we are interested in much rarer processes like Higgs production and possible physics beyond the

SM. In order to achieve the rate reduction necessary for data processing and to select only the most interesting events, the trigger system is designed as a two-step process with a hardware component (Level 1) and a software component (High Level Trigger) [38, 53].

Level 1 trigger

The Level 1 (L1) hardware trigger is the first stage of the trigger system. It makes the decision to keep an event within 3.2 μs using coarse information from the calorimeters and the muon system. The decision process is shown in Figure 3.13. Local decisions are made by each system before the events are sent to the Global Trigger (GT), where the information is combined and a L1 decision is made for each bunch crossing.

As mentioned in the above description of the calorimeters, the front-end electronics generate trigger primitives from energy deposits and send them to a Regional Calorimeter Trigger (RCT). The RCT organizes these energy measurements into e/γ candidates and pseudo-jets from regional energy deposits before sending them to the Global Calorimeter Trigger (GCT). In the GCT, the electromagnetic candidates are further selected, better jets are constructed using simple clustering algorithms [54, 55], and global quantities are computed including the missing transverse energy. The output jets, e/γ candidates, and taus are sent to the GT to be combined with the L1 muon trigger for a final decision.

The three components of the muon system participate in the trigger decision. On-detector electronics in the DTs and CSCs create muon candidates using pattern recognition of track segments in the chambers assuming muons coming

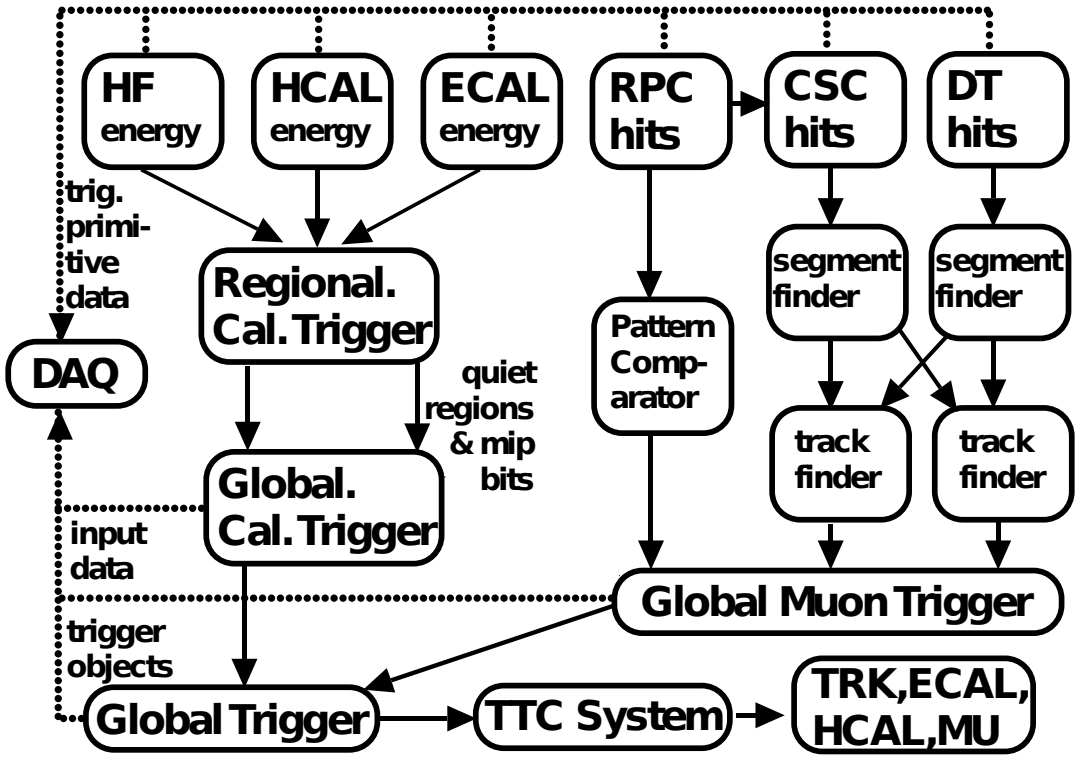

Figure 3.13: Schematic of the CMS L1 trigger system [53].

from the interaction point. Information is shared between the DT track finder and the CSC track finder in the overlap region. Up to 4 muon candidates from the DT/CSC track finders and 8 candidates from the RPC pattern comparator are sent to the Global Muon Trigger (GMT). The GMT combines this information to remove duplicates and assigns a quality rating before sending muons candidates to the GT.

FPGAs are used to implement the trigger logic that will decide if an event is passed to the HLT. Configurable trigger menus are updated during data collection to keep rates at an acceptable level. The maximum output rate of the L1 trigger is 100 kHz, which is divided between the different trigger paths. If

the rate for a given path is too high, the typical strategies are to either prescale the number of events that pass the trigger and throw away events, or raise the momentum thresholds of physics objects at the cost of losing the low energy objects. Unfortunately, reducing the rate by raising the threshold does not work for higher instantaneous luminosities like those expected in the high luminosity upgrade of the LHC. Studies have shown [56] that tracker information must be included in the L1 decision of the trigger to keep rates down. A tracking algorithm that can be implemented in hardware is presented in Appendix A.

High Level Trigger

The final decision to keep an event is made by the HLT. It relies on a better object reconstruction of objects than at L1, using algorithms similar to the offline processing. A farm of approximately 13,000 commercial CPU cores filter events from the L1 at a rate of 100 kHz down to about 400 Hz. Each event is processed in under 200 ms, after which accepted events are sent to the data storage system.

Data acquisition system

After a L1 accept, the data from all the subsystems must be transferred to the computing farm. This corresponds to a data rate of roughly 100 GB/s from more than 600 sources. The data is processed by the Event Filter before moving to the HLT filter systems and, if accepted, it is stored on tape at the CERN data center for offline processing.

3.2.8 Reconstruction and Generation Software

Monte Carlo simulation of standard model and new physics processes is done using different generator packages (PYTHIA [57], MADGRAPH [58], POWHEG [59]). These packages implement a rigorous description of SM processes as well as phenomenological models to be tested at colliders, including the Left-Right symmetry model discussed in Section 2. These generation tools are typically developed by theorists to implement and test their models using simulated events and made available to experimentalists. To use the output of these generators in a physics analysis, it must be processed through the full CMS software simulation and reconstruction software.

The software suite used in CMS for event reconstruction and physics analysis is called CMSSW [47]. The full simulation of particles going through the detector material is done using GEANT4 [60]. The resulting output format of the detector simulation is the same as the raw data coming from the detector DAQ. The simulation can then be processed by the same reconstruction algorithms as the data.

The event reconstruction takes place in three stages: local reconstruction within a detector module, global reconstruction within a detector (i.e. ECAL, muon system, etc.), and finally combining reconstructed objects into high-level objects. A detailed description of the reconstruction of the objects used in the search described in this dissertation is presented in the following Section.

CHAPTER 4

OBJECT RECONSTRUCTION

In this Chapter, we give a description of the reconstruction and identification of the physics objects used in the search described in this dissertation. We begin by describing track reconstruction in Section 4.1. In Section 4.2 we describe muons and electrons in Section 4.3. We conclude by discussing jet reconstruction in Section 4.4. Additional information about object reconstruction can be found in Reference [47].

4.1 Tracks

As discussed in Section 3.2.3, the CMS tracker covers an effective area of almost 200 m^2 with silicon sensors and provides high quality, high resolution position measurements of charged particles traversing the detector. The hardware is complimented by dedicated software algorithms to achieve the best performance. This is particularly important at the level of the current instantaneous luminosity delivered by the LHC, where there are on average 2000 tracks per event. Track information is used in the reconstruction of all the objects used in our search.

Track reconstruction is performed in steps [47]: hit reconstruction and seed generation, track finding, fitting, and selection. Hits in the pixel and the strip tracker are reconstructed from zero-suppressed signals from the detectors to provide a position measurement with its uncertainty. In the pixels, clusters are formed by combining adjacent pixels and the cluster position is calculated on the sensor plane by a weighted average of the charge collected in each pixel. In

the strip detector, hit seeds from a strip are combined with the charge of neighbor strips to form clusters. The position is determined as the charge-weighted strip position.

The next steps in track reconstruction are performed iteratively using the Combinatorial Track Finder (CTF) software [45]. The hits used for the tracks in each iteration are removed in subsequent iterations, making it less computationally demanding and allowing the reconstruction of harder-to-find low momentum and displaced tracks. On the first iteration the prompt tracks are reconstructed, those with high p_T and coming from the interaction point. The second iteration reconstructs low p_T tracks that come from the interaction point. The remaining iterations reconstruct displaced tracks that usually come from a secondary vertex.

A charged particle moving in a uniform magnetic field follows a helix and thus, five parameters are needed to determine the particle's trajectory. A first set of parameters can be estimated from three 3D points called a track seed. Given the high granularity and resolution of the pixel sensors, the seeds are usually made from three pixel hits, or two pixel hits together with the beamspot as constraint. If the parameters estimated from the seed are consistent with those of a good track, the seed is accepted and it is used for track finding.

Track finding in the CTF algorithm is based on the Kalman Filter method [61–63]. The track parameters estimated by the coarse seed generation are updated by adding hits consistent with the predicted trajectory. The parameters are updated at each layer by taking into account multiple scattering effects and energy loss. A single seed can produce multiple track candidates, since at each layer there can be multiple compatible hits. To prevent a combinatorial

explosion, only 5 candidates are considered at each step.

When all hits compatible with a track are collected, a final refit is performed to calculate the track parameters using all the information available and without possible bias from the interaction point constraint. A Kalman Filter method is used to refit the track by starting with a four-hit seed and updating as new hits are added. The precision is optimized by using a Runge-Kutta propagator [64] to take into account the detector material and the inhomogeneous magnetic field. The final selection removes many of the fake tracks produced in the track finding step. Requirements on the number of hits, the quality of the fit, and the parameter significance can reduce considerably the number of duplicated and fake tracks.

Tracks are also used to determine the position of the interaction vertices in collision events. A collision vertex is reconstructed from clustered tracks that appear to be coming from the same z-coordinate. The full 3D position of the vertex is then fitted from the clustered tracks. The z-coordinate can then be used to distinguish particles from the hard interaction vertex from those additional pileup interactions.

4.2 Muons

Muons in CMS are reconstructed in two complimentary approaches: inside-out and outside-in [52]. The inside-out reconstruction uses all the tracks formed in the inner tracker as muon candidates. If the tracker track is matched to at least one muon segment either in the DTs of the CSCs, it is called a tracker muon, with momentum and vertex measured using the tracker only. The outside-in

reconstruction starts with a track in the muon system and looks for a matching tracker track. If a compatible track is found, a global muon is fit using the combined set of hits from the tracker and the muon system, using the Kalman Filter method to estimate the track parameters. Tracker muon reconstruction is more efficient for lower momentum muons ($p < 5$ GeV) because it does not rely on the muon making it past the first muon station, while a global muon reconstruction expects the muon to penetrate through multiple muon stations.

Dedicated algorithms for high momentum muon reconstruction were developed to take into account the showering from interactions in the muon chambers for muons above the critical energy in the iron. Starting from a global-muon, the *Tracker-Plus-First-Muon-Station (TPFMS)* algorithm uses only the information from the innermost station containing hits in the muon system. The second algorithm, called *the Picky fit*, uses all the hits from the global-muon in the fit, but it can discard those that are not consistent with the muon track based on the χ^2. More recently, the *Dynamic Truncation fit (DYT)* was developed as an extension of the TPFMS algorithm to include more muon stations in the fit as long as they are still compatible with a muon track.

Each of the algorithms presented above provides a momentum estimate for the muon. The *TuneP* algorithm then chooses between the tracker-only, global, TPFMS, Picky, and DYT fits for the best estimate for each muon's momentum. For muons with $p_T < 200$ GeV, the algorithm chooses the assignment of the tracker-only fit. Above this momentum, the algorithm starts with Picky assignment and compares the goodness of the fit with the other fits. TuneP will only use the other fits if the improvement is significantly better. In the search for a W_R presented in this dissertation, we use the momentum assignment of muons

from the TuneP algorithm.

4.2.1 Muon identification algorithm

An optimized identification algorithm was developed to select high momentum muons, like those used in the W_R search, without relying on information from the calorimeters. The algorithm, called *isHighPtID*, requires the muon candidate to be a global muon. It must have hits in at least two muon stations and one muon hit must have been used in the global fit. The assigned momentum must be well measured (relative error $< 30\%$). The vertex position must be close to the interaction point to remove muons from cosmic rays. To ensure a good p_T measurement, the muon must have at least one pixel hit and at least five strip hits in the tracker. A study of the momentum resolution of muons using cosmic rays in 2016 data is presented in Appendix B.

4.3 Electrons

Electrons are reconstructed from the combination of a track in the inner silicon tracker and an energy cluster in the ECAL. Dedicated algorithms are used to reconstruct the tracks used in electrons [65], since the track reconstruction described above is not optimal for highly radiative particles. Electron tracks kink due to energy loses from bremsstrahlung causing the standard track reconstruction to lose hits further along the trajectory. A dedicated track reconstruction is used to recover these hits and provide a better estimate of the track parameters. Two complimentary seeding algorithms for the dedicated tracking are used for

electrons: ECAL based seeding and tracker based seeding.

ECAL seeding starts from a supercluster (SC) of energy deposits. Contiguous 5×1 arrays of crystals in $\eta \times \phi$ are added into clusters if the energy of the array is above a configurable threshold. The electrons bending in the magnetic field bremsstrahlung and the emitted photons deposit their energy in a spread of crystals along ϕ with little spread in η. This helps distinguish electrons from photons in the ECAL. The clusters of arrays are combined if they pass a requirement into a single SC. SCs in the endcaps are formed from multiple 5×5 crystal arrays since the crystals are not arranged in a projective geometry.

The SC energy is the sum of the energy measured in the clusters and the position at the face of the calorimeter is calculated as an energy-weighted mean corrected by the depth of the shower. The position of the SC is used to estimate the trajectory of the electron, assuming it came from the collision point. The hits predicted by the SC projection are compared with tracker seeds hits to reduce the computing load of trying fake combinations. Tracker based seeding uses multiple variables [66] to select seeds, using information from a Kalman filter track reconstruction, ECAL information, and the dedicated electron track reconstruction.

Electron tracking starts with a Kalman filter approach, which works fine when bremsstrahlung is negligible, but otherwise produces low quality tracks. Instead, a dedicated Gaussian sum filter (GSF) [67] algorithm is used to refit the tracks. By including the information about energy loss at each layer into the track reconstruction, the GSF algorithm performs better than the Kalman filter. GSF tracks are then associated with ECAL clusters by a geometrical matching or an MVA technique. For electrons above 15 GeV, the best momentum estimate

comes from the ECAL measurement alone.

4.3.1 Electron identification algorithm

Several electron identification algorithms are available and are optimized for particular event topologies. In the W_R search presented in this dissertation, we use an algorithm designed to select high momentum electrons, known as *High Energy Electron Pairs (HEEP)* identification. The algorithm takes into consideration the shape and quality of the ECAL supercluster, as well as the track information to determine isolation and a possible production vertex. Electrons must have $p_T > 35$ GeV and the pseudorapidity of the SC must be within the acceptance of the ECAL. The energy fraction in the hadronic calorimeter must be much smaller than the ECAL measurement. Finally, the electrons must be isolated from other tracks and calorimeter deposits.

4.4 Jets

Quarks and gluons are not directly detectable due to color confinement, but rather must be inferred from the hadronic showers they produce. These stable hadrons can be seen in detectors as tracks and energy clusters in the calorimeters. The collection of charged and neutral hadrons is called a jet and there are multiple algorithms to reconstruct them [54, 55]. Jet reconstruction is done as part of the particle-flow [68] event reconstruction, which uses information from all the subdetectors to provide a complete picture of each event. The best estimate for global event quantities, such as the missing transverse energy, is also

obtained from the particle-flow reconstruction.

The particle flow (PF) algorithm works by linking fundamental elements into blocks that are then interpreted as particles, where the fundamental elements are tracks, calorimeter deposits, and muon tracks. Charged hadrons make up approximately two thirds of the energy in a jet and thus, the tracker information is crucial to the energy measurement. As described in Section 4.1, an iterative track reconstruction yields the high efficiency and low fake rate needed for the event reconstruction; this is particularly true when tracking in the dense jet environment. Calorimeter clusters are independently formed in each subdetector from high energy seeds, corresponding to single cells in the subdetectors, which are grown by adding neighboring cells with energy above a threshold.

The PF elements are then linked by extrapolating tracks from their outermost position to the calorimeters and looking for nearby clusters, or by projecting an ECAL cluster to the less granular HCAL to find matching deposits. High level objects like electrons, muons, photons, and jets are then formed from these candidates. Jets are clustered from candidates by iteratively adding those that are within a certain distance from a seed, where the distance can be defined to take into account the energy of the candidate.

The energy of a jet is then taken as the sum of the energies of its constituents. The resulting energy is corrected to get a better estimate of the true energy of the particle. These corrections include pileup mitigation and removal of η and p_T-dependent detector response. These corrections are applied to both data and Monte Carlo simulation. Finally, an additional correction is applied to data only to correct for the small, remaining differences with the simulation.

4.4.1 Jet identification algorithm

In order to avoid selecting low quality jets or leptons that are misreconstructed as jets, we use a dedicated identification algorithm. A well reconstructed jet will have a considerable fraction of its energy coming from charged hadrons, so the fraction from neutrals must be less than 90%. The jets must have at least one constituent. Jets that include a muon are rejected and to reject jets faked by electrons the fraction from charged constituents using ECAL information must be less than 90%. These criteria were shown to identify jets with an efficiency of over 99% in the beginning of Run 1 [69], and the same level of performance was seen in the data collected in 2015.

CHAPTER 5

SEARCH FOR A HEAVY RIGHT-HANDED W IN THE FINAL STATE WITH TWO CHARGED LEPTONS AND TWO JETS

In this Chapter we describe the search for a right-handed W (W_R) using the data collected with the CMS detector in 2016. As discussed in Chapter 2, the Left-Right symmetry model does not predict the coupling strengths of the right-handed W or its mass. For our search we assume that the W_R is massive ($M_{WR} \gg M_{WL}$) and its couplings are the same as those of the SM W boson.

The W_R can decay in many ways, but we focus on a final state with two same flavor leptons and two jets. We only consider first and second generation leptons (electrons and muons) in our final state. The Feynman diagram of the W_R decay is shown in Figure 5.1.

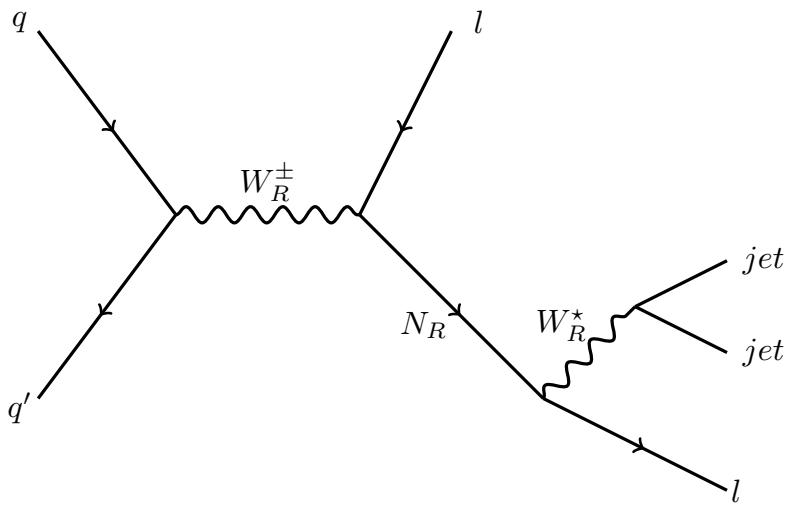

Figure 5.1: Feynman diagram of W_R decay chain.

All the final state particles can be detected and thus we can reconstruct W_R candidates by adding the four-vector momenta of our two leptons and two jets. We

can then scan the masses of our candidates and look for a resonance. The W_R would manifest as a bump in the distribution (bump-hunt) of the four-object mass.

As mentioned in Chapter 2, this bump-hunt can be reinterpreted through different theory models. We decided to keep our event selection as broad as possible and did not try to optimize particular cuts based only on the W_R signal. This is particularly important since careful study of the event kinematics in the Run 1 excess showed that these events did not look like right-handed W decays.

We begin the description of our search in Section 5.1 where we present the datasets used, then in Section 5.2 we continue with a discussion of the trigger and event selection. In Section 5.3, we compare the data with the Monte Carlo simulation. We describe our background estimation methods in Section 5.4. The statistical treatment procedure is presented in Section 5.5. We conclude with the results of our search in Section 5.6.

5.1 Datasets

In Table 5.1 we summarize the datasets used in our search for muon and electron final states.

A dedicated team in CMS provides a measurement of the integrated luminosity that is recorded when all subdetectors were operational. In 2016, CMS collected 35.9 fb^{-1} of proton-proton collisions at center of mass energy of 13 TeV. During the Run2016A era, a brief period at the beginning of the 2016 run, the CMS magnet was off and this data is not usable in our search.

Dataset	Run range	$\int \mathcal{L}dt$ (fb^{-1})
/SingleMuon/Run2016B-03Feb2017_ver2-v2	272007-275376	5.93
/SingleMuon/Run2016C-03Feb2017-v1	275657-276283	2.65
/SingleMuon/Run2016D-03Feb2017-v1	276315-276811	4.35
/SingleMuon/Run2016E-03Feb2017-v1	276831-277420	4.12
/SingleMuon/Run2016F-03Feb2017-v1	277772-278808	3.19
/SingleMuon/Run2016G-03Feb2017-v1	278820-280385	7.72
/SingleMuon/Run2016H-03Feb2017_ver2-v1	280919-	8.64
/SingleMuon/Run2016H-03Feb2017_ver3-v1	-284044	0.22
/DoubleEG/Run2016B-03Feb2017_ver2-v2	272007-275376	5.93
/DoubleEG/Run2016C-03Feb2017-v1	275657-276283	2.65
/DoubleEG/Run2016D-03Feb2017-v1	276315-276811	4.35
/DoubleEG/Run2016E-03Feb2017-v1	276831-277420	4.12
/DoubleEG/Run2016F-03Feb2017-v1	277772-278808	3.19
/DoubleEG/Run2016G-03Feb2017-v1	278820-280385	7.72
/DoubleEG/Run2016H-03Feb2017_ver2-v1	280919-	8.64
/DoubleEG/Run2016H-03Feb2017_ver3-v1	-284044	0.22

Table 5.1: Primary datasets used in the search.

Drell-Yan production of two leptons plus additional jets is simulated with PYTHIA in bins of the Z/γ^* transverse momentum and bins of the scalar sum of the jets' transverse momentum. Each of these samples has its own cross section that is calculated to next-to-leading order (NLO) by the simulation generation group. The NLO and next-to-next-to-leading order (NNLO) cross sections for the inclusive sample are also provided by the FEWZ generator [70]. We can calculate a ratio of NLO to NNLO inclusive cross sections and use it to estimate the NNLO cross sections for the binned samples. Monte Carlo generators for Drell-Yan simulation were studied in 2015 [71] (AMC@NLO, MADGRAPH, and POWHEG) and we saw that the best modeling of the additional jets is done by AMC@NLO, but the lack of statistical power led to the choice of using MADGRAPH.

This result was confirmed in 2016, where we compared a MADGRAPH sample with AMC@NLO. The MADGRAPH sample was generated in bins of the scalar sum

of all jets transverse momentum, while the AMC@NLO sample was generated in bins of the transverse momentum of the Z/γ^*. The results from this comparison are shown in Figure 5.2. These results correspond to events in a control region dominated by Drell-Yan events with the full analysis selection applied. The AMC@NLO provides a better description of the data and thus we use this sample for the Drell-Yan background estimate.

The $t\bar{t}$ sample is simulated using PYTHIA with only dilepton events produced for the top-antitop decays. Diboson, W+jets, and single top samples are simulated using MADGRAPH. All Monte Carlo samples are generated using the best estimate for the pileup conditions expected from the 2016 data taking. The small remaining differences are corrected by applying a data-driven scale factor to the simulation.

As mentioned before, we consider a heavy W_R signal in the context of the Left-Right symmetry model. This is one of the available models in the PYTHIA8 [57] generator, with the W_R and right-handed neutrino masses left as free parameters. As the baseline of our search, we chose the neutrino mass to be half of the W_R mass. Fully simulated and reconstructed samples are generated for signal points with W_R masses from 800 GeV to 6000 GeV in steps of 200 GeV.

We also consider signal points where the neutrino mass is not half the W_R mass. For these samples, we only simulate the parton showering without any detector effects. This simplifies the production process at the cost of neglecting resolution effects and detector interactions, but still provide a model for the relevant kinematic properties of the W_R decay. The efficiency to select events with our baseline selection is not optimal for these samples. The kinematics of the final state particles depend on the ratio of the W_R and N_R masses and should

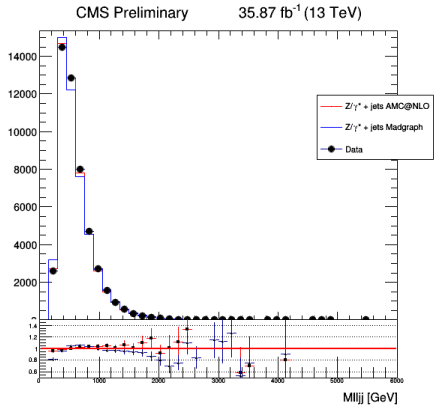

(a) Electron channel M_{lljj}.

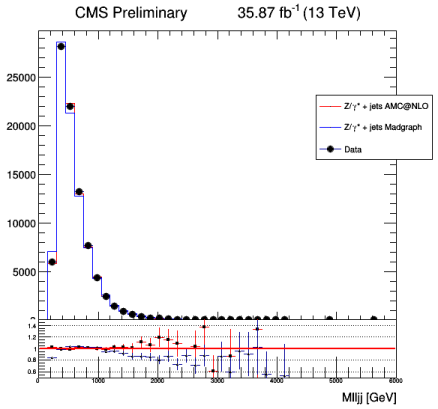

(b) Muon channel M_{lljj}.

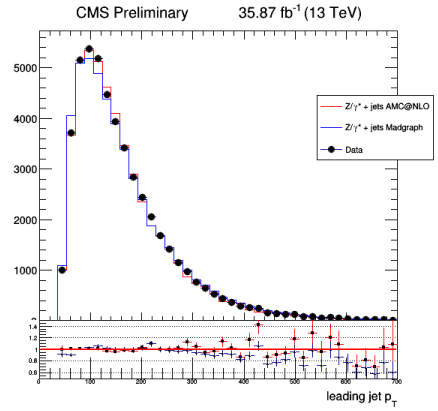

(c) Electron channel leading jet p_T.

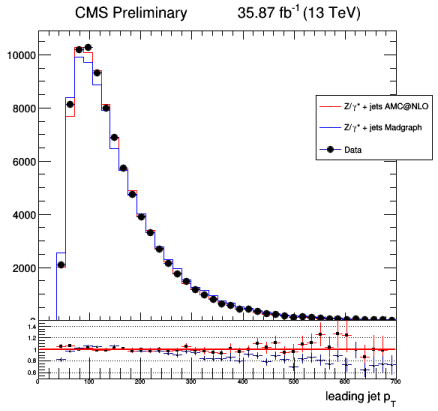

(d) Muon channel leading jet p_T.

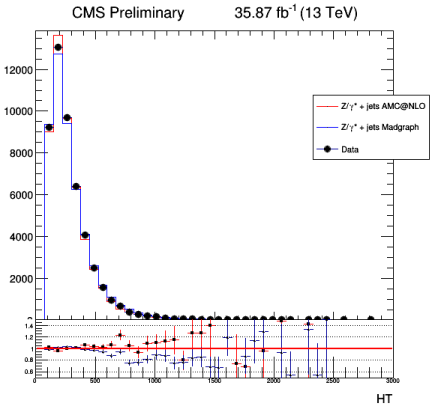

(e) Electrons channel scalar sum of jet p_T.

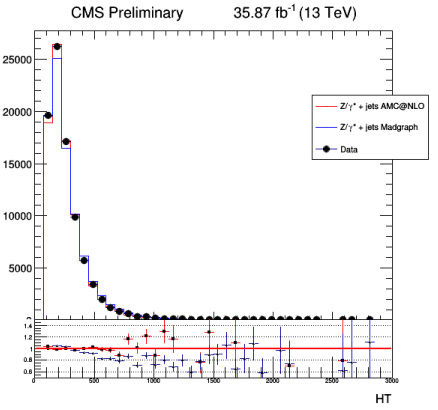

(f) Muons channel scalar sum of jet p_T.

Figure 5.2: Comparison between the data and the Drell-Yan simulated samples. Distributions correspond to events in a Drell-Yan enriched control region: dilepton mass is below 200 GeV.

be reoptimized to recover the loss in efficiency. This reoptimization is beyond the scope of this dissertation, but it is being pursued by our collaborators at the University of Minnesota as an extension to the analysis.

The standard model Monte Carlo simulation samples that we used in this analysis are presented in Table 5.2 with their corresponding cross section and dataset size.

5.2 Event selection

The search for the W_R can be done separately for first and second generation leptons, but given the similarities in the analysis of the data we decided to perform both searches in parallel. We will present the common features as well as the unique requirements in each case. We begin with the triggers used to select events and we conclude with the offline cuts.

5.2.1 Triggers

The leptons in the final state carry a large fraction of the rest energy of the W_R. Thus, a trigger with a moderately high momentum requirement on the lepton is still highly efficient for our signal. We use single muon triggers for the muon channel and for the sideband used for $t\bar{t}$ estimation, while for the electrons we use a double electron trigger with slightly lower momentum thresholds. A description of each of these triggers is presented below.

- Muon triggers: The logical OR of HLT_Mu50 and HLT_TkMu50 is required

Sample	Dataset	σ(pb)	N Events
Drell-Yan	DYJetsToLL_Pt-50To100_TuneCUETP8M1_13TeV-amcatnloFXFX-pythia8	3.47e+02	130 M
	DYJetsToLL_Pt-100To250_TuneCUETP8M1_13TeV-amcatnloFXFX-pythia8	8.13e+01	83 M
	DYJetsToLL_Pt-250To400_TuneCUETP8M1_13TeV-amcatnloFXFX-pythia8	2.98e+00	21 M
	DYJetsToLL_Pt-400To650_TuneCUETP8M1_13TeV-amcatnloFXFX-pythia8	3.84e-01	1.6 M
	DYJetsToLL_Pt-650ToInf_TuneCUETP8M1_13TeV-amcatnloFXFX-pythia8	3.56e-02	1.6 M
	DYJetsToLL_M-50_HT-70to100_TuneCUETP8M1_13TeV-madgraphMLM-pythia8	1.72e+02	9.6 M
	DYJetsToLL_M-50_HT-100to200_TuneCUETP8M1_13TeV-madgraphMLM-pythia8	1.47e+02	2.7 M
	DYJetsToLL_M-50_HT-200to400_TuneCUETP8M1_13TeV-madgraphMLM-pythia8	4.10e+01	0.9 M
	DYJetsToLL_M-50_HT-400to600_TuneCUETP8M1_13TeV-madgraphMLM-pythia8	5.70e+00	1.1 M
	DYJetsToLL_M-50_HT-600to800_TuneCUETP8M1_13TeV-madgraphMLM-pythia8	1.35e+00	8.2 M
	DYJetsToLL_M-50_HT-800to1200_TuneCUETP8M1_13TeV-madgraphMLM-pythia8	6.29e-01	2.7 M
	DYJetsToLL_M-50_HT-1200to2500_TuneCUETP8M1_13TeV-madgraphMLM-pythia8	1.51e-01	0.5 M
	DYJetsToLL_M-50_HT-2500toInf_TuneCUETP8M1_13TeV-madgraphMLM-pythia8	3.66e-03	0.4 M
$t\bar{t}$	TTJets_Dilept_TuneCUETP8M2T4_13TeV-amcatnloFXFX-pythia8	7.8e+01	68.2 M
W+Jets	WJetsToLNu_TuneCUETP8M1_13TeV-madgraphMLM-pythia8	5.02e+04	57 M
Diboson	WZ_TuneCUETP8M1_13TeV-pythia8	2.34e+01	2.9 M
	ZZ_TuneCUETP8M1_13TeV-pythia8	1.01e+01	1.0 M
	WW_TuneCUETP8M1_13TeV-pythia8	6.43e+01	0.7 M
Single Top	ST_tW_antitop_5f_inclusiveDecays_13TeV-powheg-pythia8_TuneCUETP8M1	3.81e+01	6.9 M
	ST_tW_top_5f_inclusiveDecays_13TeV-powheg-pythia8_TuneCUETP8M1	3.81e+01	7.0 M
QCD	QCD_Pt-20toInf_MuEnrichedPt15_TuneCUETP8M1_13TeV_pythia8	2.688e+05	22 M

Table 5.2: Standard model Monte Carlo samples used in the search.

to select an event. As the name suggests, a p_T cut of 50 GeV is applied on the HLT muon object. The second trigger requires that a tracker track is associated to hits in the muon system. We chose this trigger combination because it had the lowest p_T threshold, it was unprescaled for the entire 2016 data period, it was not restricted in η beyond detector acceptance, and it did not require any online isolation.

This trigger is seeded by the OR of two L1 trigger paths: L1_SingleMu22 and L1_SingleMu25. The latter path was in place as a backup in case the former had to be prescaled at any point in the run. The impact of a higher p_T threshold at L1 is expected to be minimal for our W_R signal.

Due to technical issues with the L1 and L2 muon trigger system track finding, especially in the endcap muon Track Finder, small drops in efficiency were reported. The main issue, which affected 15.4 fb^{-1} of the data collected, came when two muons were in the same sector of the same endcap, resulting in only one that fires the trigger. This was fixed for the remainder of the data collection, and recipes to correct the simulation efficiency were provided by the Muon Physics Object Group (POG).

The inclusion of the second HLT trigger (HLT_TkMu50) came during RunB as a complementary path. This path relies on a different reconstruction of the online muon. Starting from a L1 seed, iterative tracking is performed in a region defined by the seed and then muon hits are required to be associated to the track. This additional trigger path was shown to improve the performance for dimuon events, and the combination of the two paths was recommended.

- Electron triggers: The main HLT path used for the analysis was HLT_DoubleEle33_CaloIdL_MW, which requires two electrons each with

$p_T > 33$ GeV, and each must have an associated ECAL deposit and a track with a pixel hit. This trigger was developed as an improvement on a previous version, HLT_DoubleEle33_CaloIdL_GsfTrkIdVL. Unfortunately, due to a misconfiguration in the HLT_DoubleEle33_CaloIdL_MW path, where only one of the electrons was required to pass the pixel matching, the path had to be prescaled to maintain acceptable rates. A fix for the trigger came later in the data taking, but for the runs affected we had to use the HLT_DoubleEle33_CaloIdL_GsfTrkIdVL path. This trigger required a very loose GSF track matching to the ECAL deposit instead of a pixel requirement.

Both triggers used for electrons are seeded by the same set of L1 triggers: DoubleEG, SingleEG, SingleJet, and SingleTau. The thresholds for these triggers were quite complicated and changed with time during data taking. These thresholds are well below our offline requirements and thus, we are not affected by the changing in prescales. The single jet and tau triggers are used in case of a drop in efficiency in the EG paths due to very energetic seeds. The lowest unprescaled threshold for the SingleEG path was 40 GeV, while for the DoubleEG they were 24 and 17 GeV respectively.

The efficiency of the triggers for our signal with respect to our offline selection is shown in Figure 5.3. Both sets of triggers are nearly 100% efficient in selecting our signal events.

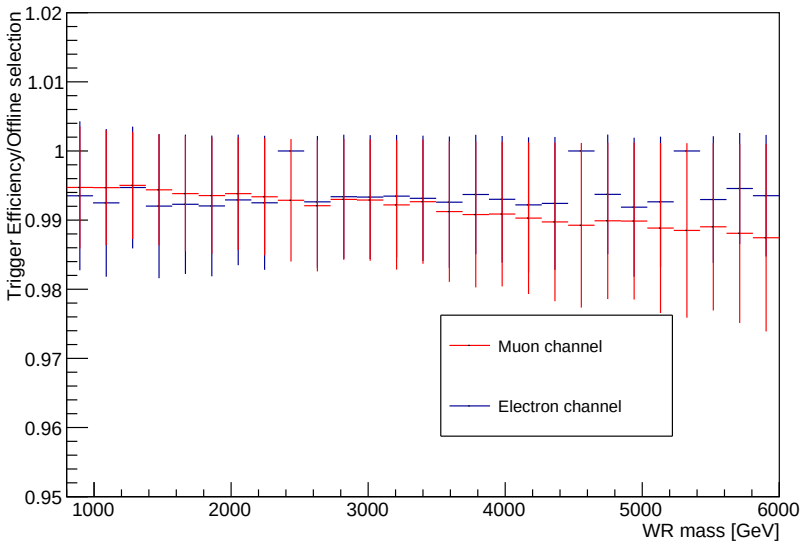

Figure 5.3: Trigger efficiencies for signal of the muon and electron triggers with respect to offline selection as a function of the W_R mass.

5.2.2 Offline selection

To properly reconstruct our W_R candidates, we select the two most energetic leptons and two jets. The selection criteria for each object are described below.

Muons

- Kinematic cuts: $p_T > 53$ GeV, to be in the efficiency plateau of the trigger, and $|\eta| < 2.4$ to be within the acceptance of the muon system.
- Must pass the HighPtID as described in Section 4.2.
- Muon track must be isolated from other tracks in the event. The sum of p_T from tracks within a cone of radius $\Delta R = 0.3$ must be less than 10% of the muon p_T.

Electrons

- Kinematic cuts: $p_T > 53$ GeV for symmetry with the muon requirements and, $|\eta| < 2.4$ within the ECAL acceptance.
- Must pass HEEP identification as described in Section 4.3.

Jets

- Kinematic cuts: $p_T > 40$ GeV and $|\eta| < 2.4$.
- Must pass tight jet identification as described in Section 4.4.

Sidebands and signal region

We define sidebands to estimate the contributions from the different backgrounds in our signal region. In the low dilepton mass sideband, we require two selected leptons with the same flavor and two selected jets. The invariant mass of the two leptons must be below 200 GeV. This sideband is used to study the Drell-Yan background contribution and to scale the overall normalization of the estimate from simulation.

In the flavor sideband, we require one selected muon, one selected electron, and two selected jets. The invariant mass of the two leptons must be above 200 GeV. This sideband is used to study the $t\bar{t}$ background contribution. This sideband in dominated by $t\bar{t}$ events with smaller contributions (8%) from diboson, tW events, and DY+jets. We estimate the $t\bar{t}$ contribution from this sideband using a data driven method as explained in Section 5.4.

The signal region requires two selected leptons with the same flavor and two selected jets. The invariant mass of the two-lepton combination must be above 200 GeV. The four-object invariant mass must be greater than 600 GeV. In the sidebands and signal region, the lepton with higher p_T must pass an additional cut of 60 GeV.

5.3 Data/simulation comparison

In this Section we compare distributions of interesting variables between the data and simulation in the two sidebands defined above. The agreement in the low dilepton mass sideband is especially important since we derive the estimate for the Drell-Yan background from the simulation. Any disagreement in these comparisons could be a sign of new physics, or some SM process that contributes to the final state that has not been taken into account and must be included. A comparison of the data and simulation is also a diagnostic for detector issues that occurred during the data taking, which could be potentially resolved.

The contributions from the simulation samples listed in Table 5.2 are shown as a stacked histogram in the following plots. The diboson and single top contributions are combined into a single histogram labeled *Other*. Figure 5.4 shows the comparison in the low dilepton sideband for muons and Figure 5.5 shows the electron distributions. These comparisons are a confirmation that our DY+jets background estimate procedure provides a sensible description of the data, with a difference between data and simulation less than 1%. The systematic uncertainties on the normalization of the simulation, lepton and jet energy

measurement, lepton and jet reconstruction, and theoretical variations that were assigned are appropriate to the level that we trust the simulation.

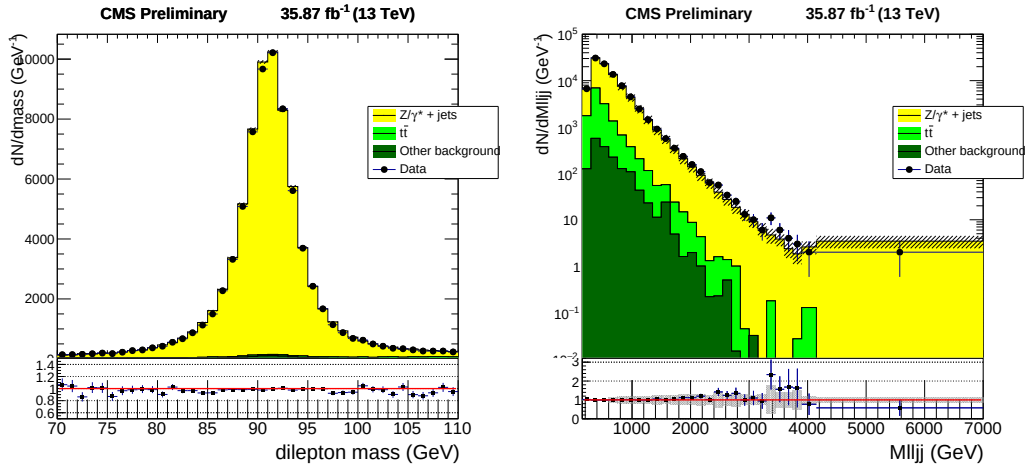

(a) Dilepton mass.

(b) Four-object mass.

(c) Dilepton momentum.

(d) Scalar sum of all jets p_T.

Figure 5.4: Comparison of data and simulation in the muon channel in low dilepton mass sideband.

Figure 5.6 shows the comparison in the flavor sideband. We do not use the simulation to estimate the $t\bar{t}$ background contribution, but the fact that we see such a good agreement is taken as a good sign that the simulation is working as intended. The contributions from other backgrounds is only 8%, so we can treat

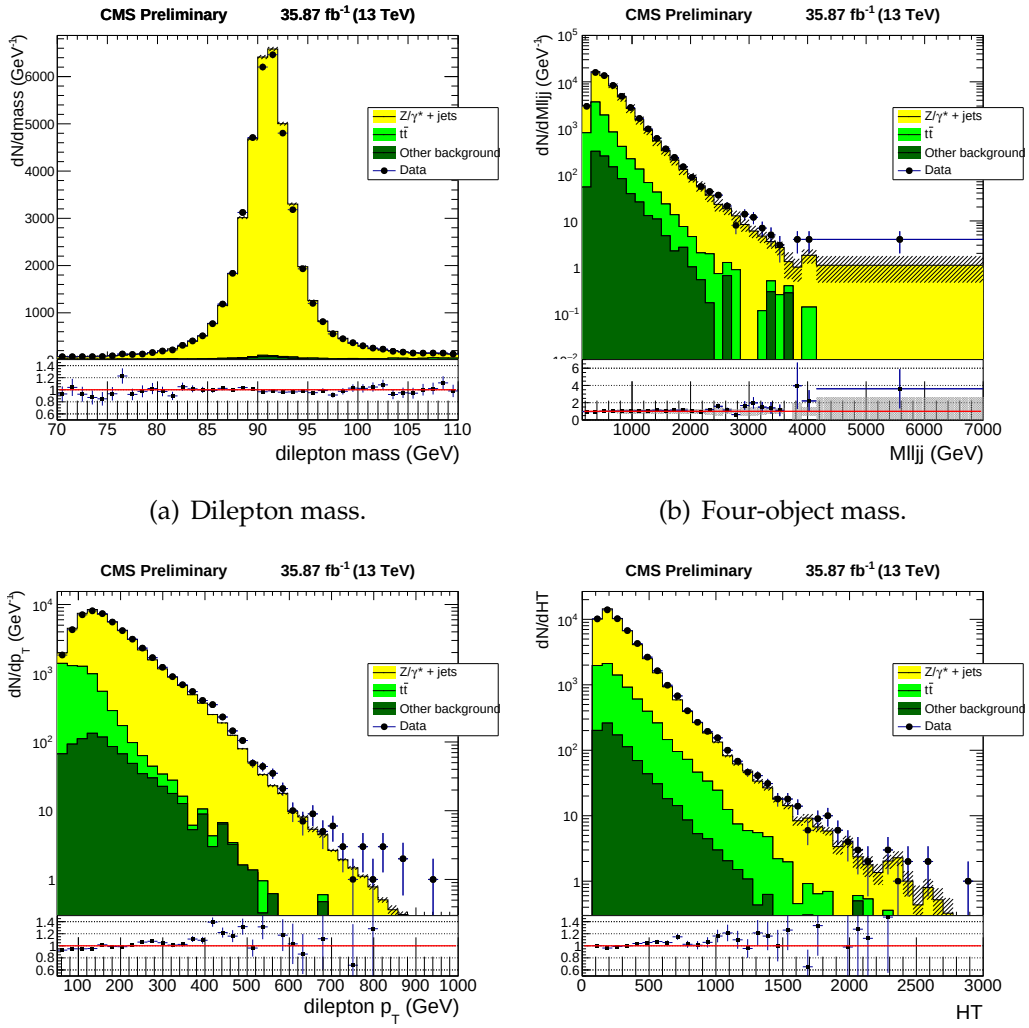

(a) Dilepton mass.

(b) Four-object mass.

(c) Dilepton momentum.

(d) Scalar sum of all jets p_T.

Figure 5.5: Comparison of data and simulation in the electron channel in low dilepton mass sideband.

this sideband as a clean $t\bar{t}$ sample.

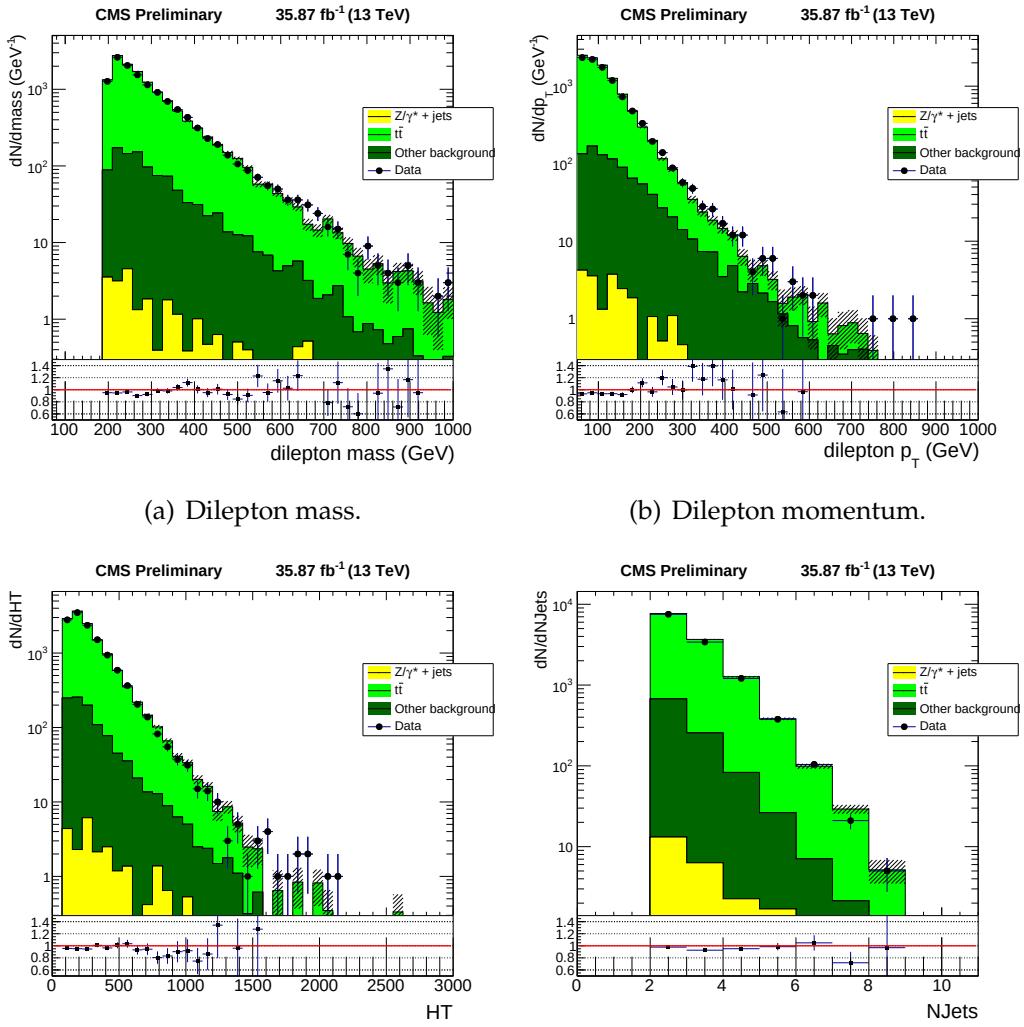

(a) Dilepton mass.

(b) Dilepton momentum.

(c) Scalar sum of all jets p_T.

(d) Number of jets.

Figure 5.6: Flavor sideband comparison between the data and simulation. Contributions from backgrounds other than $t\bar{t}$ is approximately 8%, which makes this sideband a clean sample for the $t\bar{t}$ data driven estimate.

5.4 Background estimation

Standard model processes that produce the same final state particles as our signal model include Drell-Yan production with additional jets from initial state radiation, $t\bar{t}$ production, and diboson events. These backgrounds make up the

bulk of our background estimate. Diboson backgrounds are negligible due to the dilepton mass cut above 200 GeV, away from the Z peak. We also include backgrounds where object mis-identification leads to events with two leptons and two jets in the final state. The contribution from these backgrounds is small due to the low lepton fake rates.

5.4.1 $t\bar{t}$ background

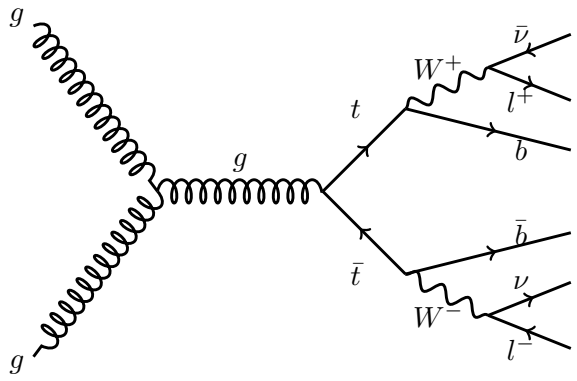

Figure 5.7: Feynman diagram for leading order $t\bar{t}$ production and dileptonic decay.

The leading Feynman diagram for dilepton $t\bar{t}$ production is shown in Figure 5.7. The $t\bar{t}$ background contribution is estimated directly from data in the flavor sideband control region, which has the same kinematics as the $t\bar{t}$ in the signal region (see Section 5.2). To produce a clean $t\bar{t}$ sample, the contribution from other standard model processes is estimated from simulation and subtracted in the flavor sideband. In Figure 5.8 the M_{lljj} distribution is shown for data and simulation in the flavor sideband.

For this estimate, the assumption made on the conservation of the flavor in the decay is needed to ensure that there is no contamination from signal events.

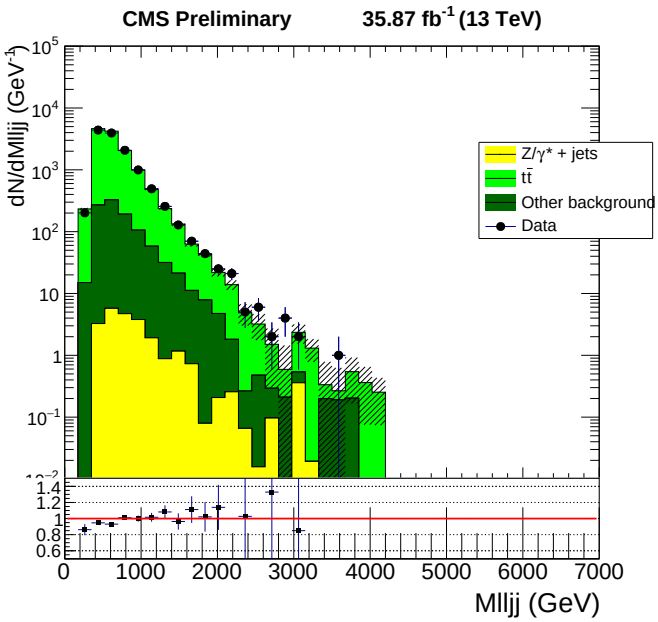

Figure 5.8: M_{lljj} distribution for data and simulated events in the flavor sideband with all scale factors applied.

We assume the decay of a real W_R boson at leading order cannot yield an $e\mu jj$ final state and we can use these events to estimate the background in our signal region.

Table 5.3: Scale factor applied to the number of events in flavor sideband to estimate the number of $t\bar{t}$ events in the $eejj$ and $\mu\mu jj$ signal regions.

channel	Scale factor
$e\mu jj \rightarrow eejj$	$0.418 \pm 0.002(\text{stat.}) \pm 0.067(\text{syst.})$
$e\mu jj \rightarrow \mu\mu jj$	$0.690 \pm 0.003(\text{stat.}) \pm 0.139(\text{syst.})$

To calculate the number of events from $t\bar{t}$ in the $eejj$ and the $\mu\mu jj$ signal-regions we use the $t\bar{t}$ simulation to find the scale factor $R_{e\mu,ee/\mu\mu}$ between events with $e\mu jj$ in the final state and events with same-flavor leptons in the final state. These scale factors are evaluated from the ratio of the number of events in the

$M_{e\mu jj}$, M_{eejj} and $M_{\mu\mu jj}$ distributions with $M_{lljj} > 600$ GeV. The number of events in the signal region is given by

$$N_{\text{ttbar}}(\text{signal}) = N_{\text{ttbar}}(\text{flavor}) * R_{e\mu,ee/\mu\mu} * R_{\text{trigger}}, \tag{5.1}$$

where $R_{\text{trigger}} = 2 - \epsilon_\mu$ is to correct for the trigger efficiency in single muon events with respect to double muon events.

Using these scale factors, we can account for the difference in efficiency and acceptance between electrons and muons in the corresponding final states. The values of the scale factors obtained are given in Table 5.3. The ratios as a function of M_{lljj} are shown in Figure 5.9. We assign a systematic uncertainty to the scale factors by fitting different envelope functions that cover the spread in the scale factor values.

Figure 5.9: Bin-by-bin ratio of the M_{lljj} and $M_{e\mu jj}$ distributions from $t\bar{t}$ simulations, for electrons (Left) and muons (Right). The χ^2 is calculated with respect to the linear fit.

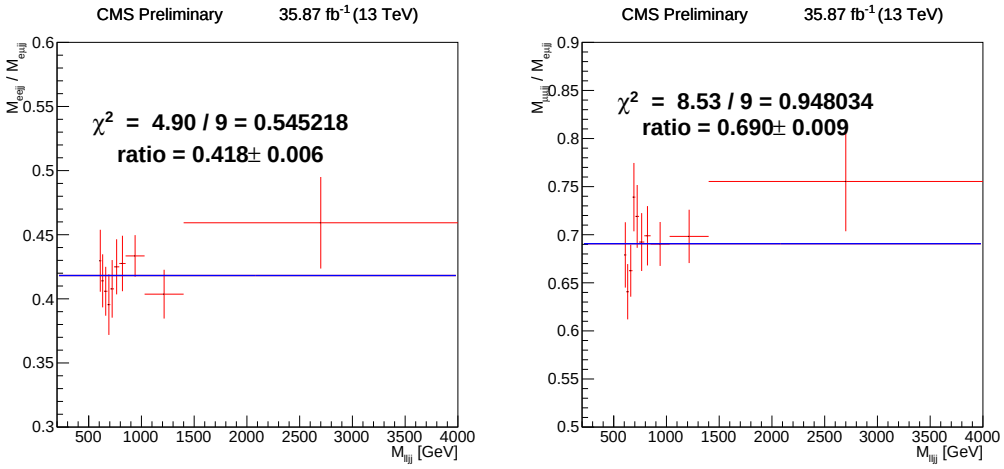

5.4.2 Drell-Yan background

Monte Carlo simulation is used to estimate the background from high mass Drell-Yan lepton pairs produced in association with additional jets, since no high purity control region has been identified having the same kinematics as the signal region. The Drell-Yan plus jets sample is normalized to the measured integrated luminosity and the scale factor for lepton efficiencies discussed in Section 4 are applied.

The Drell-Yan sample is reweighted to account for electroweak next-to-leading-order corrections calculated by the CMS monojet analysis [72]. These corrections have been derived using Z + 1-jet events as described in [73], where we can see that the changes as a function of jets multiplicity are small so they can also be applied to Z + 2-jet events. These electroweak effects tend to reduce the cross-section estimate with increasing transverse momentum of the original generated Z boson and are of the order of 1% at 150 GeV and 15 – 20% at 1 TeV.

The normalization of the Drell-Yan contribution in the simulation is corrected to match the events in data by a scale factor measured in the low M_{ll} sideband, counting the events with $80 < M_{ll} < 100$ GeV (events under the Z peak). This scale factor takes into account residual mis-modelling between data and simulation, including the requirements on the jets, luminosity, sample cross section, etc.

In Table 5.4, we present the scale factors that are used in the estimate of the Drell-Yan contribution in this analysis.

Table 5.4: Scale factors calculated in Drell-Yan low dilepton mass sideband used to normalize simulated events to data.

channel	Scale factor
$Z \to e^+e^-$ (AMC@NLO)	1.08 ± 0.01(stat.)
$Z \to \mu^+\mu^-$ (AMC@NLO)	1.08 ± 0.01(stat.)

5.5 Statistical treatment and limit setting procedure

The signals considered in this analysis are characterized by invariant mass distributions that extend over several hundred GeV. No further assumptions are made on the signal shape. A cut-and-count approach is effective in analyzing the data without exploiting further characteristics of the signal model used as benchmark and to reduce the effect of uncertainties on the shapes of the backgrounds, especially in the high M_{lljj} region. The expected number of signal and background events is estimated by counting the events falling in the specified M_{lljj} range.

The probability of the observed number of events being produced by a combination of background and signal with a cross section is calculated using a Bayesian approach with flat prior. The exclusion limit on the cross section is set such that the above mentioned probability is <5%. This is repeated for each mass hypothesis.

In order to take into account the uncertainties, pseudo-experiments are performed varying the expected number of events from signal and background according to the uncertainties as described in the following section. The median of the distribution of the excluded cross section produced by pseudo-experiments and the intervals containing 68% and 95% of the pseudo-experiments are then

quoted in the expected limits.

5.5.1 Uncertainties

Two categories of systematic uncertainties are taken into account when evaluating the limits of this search. The first category, *category A*, are those systematic effects that do not change the shape of the four-object mass distribution. These are multiplicative factors that relate to the overall event scale, such as the normalization uncertainties on $t\bar{t}$ and Drell-Yan. The second category, *category B*, refers to the systematic effects of object reconstruction. These systematics include the scale and resolution uncertainties of leptons and jets. The systematics sources considered in this analysis are:

- Background normalization (category A).

  The uncertainty on the Z/γ^*+Jets normalization scale factors, and $t\bar{t}$ $ee/e\mu$ and $\mu\mu/e\mu$ scale factors are described above.

- PDF, factorization, and renormalization (category A).

  Implemented following the PDF4LHC prescription [74].

- Luminosity (category A).

  As officially provided by the CMS Luminosity POG [75].

- Jet energy scale and resolution (category B).

  The jet energy correction uncertainties are taken from the official CMS Jet/MET group recommendations [76]. Each of the corrections applied to the data and simulation have certain systematic uncertainties, such as uncertainty in the ISR+FSR corrections, the non-Gaussian tails of the energy

measurements, and the pileup conditions among others. These uncertainties are provided to physics analyses as systematics sources that include the correlations in p_T and η.

- Muon energy scale and resolution (category B).

  Muon scale and resolution uncertainties are taken from the Rochester correction package recommended by the CMS Muon POG. These small corrections are applied to the data and the simulation to correct for the remaining detector misalignment using the Z peak as a standard candle. The residual differences between the data and simulation are taken as the systematic uncertainty of the method.

- Muon reconstruction and identification SF (category B).

  p_T dependent uncertainties are taken according to the Muon POG recipes. Uncertainties in the muon reconstruction and identification are derived using a tag-and-probe method in $Z \rightarrow \mu\mu$ events. One of the muons (the tag) is required to pass tight selection requirements, while the second muon (the probe) has looser requirements. The uncertainty in the efficiency to reconstruct and identify these muons is taken as a systematic.

- Electron energy scale and resolution (category B).

  Electron scale and resolution uncertainties are taken from the CMS EGamma group recommendations [77, 78]. Residual differences in the electron energy scale between data and simulation are taken as systematic uncertainties. Energy resolution in simulation is matched to the data by a fitted Gaussian smearing and the uncertainties and correlations from the fit are taken as the systematic uncertainty.

- Electron reconstruction, identification SF (category B).

  SF and related uncertainties are discussed in Section 4.3. A tag-and-probe

procedure is used to measure the reconstruction and identification efficiency for electrons in $Z \rightarrow ee$ events. The uncertainties in the tag-and-probe are taken as systematic uncertainties.

We summarize the *category A* uncertainties in Table 5.5. These are implemented in the statistical treatment as nuisance parameters with log-normal priors. The range in the normalization uncertainty for DY+jets is due to the low statistics at high M_{lljj}. This systematic is applied for each bin in M_{lljj} and added in quadrature when estimating the background counts.

Table 5.5: Uncertainties affecting M_{lljj} normalization only (*category A*).

Uncertainty source	Magnitude (%)
$t\bar{t}$ $ee/e\mu$ SF	15.9 (stat+syst)
$t\bar{t}$ $\mu\mu/e\mu$ SF	20.1 (stat+syst)
DY+jets ee PDF	15 – 70 (syst)
DY+jets ee renormalization/factorization	5 – 40 (syst)
DY+jets $\mu\mu$ PDF	10 – 70 (syst)
DY+jets $\mu\mu$ renormalization/factorization	10 – 50 (syst)
Luminosity	2.5 (stat+syst)

In order to propagate *category B* uncertainties, a large number of pseudo-experiments is performed, varying all the nuisance parameters in an uncorrelated way, each of them according to a Gaussian distribution with mean equal to the nominal value and σ equal to the uncertainty of the single source. The variations are done before the event selection, so each pseudo-experiment undergoes the full analysis chain. The expected number of events for signal and background used to extract the limits are given by the means of the pseudo-

experiment distributions, and their standard deviations are taken as the propagated uncertainty.

We present the expected number of events in Table 5.6 for a few W_R mass points. The statistical and systematic uncertainties are presented and we can see that both of these are of comparable size. At higher W_R masses, the statistical uncertainty tends to dominate over systematic effects.

Table 5.6: Magnitudes of systematic and statistical uncertainties in different W_R mass windows. All uncertainties are in number of events.

	Electron channel				
M_{W_R} (GeV)	Signal (mean ± stat ± syst)	Z/γ^* (mean ± stat ± syst)	Top quark (mean ± stat ± syst)	Other (mean ± stat ± syst)	All BG (mean ± stat ± syst)
2200	475.0 ± 3.7 ± 44.5	15.9 ± 1.74 ± 3.04	23.09 ± 3.1 ± 3.12	7.52 ± 1.38 ± 1.93	46.51 ± 3.81 ± 4.76
2800	114.3 ± 0.89 ± 10.57	4.17 ± 0.84 ± 0.79	5.71 ± 1.54 ± 0.86	3.43 ± 0.89 ± 0.67	13.31 ± 1.97 ± 1.34
3800	12.9 ± 0.1 ± 1.18	0.96 ± 0.24 ± 0.23	0.42 ± 0.42 ± 0.04	0.0 ± 0.0 ± 0.0	1.38 ± 0.48 ± 0.23
	Muon channel				
M_{W_R} (GeV)	Signal (mean ± stat ± syst)	Z/γ^* (mean ± stat ± syst)	Top quark (mean ± stat ± syst)	Other (mean ± stat ± syst)	All BG (mean ± stat ± syst)
2200	743.0 ± 4.7 ± 49.0	35.23 ± 2.49 ± 4.93	38.32 ± 5.14 ± 6.59	10.22 ± 1.55 ± 1.09	83.77 ± 5.92 ± 8.3
2800	176.7 ± 1.13 ± 13.58	8.39 ± 1.1 ± 1.3	9.48 ± 2.55 ± 1.74	2.31 ± 0.73 ± 0.19	20.18 ± 2.88 ± 2.18
3800	18.6 ± 0.13 ± 1.91	1.07 ± 0.38 ± 0.22	0.69 ± 0.69 ± 0.1	0.21 ± 0.21 ± 0.01	1.98 ± 0.82 ± 0.24

5.6 Results

The selected events in the signal region are shown in Figure 5.10. There is an event in the tail for the muons, where the prediction is zero events. In fact, due to the fact that we are using a `AMC@NLO` sample, the expected number of events in this bin is negative. This is physically impossible and it shows that we did not produce enough simulated events to represent this region of phase space. This excess translate into slightly worse limits at the highest W_R masses, but it is still consistent with the SM prediction within 1 σ.

The 95% confidence level expected upper limits on the W_R signal cross sec-

Figure 5.10: Selected events in the signal region. (Left) Electrons, (Right) Muons.

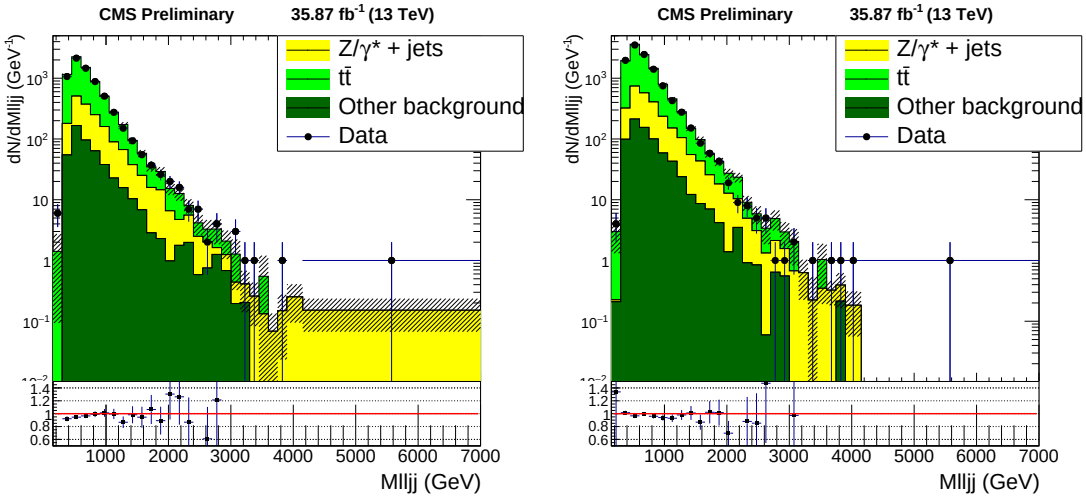

tion are shown in Figure 5.11 taking into account all the systematic and statistical uncertainties. The exclusion limit is 4.4(4.4) TeV for muons (electrons). In Figure 5.12, we also present the exclusion limits in the 2-dimensional plane of W_R vs. N_R masses. The region where $M_{N_R} \ll M_{W_R}$ cannot be excluded is due to the low efficiency to select these events with the criteria described above.

Figure 5.11: Limit on $\sigma(pp \rightarrow W_R) \times BR(W_R \rightarrow lljj)$ with expected limit bands.(Left) Electrons, (Right) Muons.

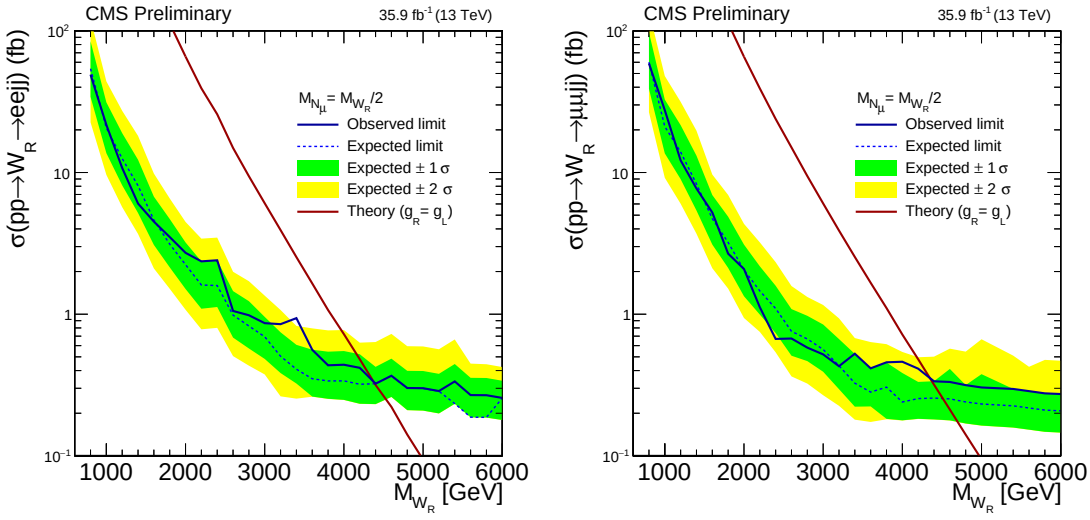

Figure 5.12: Upper limit on the plane of cross sections for W_R and N_R mass hypotheses. Expected exclusion $\sigma(pp \rightarrow W_R) \times BR(W_R \rightarrow lljj)$ cross section limit. (Left) Electrons, (Right) Muons.

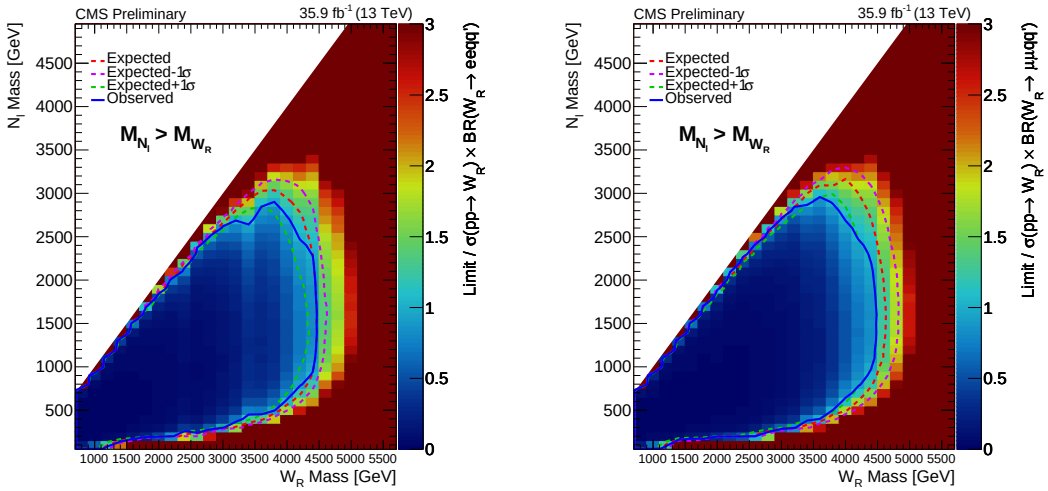

CHAPTER 6

CONCLUSION

We presented a search for a right-handed W boson in the context of a Left-Right symmetry model using the data collected by the CMS detector at 13 TeV center-of-mass energy. We used the 35.9 fb^{-1} of proton-proton collision data collected in 2016.

The initial increase in energy for Run 2 provided a large boost in production cross section for our W_R signal. As the CMS detector begins a period of stable data collection, we established a framework that allowed the search for W_R bosons to be easily repeated from 2015 to 2016 and possibly in years to come.

The W_R decays to two high p_T jets and two same flavor leptons, so its mass can be reconstructed from these objects. Therefore, we performed a bump-hunt in the four-object mass distribution looking for a wide resonance. Standard model backgrounds were estimated with a combination of data-driven techniques, as well as taken directly from the simulation.

We do not see an excess of events near a four-object mass of 2 TeV, as was seen in Run 1, effectively ruling out a possible W_R signal. We present the 95% confidence level upper limits on the W_R production cross section as a function of the W_R mass and the heavy neutrino mass. We exclude a W_R boson with masses below 4.4(4.4) TeV for muons (electrons) in the context of a Left-Right symmetry model.

APPENDIX A

PROPOSED SYSTEM FOR L1 TRACKING AT CMS

In this Appendix we present a system to perform tracking at the hardware level of triggering for the Phase 2 upgrade of CMS [79]. This proposed system is expected to be in place for the high luminosity running era of the LHC [56] (HL-LHC) starting in 2026.

The LHC is expected to deliver 300 fb^{-1} of data before the HL-LHC upgrade and 3000 fb^{-1} by the end of its lifetime. In order to achieve this in a reasonable amount of time, the beam intensity must increase considerably. During the Run 2 period, the average number of proton-proton interaction per bunch crossing was approximately 20. In the HL-LHC this number is expected to be 200 or more interactions per bunch crossing. The CMS and ATLAS detectors were not initially designed to operate under these conditions and must be upgraded to continue efficiently collecting data.

The goal of CMS for the HL-LHC is to continue to provide high quality data as in Runs 1 and 2, which led to the discovery of the Higgs boson. With this high-quality data, we hope to study the Higgs in great detail and even perhaps discover physics beyond the standard model. But we only want to keep those events where interesting physics could be happening and discard the rest. Therefore, a highly selective trigger system is necessary. A description of the current trigger in CMS was presented in Chapter 3.

A.1 CMS upgrade

By the time of the Long Shutdown 3 (LS3) of the LHC in 2023, the silicon tracker and endcap calorimeters of CMS will be severely damaged by radiation and will be replaced. Detectors in the forward region ($\eta > 3$) will be installed to help mitigate the effects of pileup. The trigger system will be redesigned to cope with the much higher instantaneous luminosity. In this environment, increasing the thresholds does not reduce the trigger rates. The flattening of the rate as a function of the threshold can be seen for a muon trigger in Figure A.1. In the current trigger system, the way to reduce trigger rates was to simply increase the p_T thresholds at the cost of losing events with possibly interesting physics. To keep a rate below 10 kHz for a muon trigger, the p_T requirements are expected to be greater than 30 GeV for muons in the barrel region, while this rate is not even possible for muons in the endcaps. These thresholds are prohibitively high for many analyses that rely on muons, including the W_R search presented in this dissertation.

To recover the discriminating power of the trigger, tracking information must be included at the hardware level. Since a new tracker is going to be built, this offers an opportunity to redesign the CMS tracker as a combined track-trigger system. A description of the proposed tracker was prepared for the Phase 2 Technical Proposal (TP) of CMS [79]. The most relevant feature for tracking is that the layers are constructed from dual sensor modules, which provide a position of the hits and an initial measurement of the momentum of tracks. Two correlated energy deposits in a module are called a stub. With the initial momentum measurement, it is possible to discriminate low momentum stubs (less than 2-3 GeV) and reduce the read-out rate from the front end

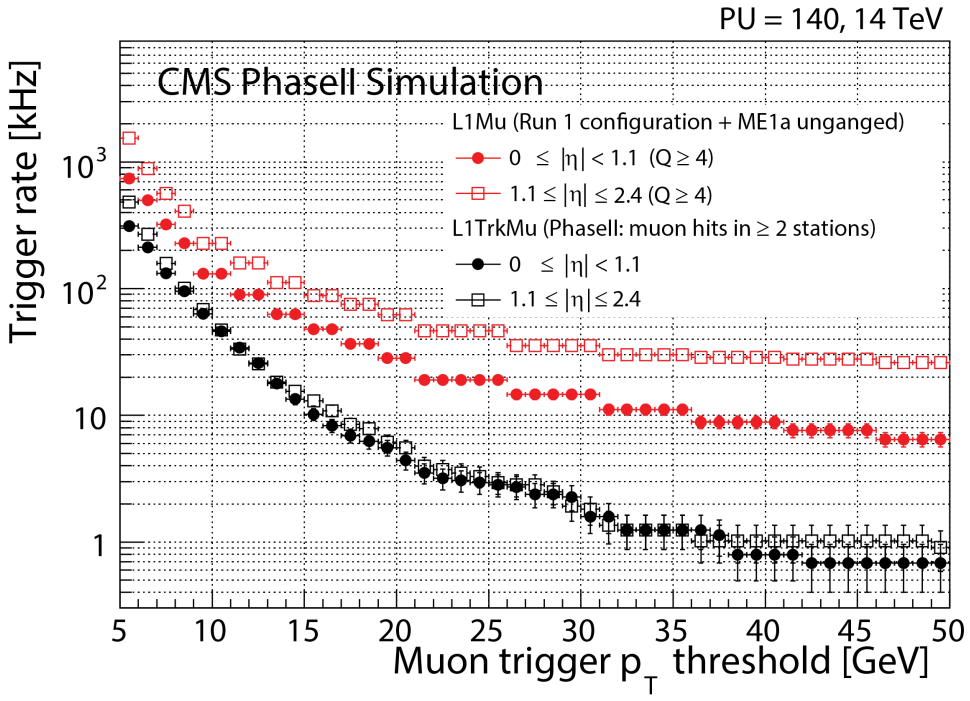

Figure A.1: Expected L1 rates for muon triggers at the HL-LHC [79] as a function of the p_T threshold. Two possible scenarios are presented for triggers with and without the tracking information at the hardware level. It is clear that the rate for a trigger without tracking information cannot be reduced by increasing the threshold.

electronics. The high momentum stubs will then be used to reconstruct tracks, which in turn will be combined with information from the muon system and calorimeters to form higher level physics objects.

The tracker geometry that was used for the TP is shown in Figure A.2. This geometry was also used to develop the tracking algorithm presented in this Appendix. To reduce the material budget of the tracker and to improve read out efficiency from the sensors, a new geometry was proposed known as the *tilted barrel* geometry. As its name suggests, in this new geometry the inner three layers are tilted such that they face normal to the interaction point in the $r - z$ plane. Some work is needed to adapt our tracking algorithm to this new

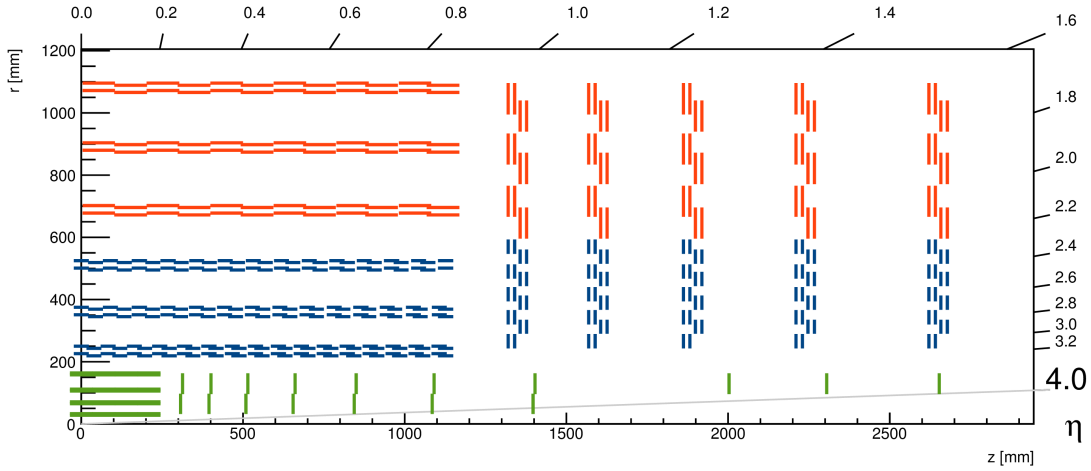

Figure A.2: One quarter of the flat barrel CMS tracker for Phase 2 [79].

geometry but the core concepts are still valid. The schematic of the tilted barrel tracker geometry is shown in Figure A.3.

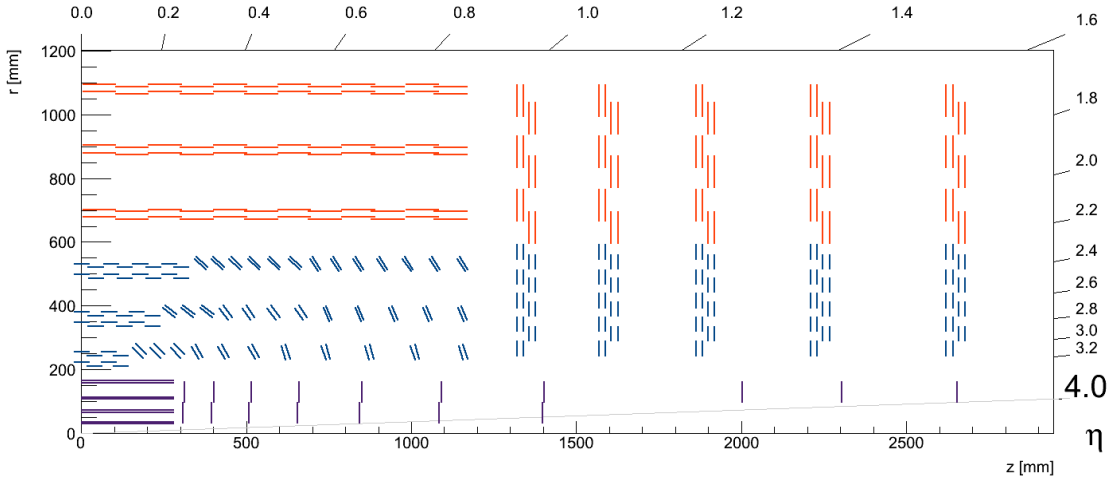

Figure A.3: Possible configuration of one quarter of the tilted barrel CMS tracker for Phase 2. The tilted geometry is still under study and optimization changes are still ongoing with the input from physics as well as engineering design.

A.2 Tracklet algorithm

The trigger requirements impose latency, reconstruction efficiency, and parameter resolution constraints on any algorithm that can be used for tracking. At a collision rate of 40 MHz, a new event is produced every 25 ns and a trigger decision must be made in under 12.5 μs. This budget includes all the time it takes for data to move from the front end of the detector to the tracking hardware and then downstream to be combined with the other subsystems. This takes up the majority of the available time: the time allotted for tracking is under 4 μs.

The algorithm must also produce well reconstructed tracks for a specified resolution on the track parameters. It is most crucial to be able to discriminate low momentum tracks for triggering, as these are mainly associated with non-interesting events. It is also important to resolve the track position along the z-axis to filter those coming from pileup interactions. Given that the algorithm must run on hardware, there is a trade-off between the precision in estimating the track parameters and the resources available on the hardware. Thus, our algorithm was tuned to provide the required parameter precision that is good enough for triggering.

We have developed a tracking algorithm that meets these requirements using Field Programmable Gate Arrays (FPGA). Our algorithm is a basic road-search algorithm not much different from those used in offline tracking. We construct a track seed (tracklet) using stubs in two adjacent layers and the interaction point. With these three points in space, we can estimate the parameters of the track helix. We use the full precision of the stub information for this initial estimate, which gives us already accurate parameters. Figure A.4 shows the

resolution of the tracklet parameters with respect to the MC truth information. The resolution on the tracklet parameters is sufficient to discard tracks that have low momentum or do not appear to be coming from the interaction point. This reduces the number of fake tracks that need to be processed further in the algorithm. The tracklet is then projected to the other layers where we look for

Figure A.4: Comparison of the tracklet parameter resolution between the floating point implementation and the reduced-precision integer implementation of the tracklet algorithm. Since the full precision of the hit position is used to calculate the tracklet parameters, the resulting parameters are already close to the MC true values. This allows to select only those tracklets that are most likely to form valid tracks without spending resources on fake combinations.

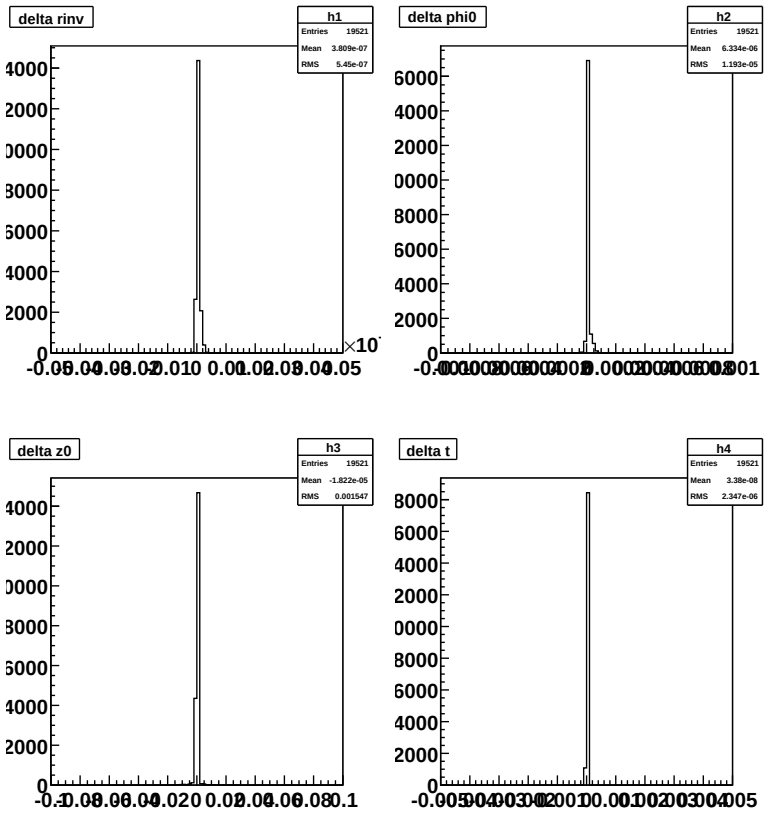

matching stubs. We form tracklets from multiple pairs of layers to increase our track finding efficiency. For a tracklet formed in the inner two layers, we project

from the inside out, while for a tracklet formed in the outer layers we project outside in. In every projected layer, we calculate the difference between the expected track position and the true position of the stubs. If a stub is found within a window around the expected track position we store the residual difference.

The residuals from matched stubs are then used in a final refit of the track parameters. We perform a linearized χ^2 fit for the final track parameters. This simplified fit can be done using precomputed derivatives stored in lookup tables, which makes it ideal for a hardware implementation. Since we form tracklet seeds in multiple layer pairs, we must remove duplicated tracks before sending them downstream. We flag a track as a duplicate if it shares more than four hits with another track. The efficiency to find tracks using different seeding combinations of layers is shown in Figure A.5. We can see that the different combinations of seeding layers provide coverage in different η regions of the detector, leading to almost full efficiency across the detector. There is overlap between the seeding layers, which provides some redundancy at the cost of duplicated tracks.

The algorithm was implemented in C++ using floating point precision for the calculations and it was integrated into the CMSSW software package for studies by the physics groups. We also developed another version of the algorithm in C++ using reduced precision and integer calculations to emulate what could be achieved in hardware. This reduced precision in the calculations barely affects the parameter resolution, as seen in Figure A.6.

The tracklet algorithm was developed with a fixed latency model, where the time it takes for each of the steps described above is constant. The drawback of this approach is that at some point, the processing of an event must be truncated

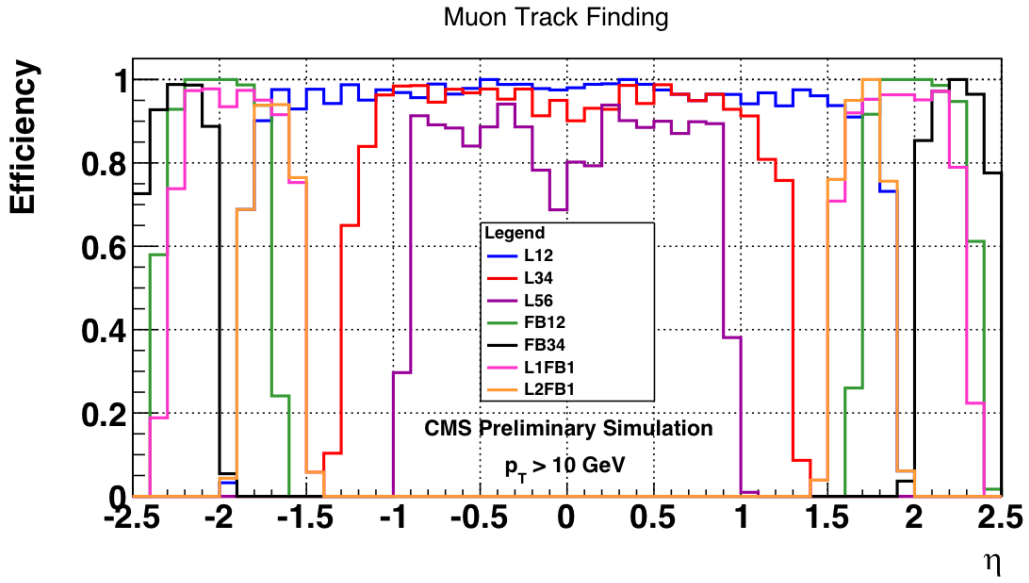

Figure A.5: Efficiency to find single muon tracks depending on the seeding layers used to form the tracklet. There is almost full efficiency across the entire η range provided by the different seeding layer combination. The overlap region produced duplicate tracks that must be removed in the final step of the algorithm.

if it takes longer than the allotted time. Events where this truncation occurs are rare and thus the drop in efficiency is not a major effect. This was studied in the C++ emulation of the algorithm and possible improvements in the data partioning were developed to mitigate loses due to truncation.

The main challenge for an implementation of tracking at 40 MHz is not the track parameter calculation, as the calculations involved are straightforward, but instead the challenge is to manage the enormous amount of data coming off the detector and move it efficiently to where it needs to be. The tracklet approach to this difficult problem is to partition the data in such a way that the available resources (both time and hardware) are used optimally. By using an FPGA, we can massively parallelize the calculations while simultaneously

Figure A.6: Comparison of the track parameter resolution between the floating point implementation and the reduced-precision integer implementation of the tracklet algorithm. There is a very small loss in resolution when using fewer bits while still meeting the resolution requirements from the trigger. (Top) Barrel. (Bottom) Forward region.

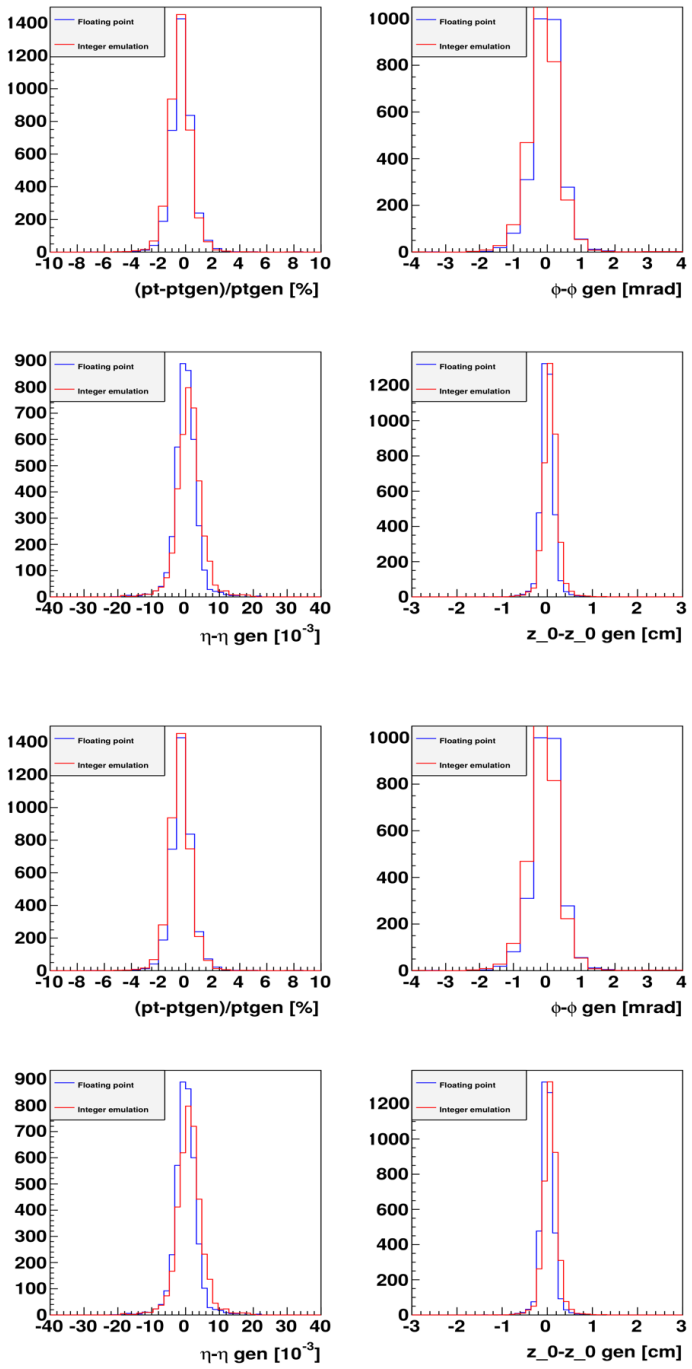

routing the data in and out of memories for optimal processing.

A.3 Data partitioning

The front end sensors in the Phase 2 tracker can send the data out from the detector at 40 MHz for tracks above 2 GeV. For a pileup scenario of 140 interactions per bunch crossing, in a minimum-bias event 97% of tracks have momentum less than 2 GeV. For our tracklet algorithm, we will only consider those tracks above 2 GeV. The algorithm will process this reduced set of tracks so that only a fraction of the hits in the detectors are used to form tracks, greatly reducing combinatorics.

To further reduce the number of possible pair combinations to try while forming tracklet seeds, we divide the detector into 28 ϕ sectors as seen in Figure A.7. Each of these sectors covers the full η range. We chose 28 sectors as it is the largest number for which a 2 GeV track can span at most 2 sectors. A single board with a dedicated FPGA will handle the processing for one of these sectors. Our sector definition for the final system will depend on factors such as the available cabling from the front end and the FPGA resources available. A more powerful FPGA than in the prototype system would allow us to divide the detector into fewer sectors.

The average occupancy in a minimum-bias event for a given sector in the innermost layer at a pileup of 140 is 60 stubs, while in the second layer there are on average 50 stubs. If we were to try all the possible combinations of stub pairs, we would form 300 tracklets, when the true number of real tracks is closer to 30. To further cut down on these fake track combinations, we subdivide each

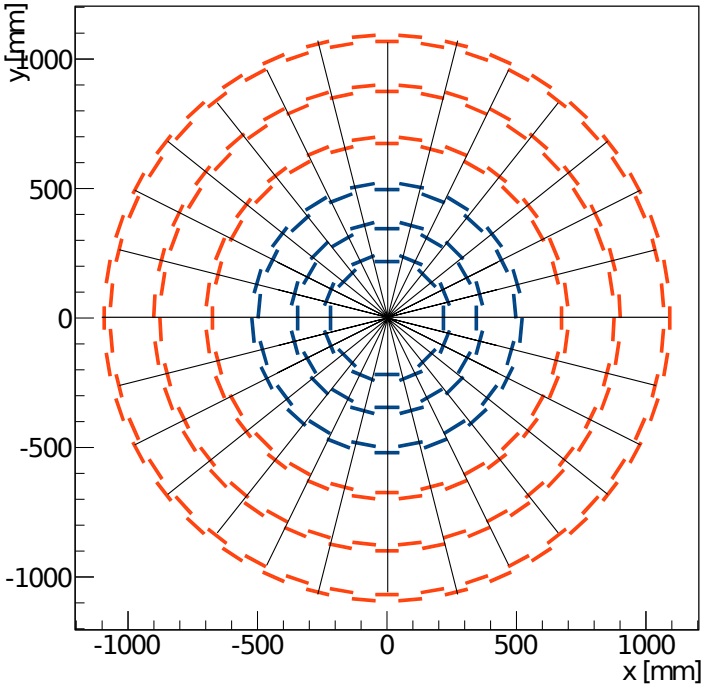

Figure A.7: The $x - y$ view of the CMS Phase 2 tracker with 28 ϕ-sector divisions. This division is implemented to reduce the combinatorics in the seeding of tracks. A 2 GeV track spans at most two of these sectors while bending due to the magnetic field, so there is only neighbor-neighbor communication while forming tracks.

of our sectors into Virtual Modules (VM).

We divide the barrel along the z-axis into 4 regions and the endcaps along r into 4 regions. In the $r - \phi$ plane, we divide odd (even) layers into 3 (4) regions. A schematic of the VMs is shown in Figure A.8(a). For a track with momentum greater than 2 GeV, a stub in a VM in layer 1 will only make valid tracklets with stubs in certain VMs in layer 2. An example of the valid combination of VMs is shown in Figure A.8(b). The total number of VM combinations is 768 pairs, but the only combinations that can form tracks with $p_T > 2$ GeV and point

back to the interaction point is just 96 pairs. The VM concept is at the core of the tracklet approach and this impressive reduction in combinatorics is one of the reasons that made it possible to demonstrate its feasibility as a track-trigger system. Other VM configurations are under study that can distribute the load more optimally in cases where many stubs are clustered in a relatively small area, as in the case of a hadronic jet.

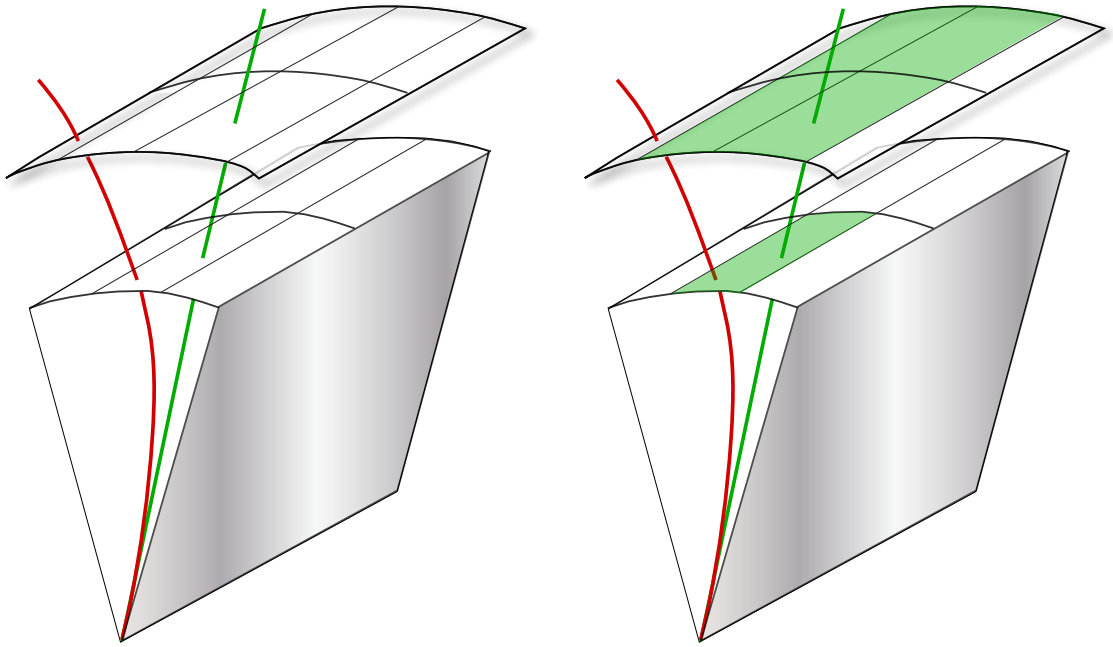

(a) Schematic of VM between L1 and L2.

(b) Valid VM combinations.

Figure A.8: Schematic for virtual modules in half of the barrel for a single ϕ sector. The VM are shown for layers 1 and 2 with 3 divisions in the ϕ direction in the inner layer and 4 divisions in the second layer. Only certain combinations of VM pairs can form valid tracks, which reduces the number from all 768 to 96 valid combinations.

An additional handle available for our algorithm is that events are uncorrelated and can be processed by independent sets of additional hardware with a round-robin scheduling scheme. At the cost of more hardware, we can replicate

our system by a fixed factor and effectively allow for longer processing times for each event. With our tracklet algorithm, we determined that a factor of 6 was a reasonable compromise between the expected system size and the time needed to process the busiest events. Each copy of the system will then receive a new event every 150 ns instead of 25 ns.

A.4 Firmware implementation

The C++ integer emulation of the tracklet algorithm was the basis for the firmware implementation as it most closely resembled the calculations that could be done in hardware. We structured the firmware in a modular way such that many tracks can be processed in parallel [80]. A diagram of the firmware structure is shown in Figure A.9.

In the tracklet diagram, we represent memory blocks in blue and processing modules in red. Data flows from the bottom to the top as it moves from an input memory into a processing module and then into an output memory. Some processing modules receive inputs from more than one memory and can also write to multiple outputs, as seen by the connections in the diagram. The modules along the same row are identical pieces of firmware code, whose only differences are determined by configuration parameters at the time of implementation.

The tracklet diagram in Figure A.9 only includes the modules and memories for a reduced version of the full project. Only the barrel layers are considered and a single copy of identical memories is shown. This is done for illustration purposes, as the full diagram is much more complicated. The source for the

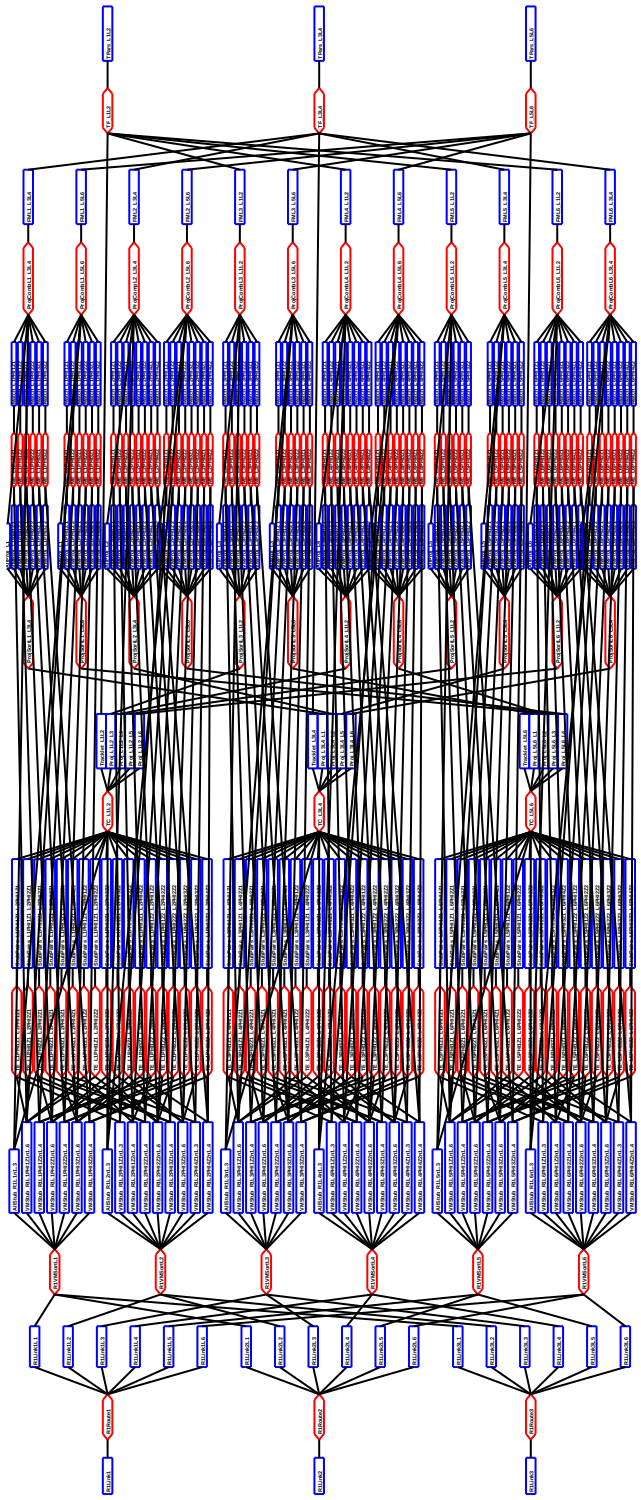

Figure A.9: Tracklet diagram showing processing modules in red and memories in blue with data flowing from the bottom up. This diagram illustrates the different levels of parallelization used in the tracklet algorithm, where many modules in a row imply high levels of parallelism.

tracklet diagram is a master configuration file with all possible connections and every instantiation of the modules. We use this master configuration file to automatically generate the top level code of the firmware, where all the modules are instantiated and their corresponding parameters are set. In C++ we also use the master configuration file to fully emulate the behavior of the firmware. This allows for direct comparisons at every stage of the processing for any memory and any calculation.

As mentioned above, the top level code of firmware is automatically generated with all the necessary instantiations of specific modules for a given task. All the modules performing the same task are identical, but can be configured with different input parameters, thus there are only a handful of unique firmware modules that are replicated many times. These firmware modules were developed using Verilog/VHDL and were carefully validated and optimized. The modules are configured using Verilog parameter statements for the different use cases, such as a layer's radial position or number of bits used to store a given parameter.

Another advantage of using a master configuration file was that it allowed us to develop and test the algorithm in smaller regions before going to the full-size sector. Initially, we developed the core steps using only a single seeding pair in the positive side of the barrel. We then followed a single track as it moved through the algorithm until it reached the final step. Once we were confident that the calculations were correctly implemented, we added the rest of the modules and tested them with more complicated events. The development of the firmware for the endcap modules was done in parallel with many of the modules shared with the barrel firmware.

The algorithm is a pipelined design with a fixed latency determined by the replication factor. An event starts to be processed at the beginning of the pipeline and after 150 ns it moves to the next step in the chain. At this time, a new event is received at the input, which starts to be processed in the first stage. This happens for all events, such that at any given time we are processing multiple events in different stages of the pipeline. After the last stage in the pipeline, we have our reconstructed tracks to be sent downstream. Since we know how much time it takes for each stage, we know our total expected latency and can compare with actual measurements. We discuss this further in Section A.5.

In the tracklet algorithm there are two kinds of processing modules: those for data routing and those for calculations. In total, we used 11 processing steps to implement the algorithm. Here is a brief description of each module:

- **Layer router:** The input data from the front end comes from multiple layers per packet. Before we can form our tracklet seeds, we need to separate this data into memories for each layer. A similar module handles the endcaps, where the data is separated by disk rather than layer.
- **VM router:** Within each layer, we bin the data into the VMs to reduce the tracklet combinatorics. We store two copies of each stub, but one of the copies has reduced precision. We call these VM stubs and they serve as input to the next stage, while the full precision stubs are used for the stage after next. Each VM stub stores an index for the full stub, such that it can be retrieved at a later stage.
- **Tracklet engine:** The tracklet engines use VM stubs from adjacent layers to determine if a tracklet seed is valid. There are many engines that process all possible VM combinations in parallel. Using just a few bits of the stub's

ϕ and z and some lookup tables, we can calculate a very rough estimate of the tracklet momentum and z_0 position. We cut on these so that we only keep tracklet candidates with momentum greater than 2 GeV and that are coming from the origin. If a tracklet candidate passes the cuts, we store the pair of indices to the full precision stubs to be used in the next step.

- **Tracklet calculator:** In this module, we implement the tracklet parameter calculation using the full precision of the stubs. Most of the fake stub pair combinations were eliminated by the tracklet engine and we do not need to spend time trying these fake combinations. The integer calculations are outlined in a whitepaper not yet public [81] and are implemented in the firmware using Data Signal Processing (DSP) slices [82]. The DSP slices are dedicated hardware that can perform very fast addition and multiplications, which makes them ideal for our calculations.

  In this module, we also calculate the projected trajectory of the track into the other layers. A tracklet that was formed in two layers in the barrel can project to the other four layers in the barrel or it can project to the disks. The calculations are slightly different for layers and disks since we store different precisions for the z and r positions of the stubs. A projection can bend enough so that expected position is outside the sector. These projections are flagged to be sent across optical links to the neighbor board.

- **Projection transceiver:** The projections that were flagged in the tracklet calculators to be sent to the neighboring sector are collected in a single module for optical transmission. This module's inputs are projection memories, but most of these memories are empty. Thus, we only need to read those that have something stored in them. To do this efficiently, we use a priority encoder to produce a single data stream with all the pro-

jections headed to the neighboring board. Each board sends and receives projections simultaneously. The incoming projections are demultiplexed and routed to the appropriate layer, where they are recombined with projections that were produced in the local sector board.

- **Projection router:** Similarly as the VM router, the projection router will store two copies of the projections for its output. One of the copies will only store a reduced precision of the projection for a rough matching to VM stubs. The full precision projections are used at a later stage.
- **Match engine:** The goal of the engines is to preselect pairs of projections and stubs that are likely to be matched. Since the matching requires a double loop, it is better to try as few combinations as possible. For every VM stub memory, there is a corresponding match engine that will compare the VM stub position with the VM projection. Again, if the pair passes a window cut, the indices for the full precision stub and projection are passed to the next stage.
- **Match calculator:** The few matches that pass the engine cut are processed by the full precision match calculator. If the stub is close in ϕ and z to the projection, we calculate the residual difference between the two positions. If multiple stubs are matched to the same projection, we only keep the stub with the smallest residual to be added to the track candidate.
- **Match transceiver:** The projections that came from a neighbor sector are flagged. If these projections are found to have a stub matching by the match calculator, the residuals are sent back to the original board that initially produced the projections. A similar priority encoder to the one used for the projection transceiver is used here. Neighbor matches are received in this module as well.

- **Track fit:** With the initial tracklet parameters and the residuals from the other layers, we can perform the linearized χ^2 fit using lookup tables for the derivatives. For tracklets formed from stubs in the disks, the derivative lookup must be done in two stages based on the radial coordinate of the matched stubs. The derivatives obtained from the lookup tables combined with the residuals provide the small corrections to the tracklet parameters needed when including the additional stubs. Only if a tracklet was associated with at least two matched stubs, do we consider the track as valid and send it to the final stage of duplicate removal.
- **Duplicate removal:** Along with the final track parameters, we store indices for the stubs that formed the track. We consider a track to be a duplicate if it shares more than 4 stubs with any other track. The tracks that were formed from an inner layer tracklet have preference in terms of duplicates. Unique tracks are sent downstream to be correlated with other trigger objects.

As mentioned above, the inputs and outputs of processing modules are stored in memories. Some of the outputs are not immediately used by a module and must be stored until the right module needs it. We can allocate a fixed size to the memories since for a given clock speed of our hardware and a fixed latency of the module, we know the maximum number of entries that can go in a memory.

The memories will provide input data to a processing modules for 150 ns, after which the processing module will move on to the data for the next bunch crossing. At the same time, data is being written from the previous module. Thus, we need to implement these as true dual port memories in the FPGA.

Memories that are read immediately after being written are implemented as distributed RAM on hardware. Other memories that need more storage space are implemented as block RAM. With this approach, we can more optimally use the resources available in the FPGA.

A.5 Hardware demonstrator and results

The algorithm was shown to perform well in C++ emulation, but the real test was to implement it in hardware. Since the system will be deployed in 2025-2026, we have to extrapolate a reduced version using current technology to the expected full system. A scaled down demonstrator was built to prove the core concepts of the tracklet algorithm. These results were presented to a committee of experts for evaluation as more than one approach to tracking was available.

The firmware was developed for a Virtex 7 FPGA (XC7VX690T) [83], which is available with the Xilinx VC709 evaluation board, using the proprietary Xilinx development suite Vivado. The evaluation board served as a test bench for development, but it did not have the required transceivers for optical communication. The University of Wisconsin developed a μTCA board (CTP7) [84] for the current trigger of CMS [85], which also used the same Virtex 7 FPGA. We were able to use four of these boards for our demonstrator system. A diagram of the demonstrator is shown in Figure A.10. A central processing board accompanied by its left and right neighbors will run the tracklet algorithm firmware, while a fourth board will serve as the source of input stubs as well as the sink for output tracks.

In addition to the Virtex 7 FPGA, the CTP7 board has a Zynq chip for signal

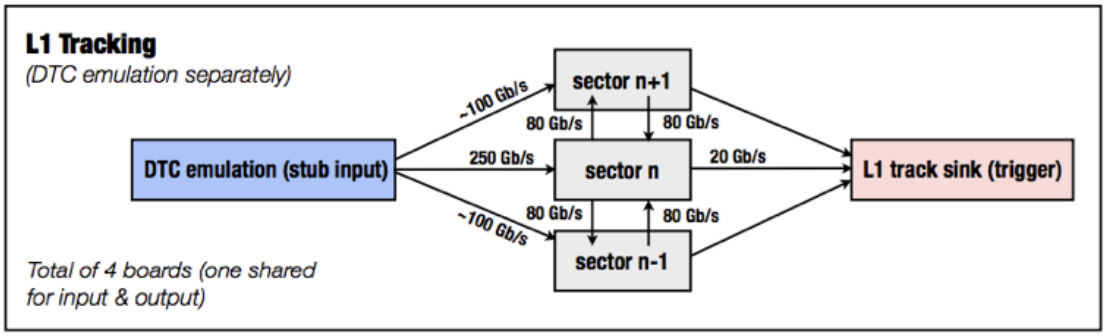

Figure A.10: Diagram of the demonstrator system.

control. The Zynq chip has an ARM core with a light-weight Linux version called PetaLinux, which is coupled with programmable logic for the FPGA side. Memory resources are shared between the two sides and are transparently used on either end. The Zynq is connected to the Virtex 7 FPGA through a Chip2Chip module, which makes the data stored in the Zynq available to the Virtex. We can input data to the board by the Linux side of the Zynq and pass it through to the Virtex for further processing. Given that the Zynq has an assigned IP address, we can send data using an RPC protocol, as well as read data back from the board with the final tracks. A picture of the CTP7 board and the demonstrator crate with the 4 boards is shown in Figure A.11.

The CTP7 board is equipped with three 10 GHz optical transceivers (CXP0-2) with 12 bi-directional bundled links in each of them and a minipod transceiver (MP) with 12 transmitter links and 31 receiving links. The transceivers are configured to run at 240 MHz with at 8b10b encoding protocol [86]. A diagram showing the test stand configuration for communication between the boards is shown in Figure A.12.

The demonstrator system was designed as a proof of concept of the tracklet

(a) CTP7 board. (b) Demonstrator test stand in Vadatech μTCA crate.

Figure A.11: CTP7 board and test stand.

algorithm using current FPGA technology. The final system would take advantage of the fast-advancing developments in FPGAs driven by telecommunications and other sectors. With the resources available in the Virtex 7, we were able to implement half of a ϕ sector corresponding to the positive η of the detector. Most of the firmware development was focused on two subprojects, one with only the barrel layers and another one that included the disks. The two projects are shown in Figure A.13.

The first set of results correspond to the hardware performance compared to our C++ emulation. As shown earlier, the performance of the integer emulation of the tracklet algorithm was well within the requirements of the trigger. The firmware was then developed to match the emulation on a bitwise level for all calculations of the algorithm. The Virtex 7 allows for larger multiplications than the native 18x25 bits by combining multiple DSPs in a chain at the cost of a more difficult routing. Given the tight constraints for the algorithm, we had to minimize these large operations without sacrificing performance. A balance

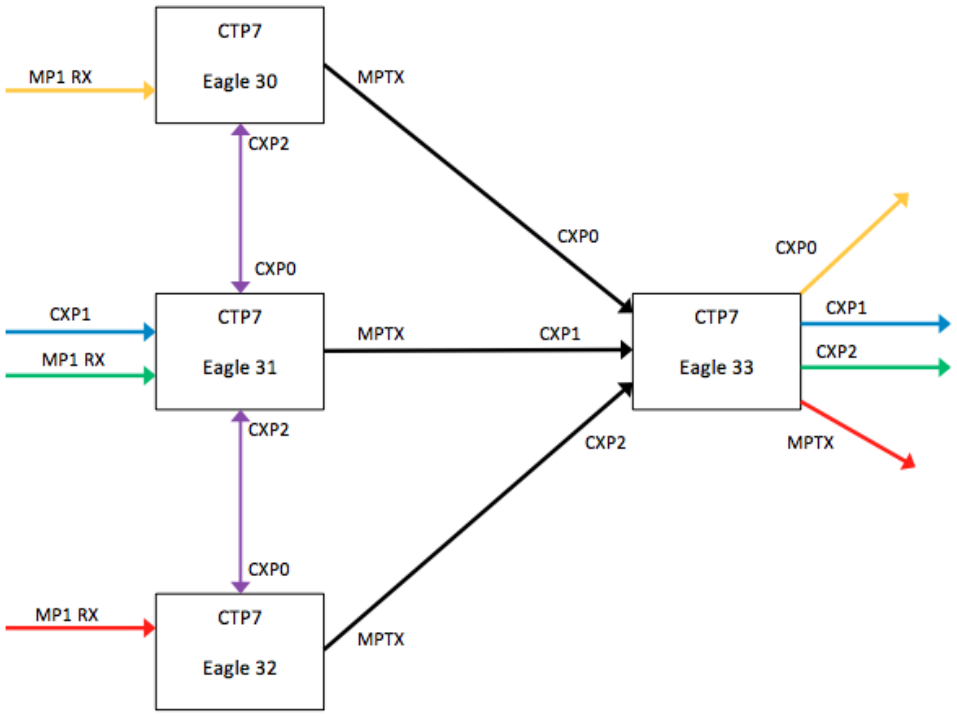

Figure A.12: Diagram of the demonstrator communications. Each of the boards are named *eagleXX* as a way to identify them for RPC communication. Eagle33 was used as the input/sink board. Eagle31 was used as the central processing board. Eagle30 and eagle32 were used as neighbor processing boards.

was achieved between efficient resource usage and precision in the calculations.

The most challenging events for tracking are those with jets in a high pileup environment. We studied events with a single muon track and no additional interactions as well as $t\bar{t}$ events with pileup of 200 interactions. Within the Vivado suite, we were able to fully simulate our firmware before implementing it on the boards. This simulation is very robust and helped significantly with the firmware development to the point that we could confidently assume that results seen in the simulation would correspond to what was seen in the hardware. A comparison of the final track parameters in $t\bar{t}$ events between the emu-

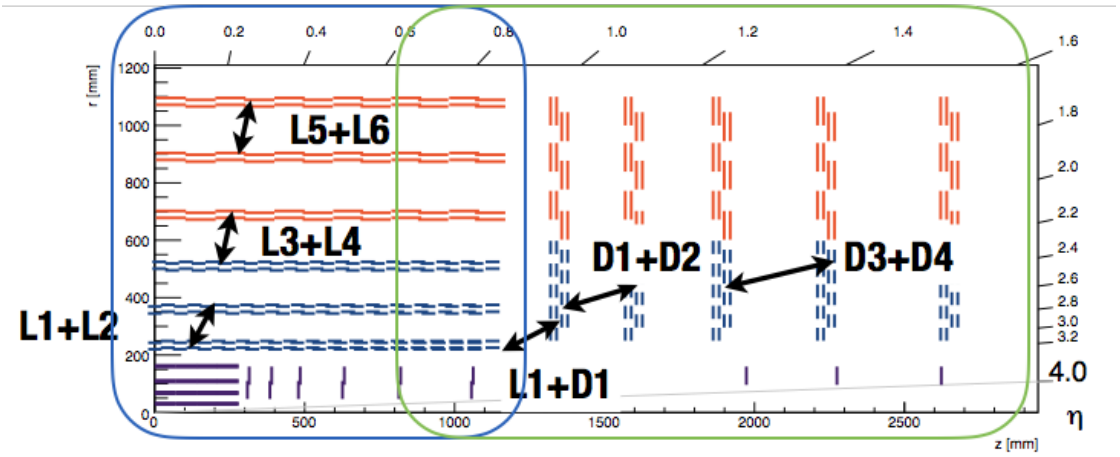

Figure A.13: Diagram of the two subprojects used for development. The arrows in the diagram show the layer pairs used for seeding.

lation and firmware simulation is shown in Figure A.14. We can see an almost perfect agreement between the two implementations with over 99% agreement between the hardware output and the emulation.

Even though the firmware simulation was used for most of the calculation comparisons with the C++ emulation, the actual hardware implementation had to be optimized to fit timing and routing constraints in the FPGA. The project was set to run at clock speed of 240 MHz. Since each step in our algorithm was designed with a fixed latency, the faster the clock speed the more operations can be performed. We chose 240 MHz as our clock speed as a compromise between high frequency and what could be easily routed on the Virtex 7. This also happens to be an integer multiple of the LHC's collision frequency of 40 MHz.

The strategy used to achieve successful routing and placement of the project on the FPGA consisted of flip-flop latching, minimal DSP chaining, and optimal

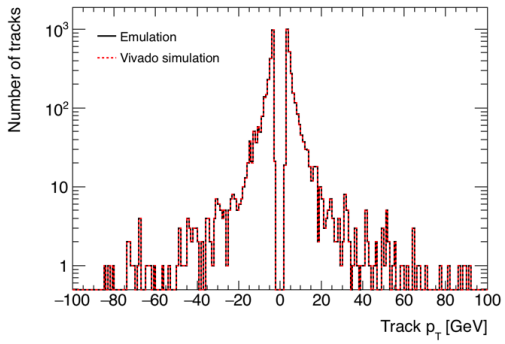

(a) Transverse momentum of tracks in barrel subproject.

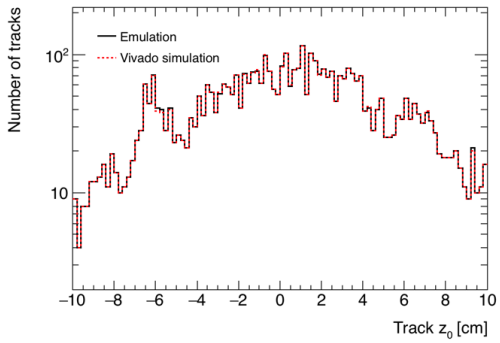

(b) Position in the z axis of tracks in barrel subproject.

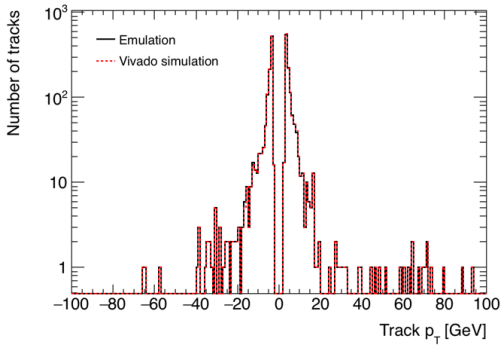

(c) Transverse momentum of tracks in disk subproject.

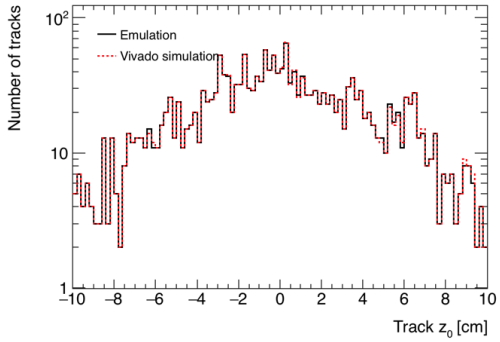

(d) Position in the z axis of tracks in disk subproject.

Figure A.14: Track parameter comparison for $t\bar{t}$ events with pileup of 200. The level of agreement between the firmware implementation and C++ emulation is higher than 99%.

pipelining of RAM inputs and outputs. Each additional register latch increased the overhead latency in each processing step, but this was taken into account for the overall latency. Flip-flops are an abundant resource in the FPGA and thus were used extensively to ease routing and placement. Block RAM resources are more scarce and are harder to route, so they were used only when absolutely necessary. A report of resource usage from the Vivado development suite is shown in Figure A.15. The report shows that the project that was implemented fits in the current generation Virtex 7 FPGA, with BRAMs being the most used resource as expected. The Gigabit Transceiver (GT) usage is exclusively driven

by the optical connections that the CTP7 board had implemented and does not vary with the size of the project.

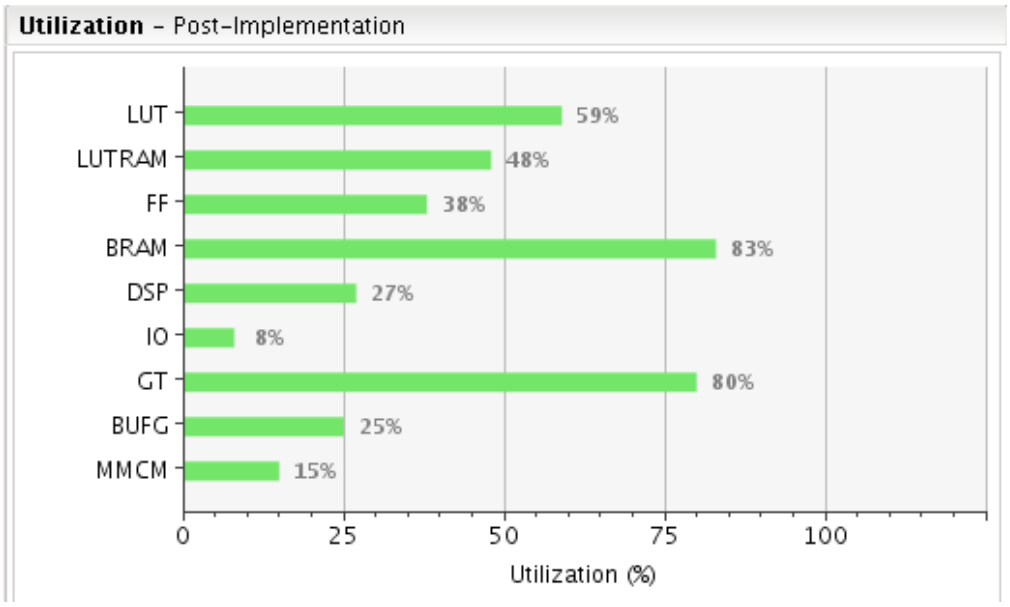

Figure A.15: Resource usage report of tracklet hardware implementation. A reduced number of seeding layers was used to simplify the routing. The project fits in the current generation of FPGAs with room for improvement and optimization. Gigabit Transceiver (GT) usage corresponds to the optical transceivers implemented in the CTP7 board and does not depend on the size of the project.

The next set of results presented are the timing measurements of the firmware implementation. Each step in the algorithm is fixed at 150 ns of available processing time. This time starts only after the first input has gone through the step and the first output is produced. After that, a new output is produced on every clock cycle until the time limit is reached. The time it takes for each module to produce an output after the input is received is considered the module's intrinsic latency. Using the firmware simulation, this latency can be estimated for every step and a total latency can be calculated. A model for the latency budget is presented in Table A.1, where we include the fixed latency,

Step	Processing (ns)	Latency (ns)	Link lat. (ns)	Total (ns)
Input Link	0.0	4.2	316.7	320.9
Layer Router	150.0	4.2	-	154.2
VM Router	150.0	16.7	-	166.7
Tracklet Engine	150.0	20.8	-	170.8
Tracklet Calculator	150.0	179.2	-	329.2
Projection Transceiver	150.0	54.2	316.7	520.8
Projection Router	150.0	20.8	-	170.8
Match Engine	150.0	25.0	-	175.0
Match Calculator	150.0	66.7	-	216.7
Match Transceiver	150.0	50.0	316.7	516.7
Track Fit	150.0	108.3	-	258.3
Duplicate Removal	0.0	25.0	-	25.0
Track Link	0.0	4.2	316.7	320.9
Total	1500	579.2	1266.7	3345.8

Table A.1: Latency model estimated from simulation. Input and Track Link are not steps in the processing, but add to the latency due to communication delay.

the intrinsic latency, and the communication latency for each model where it applies. The total estimate for the latency can be then compared to actual measurements in the hardware.

As mentioned before, a single CTP7 board serves as the stub input source as well as the track sink. This allows for an end-to-end synchronized latency measurement using a common clock. We developed the firmware that sends the stubs to the processing boards and receives the incoming tracks, so it was a simple task to add a clock counter that would start as soon as the first stub was sent and stopped when the first track was received. This is how we measured the algorithm latency to be 800 clock cycles using a 240 MHz clock (3.33 μs). The latency model estimate is only 3 clock cycles different than the measured value, thus giving us confidence that we understand the latency of the algorithm. The measured latency is well within the 4 μs required by the trigger.

As a final test of the system, and a necessary requirement for any system to be incorporated into CMS, we ran our algorithm for extended periods of time to check for stability and random bit errors. Before we could run this test, we had to emulate the structure of the LHC bunch trains in our input algorithm. Unfortunately, the number of bunches in an LHC orbit does not divide evenly with our replication factor of 6, which causes a small inefficiency at the tail ends of the orbit. Once the input was well emulated, we were able to run the tracklet algorithm on the boards for many days without a single bit error.

A.6 Conclusion

In this Appendix we have described a prototype system to perform tracking at 40 MHz for the upgraded CMS detector. With the high luminosity upgrade of the LHC, CMS hopes to collect 3000 fb^{-1} of integrated luminosity by the end of its run. The HL-LHC will provide an estimated instantaneous luminosity of $\mathcal{L} = 7.5 \times 10^{34}\ \text{cm}^{-2}\text{s}^{-1}$, achieved by an average of 200 interactions per bunch crossing. The current trigger system will not be able to handle the rate unless tracking information is incorporated at the hardware level.

A road-search tracking algorithm, called the *tracklet* algorithm, was developed for an FPGA-only hardware implementation. This algorithm was shown to meet the requirements specified by the trigger. The resolution on the track parameters using integer precision calculations was seen to be within the specifications. In order to keep the trigger rate at a reasonable level, reconstructed tracks were required to be at least 2 GeV of momentum and the position in the z-axis to be at most 15 cm from the interaction point. A precise measurement

of the track's transverse momentum was also needed if these tracks were to be used in event-wide calculations, such as $\not{E}_T$. The tracklet algorithm also met these track quality requirements.

A demonstrator system was built to prove the core concepts of the algorithm using current FPGA technology. Some simplifications were made and a reduced version of the full system was implemented on a Virtex 7 FPGA. The results of the calculations in the hardware matched the expected results from a C++ emulation to better than 99% agreement. Since the algorithm was designed to be fixed latency, we were able to estimate and then measure the total latency directly on the boards. Our latency model was within 3 clock cycles of the expected value and within the 4 μs requirement. Finally, we tested the stability of the system by running it continuously for several days without a single bit error.

APPENDIX B

MUON MOMENTUM RESOLUTION MEASUREMENTS USING COSMIC RAYS

In this Section, we describe the results from muon momentum resolution measurements using the cosmic ray events collected during the 2016 running of CMS. The method for resolution measurement was initially developed in 2009 for the first run of CMS and it is described in the literature [52, 87]. We present a brief description of the relevant parts of the method followed by the final results. The goal of this measurement is to provide analyses in CMS that use muons with a resolution measurement that can be used when studying the collision data.

For this measurement, we only care about those cosmic muons that resemble a collision event. Most of the muons produced from cosmic rays that pass through the CMS detector are too far from the interaction point and thus are ignored. A special reconstruction (*2-leg* reconstruction) is applied to muons that pass near the center of the detector. The single track from a cosmic muon is split into an upper and a lower leg to better emulate a collision event. The direction of the momentum of the upper leg must be inverted in the reconstruction, but otherwise the event is very similar to a high p_T collision event. A schematic of the track splitting is shown in Figure B.1.

To select further a clean list of tracks, we apply additional event cuts as well as quality cuts on the tracks themselves. The event cuts are:

- There are exactly two tracks in the event.
- There are exactly two muons reconstructed as global muons.
- All the muon reconstruction algorithm refits described in Section 4.2 must

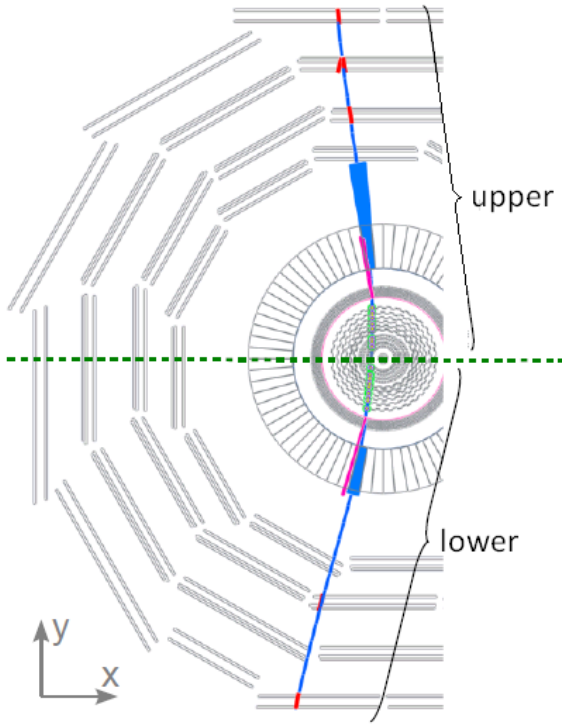

Figure B.1: Super-pointing cosmic muon 2-leg reconstruction.

succeed for each pair of tracks.

The quality cuts are:

- A cut on the difference in θ and ϕ positions of the tracks is applied to ensure they both come from the same cosmic ray muon.
- Each track must have at least one hit in the pixel detector.
- Each track must have at least five hits on the strip tracker.
- Veto hits in the CSC modules.

There are no explicit cuts on the impact parameter, but the pixel requirement serves a similar purpose. The purpose of the CSC veto is to only consider tracks

in the barrel. The alignment of the disk detectors must be studied independently, but given the lack of cosmic tracks that pass through the disks and the interaction point, we decided to only focus on tracks in the barrel.

The two reconstructed legs come from the same muon and thus their true momenta are the same. The measured quantities are not exactly equal due to detector effects and the differences give a measure of the resolution. We study the relative difference for the inverse momentum q/p_T,

$$R(q/p_T) = \frac{(q/p_T)^{upper} - (q/p_T)^{lower}}{\sqrt{2}(q/p_T)^{lower}}. \tag{B.1}$$

We normalize the difference using the momentum of the lower leg because this leg of the cosmic is reconstructed in the same direction as normal collision muon, but either leg or the average of the two give similar results for the bulk of the distribution. The factor of $\sqrt{2}$ comes from the assumption that these are two uncorrelated momentum measurements. There can be correlations that are not accounted for and we use Monte Carlo truth information to determine if this factor is valid. A comparison between the difference method and the measurement using MC truth is shown in Figure B.2.

The second quantity that is useful to study is the pull distribution of the upper and lower measurements, which serves as a diagnostic for the uncertainties on the momentum measurements. We define the pull as

$$P(q/p_T) = \frac{(q/p_T)^{upper} - (q/p_T)^{lower}}{\sqrt{\sigma^2_{(q/p_T)^{upper}} + \sigma^2_{(q/p_T)^{lower}}}}. \tag{B.2}$$

For perfectly unbiased measurements, the pull distribution would be centered at zero and, if the assigned uncertainties properly describe the detector conditions, the width of the distribution would be unity.

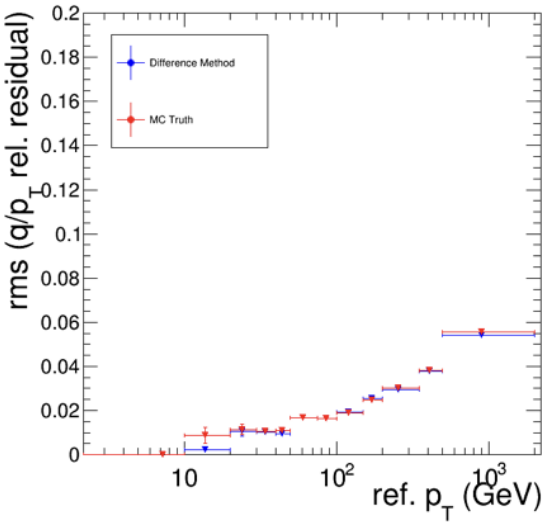

Figure B.2: Difference method validation compared to MC truth information using TuneP.

Cosmic muons are collected in CMS when collisions are not happening. During 2016, a small sample of cosmics was collected before the official collision runs began. A larger sample of cosmics was collected during the interfill periods of collision data taking. The tracker alignment conditions for the interfill sample resemble more closely those of collision events and therefore, this sample was used for the results presented below.

The results are presented in bins of the lower leg p_T assigned using the tracker-only algorithm. In each of these bins, we calculate the resolution and the pull. The distributions are then fitted using a Gaussian to capture the behavior of the core, and the tails are studied using the RMS as a statistic. Example distributions for a specific p_T bin are shown in Figure B.3.

The pull distributions are shown in Figure B.4 and as hoped, the mean is consistent with zero and the width is close to 1. These results were used as a confirmation that the assigned uncertainties were appropriate for the detector

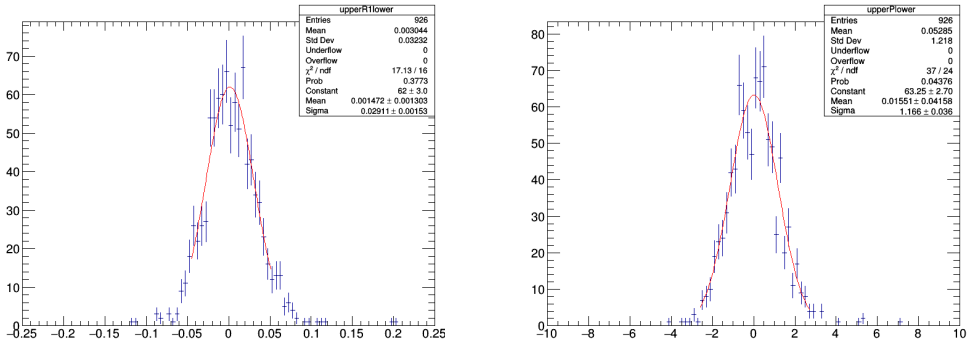

Figure B.3: Example distributions of $R(q/p_T)$ and $P(q/p_T)$ for TuneP muons with p_T between 200 and 350 GeV.(Left) Resolution distribution. (Right) Pull distribution.

alignment in 2016. The next set of results correspond to resolution measured with the interfill cosmics collected in 2016. In Figure B.5, we present the RMS of the $R(q/p_T)$ distribution and we also show the width of a Gaussian fitted to the core of the distributions. The measured resolution is approximately 8% in the highest p_T bin and as low as 1% for low momentum muons. These results are consistent with previous measurements of muon momentum resolution [52].

Finally, the results obtained in the data can be compared with the Monte Carlo simulation of cosmic events. The simulation uses the asymptotic alignment of the detector. This alignment is the best estimate of the position of each detector module that one could achieve in the asymptotic limit of infinite data. A comparison between the data and the simulation is shown in Figure B.6.

The simulation describes well the data for muons with momentum below 200 GeV and we see some slightly worse resolution in the data above this energy. Even for muons in the highest bin, $p_T > 500$ GeV, where the resolution is approximately 8%, this measurement demonstrates the great performance of the muon system in CMS. We propagate this result as a systematic uncertainty

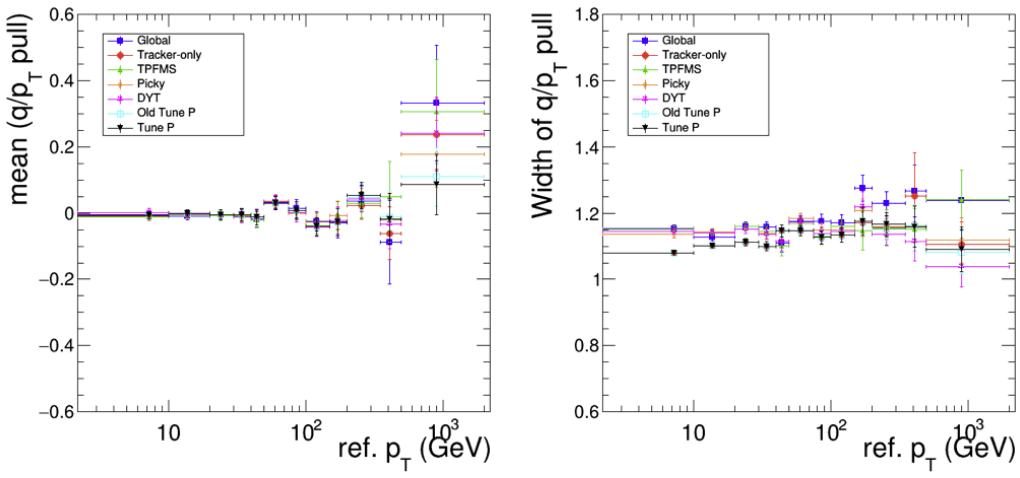

(a) Mean of pull distribution.

(b) Width of pull distribuiton.

Figure B.4: Pull distribution as a function of the lower track p_T. All the reconstruction algorithms are shown, but most analyses using high p_T muons use the TuneP assignment.

for the W_R search, although the mass resolution in our signal is driven by the jet energy resolution.

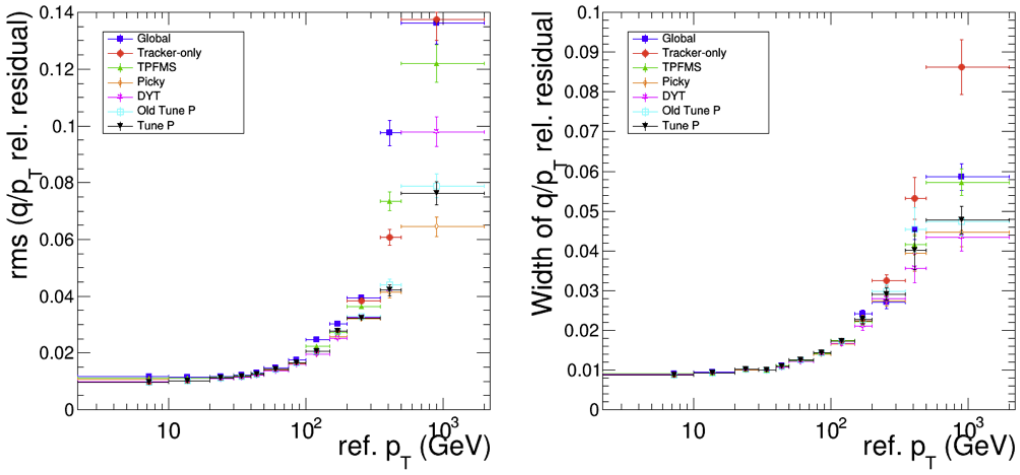

(a) RMS of resolution.

(b) Width of resolution.

Figure B.5: Resolution distribution as a function of the lower track p_T. All the reconstruction algorithms are shown, but most analyses use the TuneP assignment.

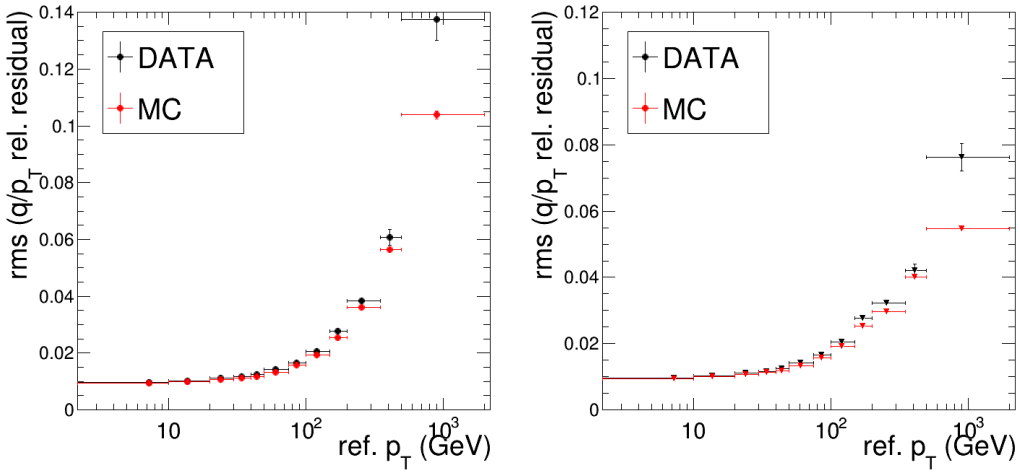

(a) Tracker Only assignment.

(b) TuneP assignment.

Figure B.6: Data/MC comparison of the resolution RMS with the asymptotic alignment conditions in the simulation.

BIBLIOGRAPHY

[1] S. Weinberg, "A Model of Leptons", *Phys. Rev. Lett.* **19** (1967) 1264–1266, doi: 10.1103/PhysRevLett.19.1264.

[2] F. Englert and R. Brout, "Broken Symmetry and the Mass of Gauge Vector Mesons", *Phys. Rev. Lett.* **13** (1964) 321–323, doi: 10.1103/PhysRevLett.13.321.

[3] P. W. Higgs, "Broken Symmetries and the Masses of Gauge Bosons", *Phys. Rev. Lett.* **13** (1964) 508–509, doi: 10.1103/PhysRevLett.13.508.

[4] ATLAS Collaboration, "Observation of a new particle in the search for the Standard Model Higgs boson with the ATLAS detector at the LHC", *Phys. Lett.* **B716** (2012) 1–29, doi: 10.1016/j.physletb.2012.08.020, arXiv:1207.7214.

[5] CMS Collaboration, "A New Boson with a Mass of 125 GeV Observed with the CMS Experiment at the Large Hadron Collider", *Science* **338** (2012) 1569–1575, doi: 10.1126/science.1230816.

[6] W.-Y. Keung and G. Senjanović, "Majorana neutrinos and the production of the right-handed charged gauge boson", *Phys. Rev. Lett.* **50** (May, 1983) 1427–1430, doi: 10.1103/PhysRevLett.50.1427.

[7] A. Maiezza, M. Nemevsek, F. Nesti, and G. Senjanovic, "Left-Right Symmetry at LHC", *Phys. Rev. D* **82** (2010) 055022, doi: 10.1103/PhysRevD.82.055022, arXiv:1005.5160.

[8] R. N. Mohapatra and J. C. Pati, ""natural" left-right symmetry", *Phys. Rev. D* **11** (May, 1975) 2558–2561, doi: 10.1103/PhysRevD.11.2558.

[9] J. C. Pati and A. Salam, "Lepton number as the fourth "color"", *Phys. Rev. D* **10** (Jul, 1974) 275–289, doi: 10.1103/PhysRevD.10.275.

[10] G. Senjanovic and R. N. Mohapatra, "Exact left-right symmetry and spontaneous violation of parity", *Phys. Rev. D* **12** (Sep, 1975) 1502–1505, doi: 10.1103/PhysRevD.12.1502.

[11] CMS Collaboration, "Search for heavy neutrinos and W bosons with right-handed couplings in proton-proton collisions at $\sqrt{s} = 8$ TeV", *Eur. Phys. J.* **C74** (2014), no. 11, 3149, doi: 10.1140/epjc/s10052-014-3149-z, arXiv:1407.3683.

[12] S. L. Glashow, "Partial Symmetries of Weak Interactions", *Nucl. Phys.* **22** (1961) 579–588, doi: 10.1016/0029-5582(61)90469-2.

[13] P. Langacker, "The standard model and beyond". 2010. ISBN 9781420079067,

[14] E. C. G. Sudarshan, "Ten years of the universal V-A weak interaction theory and some remarks on a universal theory of primary interactions",.

[15] Mu3e Collaboration, "The Mu3e Experiment at PSI", *Nucl. Part. Phys. Proc.* **260** (2015) 155–159, doi: 10.1016/j.nuclphysbps.2015.02.033.

[16] L. A. Winslow, "Discovering the Majorana neutrino: The next generation of experiments", *AIP Conf. Proc.* **1666** (2015) 170005, doi: 10.1063/1.4915595.

[17] Particle Data Group Collaboration, "Review of Particle Physics", *Chin. Phys.* **C40** (2016), no. 10, 100001, doi: 10.1088/1674-1137/40/10/100001.

[18] SNO Collaboration, "Direct evidence for neutrino flavor transformation from neutral current interactions in the Sudbury Neutrino Observatory", *Phys. Rev. Lett.* **89** (2002) 011301, doi: 10.1103/PhysRevLett.89.011301, arXiv:nucl-ex/0204008.

[19] Super-Kamiokande Collaboration, "Evidence for oscillation of atmospheric neutrinos", *Phys. Rev. Lett.* **81** (1998) 1562–1567, doi: 10.1103/PhysRevLett.81.1562, arXiv:hep-ex/9807003.

[20] WMAP Collaboration, "First year Wilkinson Microwave Anisotropy Probe (WMAP) observations: Determination of cosmological parameters", *Astrophys. J. Suppl.* **148** (2003) 175–194, doi: 10.1086/377226, arXiv:astro-ph/0302209.

[21] S. P. Martin, "A Supersymmetry primer", ch. 1, p. 1. WORLD SCIENTIFIC, 2011. arXiv:hep-ph/9709356. doi: 10.1142/9789812839657˙0001.

[22] M. Persic and P. Salucci, "Dark and visible matter in spiral galaxies", *Mon. Not. Roy. Astron. Soc.* **234** (1988) 131–154.

[23] LUX Collaboration, "First results from the LUX dark matter experiment at the Sanford Underground Research Facility", *Phys. Rev. Lett.* **112** (2014) 091303, doi: 10.1103/PhysRevLett.112.091303, arXiv:1310.8214.

[24] X. Wu, "The Silicon-Tungsten Tracker of the DAMPE Mission", *PoS* **ICRC2015** (2016) 1192.

[25] M. Gell-Mann, P. Ramond, and R. Slansky, "Complex Spinors and Unified Theories", *Conf. Proc.* **C790927** (1979) 315–321, arXiv:1306.4669.

[26] R. N. Mohapatra and G. Senjanovic, "Neutrino Mass and Spontaneous Parity Violation", *Phys. Rev. Lett.* **44** (1980) 912, doi: 10.1103/PhysRevLett.44.912.

[27] J. Berger, J. A. Dror, and W. H. Ng, "Sneutrino Higgs models explain lepton non-universality in $eejj, ejj$ excesses", *JHEP* **09** (2015) 156, doi: 10.1007/JHEP09(2015)156, arXiv:1506.08213.

[28] P. S. Bhupal Dev, C.-H. Lee, and R. N. Mohapatra, "Leptogenesis Constraints on the Mass of Right-handed Gauge Bosons", *Phys. Rev. D* **90** (2014), no. 9, 095012, doi: 10.1103/PhysRevD.90.095012, arXiv:1408.2820.

[29] J. H. Collins and W. H. Ng, "A 2TeV W_R , supersymmetry, and the Higgs mass", *JHEP* **01** (2016) 159, doi: 10.1007/JHEP01(2016)159, arXiv:1510.08083.

[30] A. Das, N. Nagata, and N. Okada, "Testing the 2-TeV Resonance with Trileptons", *JHEP* **03** (2016) 049, doi: 10.1007/JHEP03(2016)049, arXiv:1601.05079.

[31] B. A. Dobrescu and P. J. Fox, "Signals of a 2 TeV W' boson and a heavier Z' boson", *JHEP* **05** (2016) 047, doi: 10.1007/JHEP05(2016)047, arXiv:1511.02148.

[32] L. Evans and P. Bryant, "LHC Machine", *JINST* **3** (2008) S08001, doi: 10.1088/1748-0221/3/08/S08001.

[33] C. Lefvre, "The CERN accelerator complex. Complexe des accélérateurs du CERN", (Dec, 2008).

[34] S. Dailler, "Cross section of LHC dipole. Dipole LHC: coupe transversale.", (Apr, 1999).

[35] H. Wiedemann, "Particle Accelerator Physics". Graduate Texts in Physics. Springer, Berlin, Germany, 2015. doi: 10.1007/978-3-319-18317-6, ISBN 9783319183169, 9783319183176,

[36] ALICE Collaboration, "The ALICE experiment at the CERN LHC", *JINST* **3** (2008) S08002, doi: 10.1088/1748-0221/3/08/S08002.

[37] ATLAS Collaboration, "The ATLAS Experiment at the CERN Large Hadron Collider", *JINST* **3** (2008) S08003, doi: 10.1088/1748-0221/3/08/S08003.

[38] CMS Collaboration, "The CMS Experiment at the CERN LHC", *JINST* **3** (2008) S08004, doi: 10.1088/1748-0221/3/08/S08004.

[39] LHCb Collaboration, "The LHCb Detector at the LHC", *JINST* **3** (2008) S08005, doi: 10.1088/1748-0221/3/08/S08005.

[40] LHCb Collaboration, "First Evidence for the Decay $B_s^0 \to \mu^+\mu^-$", *Phys. Rev. Lett.* **110** (2013), no. 2, 021801, doi: 10.1103/PhysRevLett.110.021801, arXiv:1211.2674.

[41] LHCb Collaboration, "Observation of $J/\psi p$ Resonances Consistent with Pentaquark States in $\Lambda_b^0 \to J/\psi K^- p$ Decays", *Phys. Rev. Lett.* **115** (2015) 072001, doi: 10.1103/PhysRevLett.115.072001, arXiv:1507.03414.

[42] CMS Public, "CMS Luminosity - Public Results". https://twiki.cern.ch/twiki/bin/view/CMSPublic/LumiPublicResults, last accessed on 2017-04-26.

[43] CMS Collaboration, "Precise Mapping of the Magnetic Field in the CMS Barrel Yoke using Cosmic Rays", *JINST* **5** (2010) T03021, doi: 10.1088/1748-0221/5/03/T03021, arXiv:0910.5530.

[44] CMS CollaborationV. Karimäki, et al., "The CMS tracker system project: Technical Design Report". Technical Design Report CMS. CERN, Geneva, 1997.

[45] CMS Collaboration, "Description and performance of track and primary-vertex reconstruction with the CMS tracker", *J. Instrum.* **9** (May, 2014) P10009.

[46] CMS Collaboration, S. Taroni, "The Alignment of the CMS Silicon Tracker", in *Proceedings, 13th ICATPP Conference on Astroparticle, Particle, Space Physics and Detectors for Physics Applications (ICATPP 2011): Como, Italy, October 3-7, 2011*, pp. 676–680. 2012. doi: 10.1142/9789814405072˙0100.

[47] CMS Collaboration, G. L. Bayatian et al., "CMS Physics: Technical Design Report Volume 1: Detector Performance and Software". Technical Design Report CMS. CERN, Geneva, 2006.

[48] CMS Collaboration, CMS Collaboration, "The CMS electromagnetic calorimeter project: Technical Design Report". Technical Design Report CMS. CERN, Geneva, 1997.

[49] CMS Collaboration, CMS Collaboration, "The CMS hadron calorimeter project: Technical Design Report". Technical Design Report CMS. CERN, Geneva, 1997.

[50] CMS Collaboration, CMS Collaboration, "The CMS muon project: Technical Design Report". Technical Design Report CMS. CERN, Geneva, 1997.

[51] CMS Collaboration, "The performance of the CMS muon detector in proton-proton collisions at sqrt(s) = 7 TeV at the LHC", *JINST* **8** (2013) P11002, doi: 10.1088/1748-0221/8/11/P11002, arXiv:1306.6905.

[52] CMS Collaboration, "Performance of CMS muon reconstruction in pp collision events at $\sqrt{s}$ = 7 TeV", *JINST* **7** (2012) P10002, doi: 10.1088/1748-0221/7/10/P10002, arXiv:1206.4071.

[53] CMS Collaboration, "The CMS trigger system", *JINST* **12** (2016) P01020.

[54] S. Bentvelsen and I. Meyer, "The Cambridge jet algorithm: Features and applications", *Eur. Phys. J.* **C4** (1998) 623–629, doi: 10.1007/s100520050232, arXiv:hep-ph/9803322.

[55] M. Cacciari, G. P. Salam, and G. Soyez, "The anti-k_t jet clustering algorithm", *JHEP* **04** (2008) 063, doi: 10.1088/1126-6708/2008/04/063, arXiv:0802.1189.

[56] F. Zimmermann, "CERN upgrade plans for the LHC and its injectors", *PoS* **EPS-HEP 2009** (2009) 140.

[57] T. Sjstrandet al., "An Introduction to PYTHIA 8.2", *Comput. Phys. Commun.* **191** (Oct, 2014) 159–177. 45 p.

[58] J. Alwall et al., "MadGraph 5 : Going Beyond", *JHEP* **06** (2011) 128, doi: 10.1007/JHEP06(2011)128, arXiv:1106.0522.

[59] S. Frixione, P. Nason, and C. Oleari, "Matching NLO QCD computations with Parton Shower simulations: the POWHEG method", *JHEP* **11** (2007) 070, doi: 10.1088/1126-6708/2007/11/070, arXiv:0709.2092.

[60] A. Rybin et al., "Geant 4 - a simulation toolkit", *Nucl. Instr. Meth. A* **506** (2003), no. 3, 250, doi: 10.1016/S0168-9002(03)01368-8.

[61] P. Billoir, "Progressive track recognition with a Kalman like fitting procedure", *Comput. Phys. Commun.* **57** (1989) 390–394, doi: 10.1016/0010-4655(89)90249-X.

[62] P. Billoir and S. Qian, "Simultaneous pattern recognition and track fitting by the Kalman filtering method", *Nucl. Instrum. Meth.* **A294** (1990) 219–228, doi: 10.1016/0168-9002(90)91835-Y.

[63] A. Strandlie and W. Wittek, "Propagation of Covariance Matrices of Track Parameters in Homogeneous Magnetic Fields in CMS", Technical Report CMS-NOTE-2006-001, CERN, Geneva, Jan, 2006.

[64] J. Myrheim and L. Bugge, "A FAST RUNGE-KUTTA METHOD FOR FITTING TRACKS IN A MAGNETIC FIELD", *Nucl. Instrum. Meth.* **160** (1979) 43–48, doi: 10.1016/0029-554X(79)90163-0.

[65] CMS Collaboration, "Performance of electron reconstruction and selection with the CMS detector in proton-proton collisions at $\sqrt{s} = 8$ TeV", *J. Instrum.* **10** (Feb, 2015) P06005. 63 p.

[66] A. Hocker et al., "TMVA - Toolkit for Multivariate Data Analysis", *PoS* **ACAT** (2007) 040, arXiv:physics/0703039.

[67] W. Adam, R. Fruhwirth, A. Strandlie, and T. Todorov, "Reconstruction of electrons with the Gaussian sum filter in the CMS tracker at LHC", *eConf*

C0303241 (2003) TULT009, doi: 10.1088/0954-3899/31/9/N01, arXiv:physics/0306087.

[68] CMS Collaboration, "Particle-Flow Event Reconstruction in CMS and Performance for Jets, Taus, and MET", Technical Report CMS-PAS-PFT-09-001, CERN, Geneva, Apr, 2009.

[69] CMS Collaboration, "Jet performance in pp collisions at $\sqrt{s}$=7 TeV", CMS Physics Analysis Summary CMS-PAS-JME-10-003, 2010.

[70] R. Gavin, Y. Li, F. Petriello, and S. Quackenbush, "FEWZ 2.0: A code for hadronic Z production at next-to-next-to-leading order", *Comput. Phys. Commun.* **182** (2011) 2388–2403, doi: 10.1016/j.cpc.2011.06.008, arXiv:1011.3540.

[71] CMS Collaboration Collaboration, "Search for heavy neutrinos and W bosons with right handed couplings in proton-proton collisions at $\sqrt{s}$ = 13 TeV", Technical Report CMS-PAS-EXO-16-045, CERN, Geneva, 2017.

[72] CMS Collaboration Collaboration, "Search for new physics in final states with an energetic jet or a hadronically decaying W or Z boson using 35.9 fb^{-1} of data at $\sqrt{s}$ = 13 TeV", Technical Report CMS-PAS-EXO-16-048, CERN, Geneva, 2017.

[73] J. M. Lindert et al., "Precise predictions for V+jets dark matter backgrounds", arXiv:1705.04664.

[74] J. Butterworth et al., "PDF4LHC recommendations for LHC Run II", *J. Phys.* **G43** (2016) 023001, doi: 10.1088/0954-3899/43/2/023001, arXiv:1510.03865.

[75] CMS Collaboration, "CMS luminosity measurements for the 2016 data taking period", Technical Report CMS-PAS-LUM-17-001, CERN, Geneva, 2017.

[76] CMS Collaboration, "Jet energy scale and resolution in the CMS experiment in pp collisions at 8 TeV", *JINST* **12** (2017), no. 02, P02014, doi: 10.1088/1748-0221/12/02/P02014, arXiv:1607.03663.

[77] CMS Collaboration, "Performance of electron reconstruction and selection with the CMS detector in proton-proton collisions at $\sqrt{s}$ = 8 TeV", *JINST* **10** (2015) P06005, doi: 10.1088/1748-0221/10/06/P06005, arXiv:1502.02701.

[78] CMS Collaboration, "Performance of Photon Reconstruction and Identification with the CMS Detector in Proton-Proton Collisions at sqrt(s) = 8 TeV", *JINST* **10** (2015), no. 08, P08010, doi: 10.1088/1748-0221/10/08/P08010, arXiv:1502.02702.

[79] The CMS Collaboration, "Technical proposal for the Phase-II upgrade of the CMS detector", Technical Report CERN-LHCC-2015-010, 2015.

[80] J. Chaves, "Implementation of FPGA-based level-1 tracking at CMS for the HL-LHC", *JINST* **9** (2014) C10038.

[81] CMS Collaboration, "L1 Tracklet-Based Track Finding and Fitting", (May, 2016).

[82] Xilinx Incorporated, "Accelerating Design Productivity with 7 Series FPGAs and DSP Platforms". https://www.xilinx.com/support/documentation/white_

papers/wp406-DSP-Design-Productivity.pdf, last accessed on 2017-04-29.

[83] Xilinx Incorporated, "7 Series FPGAs Overview". https://www.xilinx.com/products/silicon-devices/fpga/virtex-7.html, last accessed on 2017-03-28.

[84] A. Svetek et al., "The Calorimeter Trigger Processor Card", *JINST* **11** (2016) C02011.

[85] The CMS Collaboration, "CMS technical design report for the Level-1 trigger upgrade", Technical Report CERN-LHCC-2013-011, 2013.

[86] P. Franaszek and A. Widmer, "Byte oriented dc balanced (0,4) 8b/10b partitioned block transmission code", December 4, 1984.

[87] CMS Collaboration, "Performance of CMS Muon Reconstruction in Cosmic-Ray Events", *JINST* **5** (2010) T03022, doi: 10.1088/1748-0221/5/03/T03022, arXiv:0911.4994.